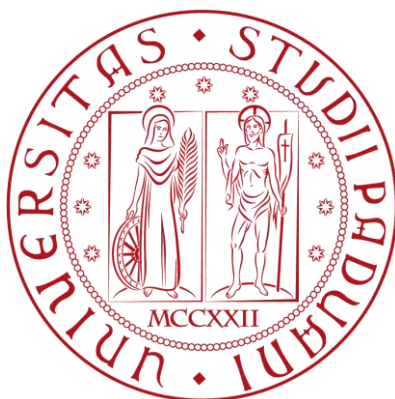# UNIVERSITÀ DEGLI STUDI DI PADOVA

Dipartimento di Ingegneria Industriale

Corso di Laurea Magistrale in Ingegneria dell' Energia Elettrica

NIO1 experiment, a source of negative hydrogen and deuterium ions accelerated up to 60kV: commissioning and analysis of first experimental results of ion beam extraction

Relatore:
prof. Piergiorgio Sonato

Laureando: Tommaso Patton

Correlatore:
Dott. Gianluigi Serianni
Dott. Matteo Brombin

ANNO ACCADEMICO 2015-2016

Abstract

In the framework of nuclear fusion for energy production, Neutral Beam Injectors (NBI) represent a key component in the plasma heating in order to achieve the proper temperature for fusion reactions. In particular an experimental reactor, so-called ITER, is under realization in Cadarache (France). In this project Padova will play a major role in the design, research, development and construction of the NBI prototype for ITER. With the aim to gain experience in neutral beam injectors, also a smaller experiment, called NIO1, has been installed at *Consorzio RFX* as a project developed by the host and INFN-LNL (Laboratori Nazionali di Legnaro). NIO1 is a negative ion source with an accelerating stage up to 60kV built as a very modular assembly on which a lot of diagnostics will be tested and installed; moreover numerical codes will be experimentally validated by NIO1 results. This thesis deals with the preparation and the commissioning of the NIO1 experiment: new diagnostics and components will be developed, installed and tested for the first time and also the first beam of particles will be extracted and accelerated. More In detail, in *Chapter1* main nuclear fusion processes, heating systems, ion sources and accelerator types for NBI are presented, furthermore a brief overview regarding the ITER project and the Padova Facility is given. In *Chapter2* the NIO1 experiment is presented in detail with special focus on the diagnostics already installed and planned; moreover also the electrical system is well described. In *Chapter3* the recovery operation after a previous breakage is described and some considerations regarding the new choices adopted are presented; then installation and test of a new passive protection system for the high voltage power supplies is described as well as an active protection system and two current sensors (Rogowski coils) that work with it; the tests directly on NIO1 are also presented; finally a measurement campaign regarding the electrostatic field coming from NIO1 and the improvement campaign of the magnetic filter are described. In *Chapter4* the design of an acquisition and conditioning board for thermocouples is presented; then a prototype of the board has been realized and the tests on NIO1 in order to analyze the main problems linked to thermal measurements in accelerators are presented. In *Chapter5* two current measurement systems developed, built and installed in order to analyze the beam current are described. In *Chapter6* first experimental results regarding the beam extraction are presented for 3 types of filling gasses: hydrogen, air and oxygen; finally events like electrical breakdowns and the first small beam currents are shown and analyzed.

Sommario

Nel contesto della fusione nucleare impiegata per la produzione di energia elettrica, gli iniettori di fasci di neutri rappresentano un ruolo fondamentale nel riscaldamento del plasma al fine di raggiungere la temperatura adeguata per le reazioni di fusione. In particolare un reattore sperimentale denominato ITER è in costruzione a Cadarache (Francia).In questo progetto, Padova giocherà un ruolo principale nella progettazione, nella ricerca e sviluppo e nella realizzazione del prototipo dell'iniettore di fasci di neutri per ITER. Con l'obiettivo di acquisire esperienza riguardo gli iniettori di fasci di neutri, anche un esperimento in scala ridotta chiamato NIO1 è stato installato presso il *Consorzio RFX* in quanto progetto sviluppato dal sito ospitante stesso e dall' istituto nazionale di fisica nucleare INFN-LNL (Laboratori Nazionali di Legnaro).NIO1 è una sorgente di ioni negativi con uno stadio di accelerazione fino a 60kV, costruito come un assemblato molto modulare sul quale molte diagnostiche verranno testate ed installate, inoltre codici numerici verranno validati per mezzo dei risultati sperimentali ottenuti per mezzo di NIO1. Questa tesi si occupa della preparazione e della messa in servizio dell'esperimento NIO1: nuove diagnostiche e componenti saranno sviluppati, installati e testati per la prima volta ed inoltre il primo fascio di particelle sarà estratto ed accelerato. Più in dettaglio, nel Capitolo 1 i principali processi di fusione nucleare, i sistemi di riscaldamento, le sorgenti di ioni ed i tipi di acceleratori negli iniettori di neutri sono presentati; inoltre verrà mostrata una breve panoramica del progetto ITER e dell'infrastruttura di Padova.Nel Capitolo 2 l'esperimento NIO1 è presentato in dettaglio con speciale attenzione riguardo le diagnostiche già installate e pianificate; inoltre sarà descritto l'impianto elettrico. Nel Capitolo 3 viene descritta l'operazione di recupero dall'incidente avvenuto precedentemente e verranno presentate alcune considerazioni riguardo le nuove scelte adottate; verranno poi descritti l'installazione ed il test di un nuovo sistema di protezioni passive per gli alimentatori di alta tensione ed anche un nuovo sistema di protezioni attive e 2 sensori di corrente (bobine di Rogowski) che lavorano con esso sono; verranno anche presentati i test direttamente su NIO1; infine sono descritte una campagna di misura del campo elettrostatico proveniente da NIO1 e una campagna di miglioramento del filtro magnetico. Nel Capitolo 4 è presentata la progettazione di una scheda di acquisizione e condizionamento del segnale di termocoppie, poi la realizzazione ed il test su NIO1 di un prototipo della scheda allo scopo di analizzare i problemi legati alle misure termiche negli acceleratori. Nel Capitolo 5 verranno descritti due sistemi di misura della corrente del fascio di particelle costruiti, sviluppati ed installati in NIO1.

Nel Capitolo 6 sono presentati i primi risultati sperimentali riguardanti l'estrazione di un fascio di particelle per 3 tipi di gas di processo: idrogeno, aria ed ossigeno; infine verranno descritti eventi quali le scariche elettriche nell'acceleratore e verranno analizzati i primi casi di correnti di fascio, per quanto piccole.

Indice

1 Introduction

In recent years energy and environmental problems are one of the most severe challenges for the future since the word population is growing rapidly, and at the same time especially for developing countries the final energy demand *per-capita* is increasing in order to improve their living conditions. Therefore these two facts drive a huge global increase of primary energy demand and hence new ways to satisfy this need are necessary. In particular fossil fuels are not limitless and problems due to the global warming caused by green-house gasses will be more considerable if the world population does not change the way to produce energy. Thus different scenarios have been developed from International Energy Agency (IEA) and other organizations in order to foresee the future for different ways to produce energy in which electrical energy production represent a key role.

Alternative energy sources for electrical energy production have to be investigated and analyzed; in particular controlled thermonuclear fusion can be a good candidate to meet these needs for several reasons like the abundance of fuel reserves, environmental impact and safety.

In this chapter the main physical principles of nuclear fusion reactions will be briefly presented as well as the way to exploit it to produce electrical energy; then an outline of the main issues with special focus on plasma heating will be given; in particular it will be explained in detail how one type of heating system, called Neutral Beam Injector (NBI) works; finally the Padova facility involved in NBI research and development within the international framework will be described.

1.1 Nuclear fusion

In contrast to nuclear fission, where heavy nuclei like uranium are fragmented and release energy, in fusion one starts with light elements and brings them together so that they may fuse to form heavier elements.

Energy comes out in the form of the kinetic energy of the products, from which it may be trapped and used for electricity production.

For both fission and fusion the principle to energy conversion is the same: products have less mass than reactants and this difference is the so called mass defect **m**; the energy produced **E** is proportional to the mass defect and it can be evaluated from the Einstein equation [Eq.1.1] where **c** is the speed of light:

$$E = mc^2 \qquad (1.1)$$

For the fusion process to occur, nuclei, that are positively charged, have to be brought close enough to overcome the electrostatic repulsion so that the so-called nuclear strong force sets in, which is effective for very close distances only. This is possible just when nuclei are heated to very high thermonuclear temperatures in the order of 10^7 -10^8 K (millions of °C).

Several possible fusion reactions are known, and studies of the nuclear properties of light element fusion indicate that three such reactions may be advantageous for the production of nuclear energy on the Earth:

- Deuterium-Deuterium
- Deuterium-Tritium
- Deuterium-Helium-3

For simplicity of notation the following symbol is used: *hydrogen nucleus→p, deuterium nucleus →D, tritium nucleus →T, helium nucleus→α, helium-3 He^3.*

Deuterium-Deuterium reaction

Deuterium (D) is not radioactive and is well available on the Earth; it can be easily extracted from the sea water in which it is present with a concentration of about 30mg/l, hence it is practically inexhaustible and is likely to last several tens of thousands of years.[1]

Therefore this would be the most suitable reactions, if it were not the most difficult of the three reactions to initiate since the reaction cross section is the smallest one. [Figure 1.1]

This reaction can evolve in two ways, each one with the same likelihood as reported below:

$$D + D \rightarrow He^3 + n + 3.27 MeV \qquad (1.2)$$

$$D + D \rightarrow T + p + 4.03 MeV \qquad (1.3)$$
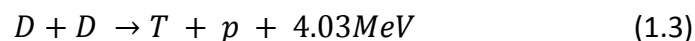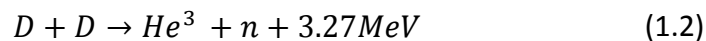
Since D has one proton and 2 neutrons in its nucleus (3 nucleons), these reactions produce an energy of 0.82 and 1.01 MeV per nucleon respectively that correspond to about a specific energy of 70 and 96 Tj/kg of deuterium.

Deuterium-Helium-3 reaction

This reaction [Eq.1.4] emits a lot of energy (3.66 MeV per nucleon) equivalent to 351 Tj/kg of the combined D–He^3 fuel. In the products there are no neutrons (if the D-D reaction that can also occur is minimized) therefore the activation of metals will be avoided limiting the presence of radioactive parts to the reaction chamber; furthermore the presence of electrically charged products could lead to the development of conversion systems that use directly the electrical energy instead of thermodynamic cycles.

$$D + He^3 \rightarrow He^4 + p + 18MeV \qquad\qquad (1.4)$$
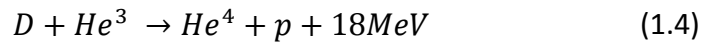
Unfortunately, Helium-3 is an isotope that is practically not present on the Earth since 99,999863% [2] is Helium-4;furthermore this reaction is also difficult to achieve although not as difficult as D-D. For these reasons research has not been focused on this process.

Deuterium-Tritium reaction

The D-T fusion is most conveniently achievable because the collision cross-section of the D-T fusion reactions is the highest and it occurs at the lowest temperature; therefore this is the most suitable reaction for fusion reactors.
Though Tritium is not present on the Earth, it can be created by the interaction of neutrons with lithium, which will be present in the reaction chamber.

$$Li^6 + n(slow) = \alpha + T + 4.8MeV \qquad\qquad (1.5)$$

$$Li^7 + n(fast) = \alpha + T + n - 2.5MeV \qquad\qquad (1.6)$$
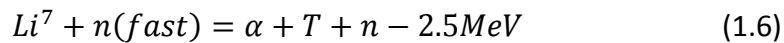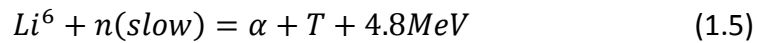
On the Earth natural lithium is present in both the previous isotopic forms in different fractions: 7.4% for Li^6 and 92.6% for Li^7 . Nevertheless, nuclear data show that the reaction involving Li^7 is much easier to initiate and as a result this reaction is the one dominating in the tritium creation.
Then, once tritium is created, the following fusion reaction can start.

$$D + T = \alpha + n + 17.6 \text{ MeV} \qquad\qquad (1.7)$$

Also this reaction generates a lot of energy per nucleon (3.52MeV) equal to 338 Tj/kg of Deuterium-Tritium mixture.
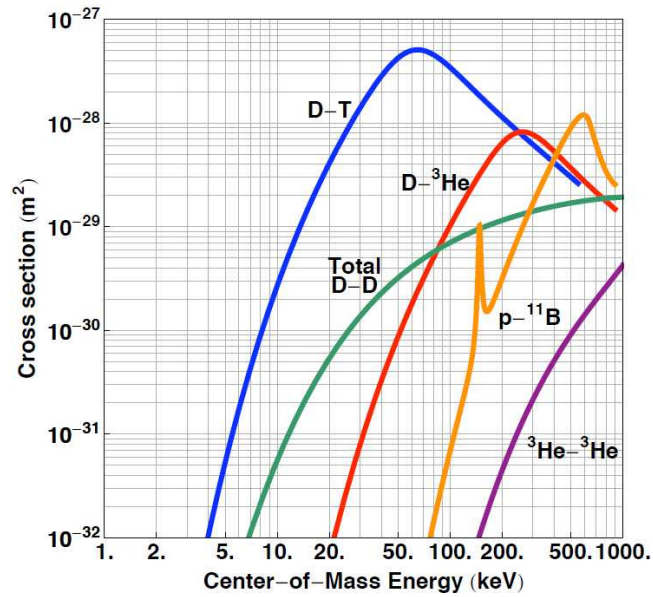
Figure 1.1 Fusion cross-sections of various fusion reactions as a function of kinetic energy of an incident D or p on a stationary target [3].

From Figure 1.1 we can see that D-T has a cross section much larger than the other reactions and the maximum is around 100 keV which correspond to a temperature of about 100 millions of °C we can also see that below the maximum peak its value is always almost 100 times bigger than the other ones and in order to produce enough energy a temperature of almost 10keV has to be achieved.

At these temperatures the energy is sufficient high to ionize the reactants, so they reach the so-called plasma state in which electrons are separated from positive nuclei, therefore we have a quasi-neutral fuel made of free charges that show a collective behavior.

1.2 Nuclear fusion for energy

The main goal to achieve a nuclear fusion reaction in reactors is to reach the balance between the energy input, represented by the energy deposited into the plasma by α particles (the neutrons produced escape from the plasma), produced by fusion reactions, and by additional heating systems, and energy losses, due to transport and radiation. The energy losses can be described by a parameter called energy confinement time τ_E:

$$\tau_E = \frac{W}{P_L} \qquad (1.8)$$

where W is the total energy stored in the fusion plasma and P_L is the total power loss due to the transport phenomena.

In order to obtain more energy from the fusion reaction than that supplied for plasma heating some requirements have to be met, corresponding to the threshold given by the Lawson criterion:

$$n\tau_E \geq \frac{12K_b T}{E_\alpha < \sigma v >} \qquad (1.9)$$

in which k_b is the Boltzmann constant, n is the plasma density, T is the plasma temperature, E_α is the energy of the alpha particles and <σv> is the reaction rate coefficient.

Since the terms at the right-hand side in Eq.1.9 depend only on the temperature T (also <σv> is a function of T), there is an absolute minimum for T, around 15keV, and the Lawson criterion corresponds to the numerical value shown in Eq.1.10

$$n\tau_E \geq 1.5 \cdot 10^{20} sm^{-3} \qquad (1.10)$$

Considering the fusion reaction for a range of particle temperatures, the variation of the fusion cross-section with temperature has to be taken into account. Roughly speaking, the fusion rate <σv> varies with temperature as T^2 and hence the Lawson criterion for a D-T plasma at T= 15 keV may be rewritten in the form also called triple product relation: [1]

$$n\tau_E T \geq 1.5 \cdot 10^{21} keVsm^{-3} \qquad (1.11)$$

The plasma created in reactors needs a huge quantity of energy to reach the fusion conditions imposed by the triple product; this turns into the following two requirements:

- supply the energy only to small quantity of matter

- realize a thermal insulation between the plasma and its container, not to lose the energy supplied and to avoid damaging of the container due to high thermal flux.

Summarizing it a plasma of the fusion reactants has to be created having sufficiently high temperature and density, and also it must be confined for a sufficiently long time away from any surrounding material walls. There are two main approaches for achieving this:

- **inertial confinement**: a laser is used to compress a mixture of deuterium and tritium, so that very high density is achieved for a very short time.

- **magnetic confinement**: the other possible way is to increase the energy confinement time by magnetically confining the plasma; in fact, the plasma is composed of charged particles, which are sensitive to magnetic fields in accordance to the Lorentz force that forces the particles to follow the field lines with a helical movement.

Thus far the most successful way of trapping the plasma particles along the magnetic field lines has been achieved by magnetic confinement in fusion reactors based on the Tokamak concept[1]; however other magnetic configurations like, Stellarator and Reversed Field Pinches (RFP) are possible.

With respect the nuclear fission these technologies have several big advantages in addition to those already highlighted (fuel availability):

- The fusion reaction is inherently safe. There is no danger of runaway reactions, criticality or a meltdown. At a given instant of time the total inventory of fusion materials in the device is just enough to produce the power for a few seconds. This is to be contrasted with fission reactors, where the inventory stored at a given instant is enough to cause a major explosion.

- The radioactive pollution is still present, due to the activation of materials by high energy neutrons, but the life time of the radioactive waste is hundreds of years instead of thousands of years such as for nuclear fission.

1.3 ITER Project

ITER that means "the way or the road" (from the Latin word) is the machine that will represent the first thermonuclear fusion experiment capable of producing more power than the power being delivered to the plasma by its heating systems.
The ITER project started at the end of 1985 thanks to an agreement between the European Union, the Soviet Union, the United States and Japan, with the aim of studying and developing fusion energy for peaceful purposes. Other signatories joined the project later on, such as the Republic of China and the Republic of Korea in 2003 and India in 2005. The ITER agreement was signed in 2006 and the location selected for building the reactor was Cadarache, in southern France.[4].
This reactor[Figure 1.2] will be based on Tokamak magnetic configuration in which the strongest magnetic field is along the toroidal direction and it is generated by superconductive electro-magnets placed around the chamber, then another magnetic field along the poloidal direction will be created by the current flowing in plasma itself that initially will be created by a strong induced electric field generated from a very fast flux variation provided by the central solenoid; furthermore this current is needed also to heat the plasma.
In ITER the fuel will be a Deuterium-Tritium mixture, and it will be heated up to about 10keV (150M°C);the target output power is 500MW for a pulse duration of at least 400s and it will

be obtained by about 50MW of input power, hence the so called gain factor Q, that is the ratio between output and input power, will be 10.

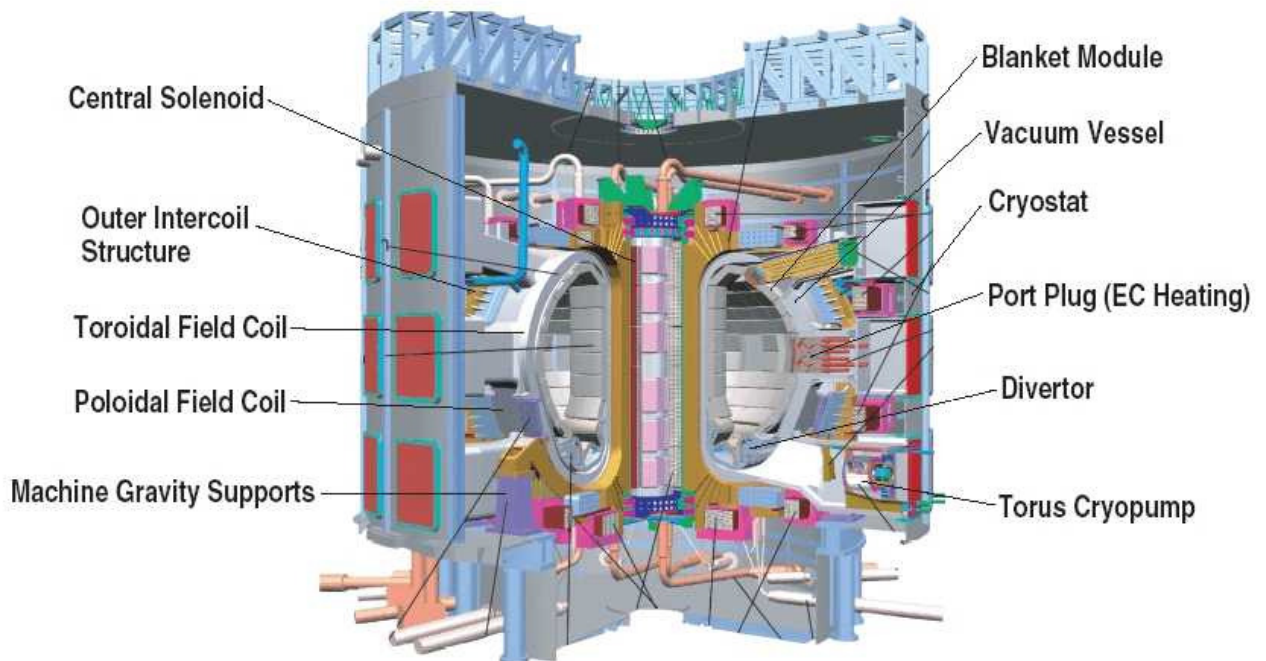## THE ITER-FEAT MACHINE

Figure 1.1 Cut view of ITER reactor.

In order to get the high temperature (10keV) needed for fusion reaction, three ways to heat the plasma are needed:

- **Ohmic heating**: the current induced in the plasma provides the heating by Joule losses that are represented by the product $R_p \cdot I_p^2$, where R_p is the plasma resistance and I_p is the plasma current. Unfortunately plasma resistivity falls with the rise of the plasma temperature since it is proportional to $T^{-3/2}$ [5] therefore other heating systems are needed.

- **Radiofrequency heating:** electromagnetic wave generators by antennas send electromagnetic waves inside the plasma with an adequate frequency, the gyro frequency of the particles or the plasma frequency that are absorbed by the plasma or generate oscillatory phenomena; in this way the wave energy is transmitted to the oscillating particles thus heating the plasma.

- **Neutral Beam Injection (NBI):** Neutral beam heating (NBH) is one of the most promising and best understood methods to heat a dense plasma and to drive plasma

13

current in fusion machines. This system will inject high energy D atoms (40A, 1MeV) inside the ITER plasma chamber and since the particles are electrically neutral they are unaffected by the magnetic field and travel along straight-line trajectories until they are ionized by collisions with the background plasma. Once ionized the neutral beam particles are partially magnetically confined then the kinetic energy carried by these fast particles is transferred to the plasma in order to increase the temperature. This system will be well described in the next section.
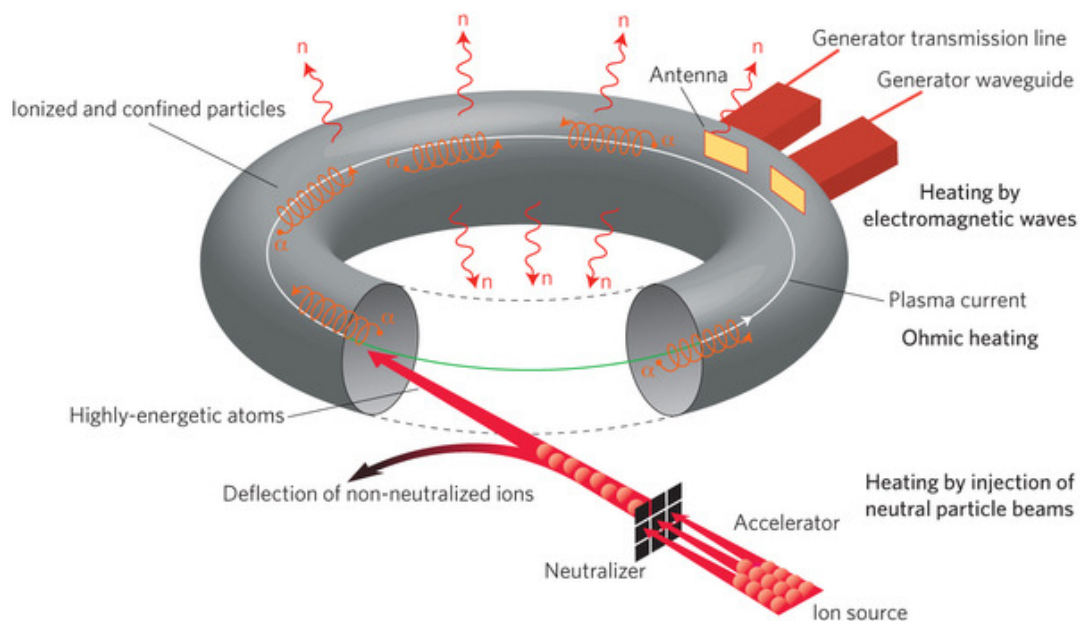

Figure 1.3 Scheme of plasma heating systems.

1.4 NBI

The heart of the NBI is the ion source, where hydrogen or deuterium ions are generated by a plasma generator, then the ions are accelerated to a desired energy by an electrostatic extractor/accelerator. The beam energy has to be significantly above the energy of the plasma particles it has to heat, and the beam has to penetrate sufficiently into the plasma to deposit its energy in the center, where the energy is lost more slowly. It has to be reminded that the cross sections for ionizing the neutral beam decrease with the beam energy, thus a higher energy beam penetrates deeper into any given plasma[6]. In the case of ITER the required beam energy is 1MeV. [7]

The accelerator is followed by a neutralizer cell in which a fraction of the accelerated ions is converted into energetic neutrals typically by a charge exchange process thanks to collisions

with the background gas. Since not all ions can be neutralized, the un-neutralized ones are removed from the neutral beam and typically guided onto ion beam dumps by a deflecting magnet. Figure 1.4 shows a typical layout for NBI.
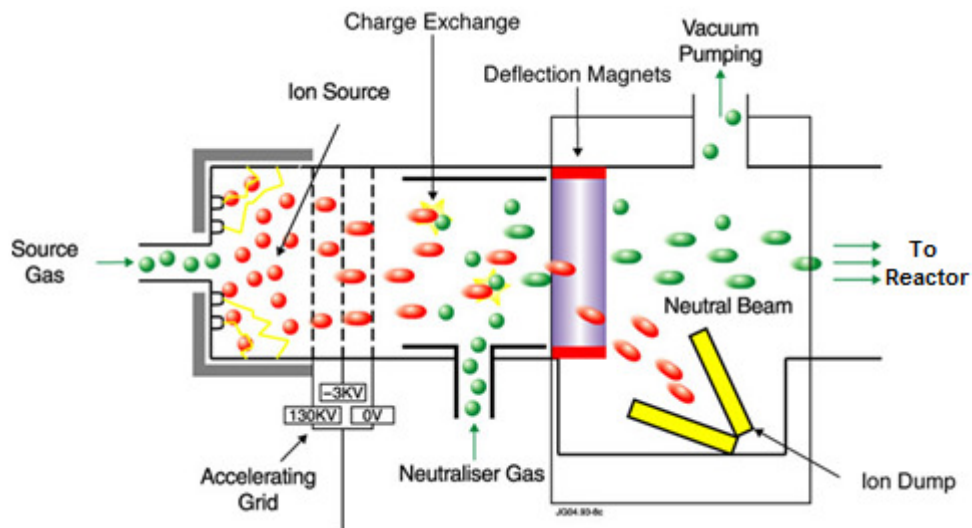

Figure 1.2 Typical layout for a NBI.

Both negative and positive ions can be employed to generate an ion beam. For the case of Hydrogen/Deuterium on the one hand producing and preserving positive ions up to the neutralizer is easier than negative ones, on the other hand the neutralization efficiency quickly decreases with increasing particle energy.

In Figure 1.5Figure 1.3[1] it can be observed that for D positive ions from about 50keV the neutralization efficiency strongly decreases compared to the negative ones and at the ITER target specification of 1MeV it is practically zero where as for negative ions it is about 60%; therefore a negative source has been chosen for ITER.
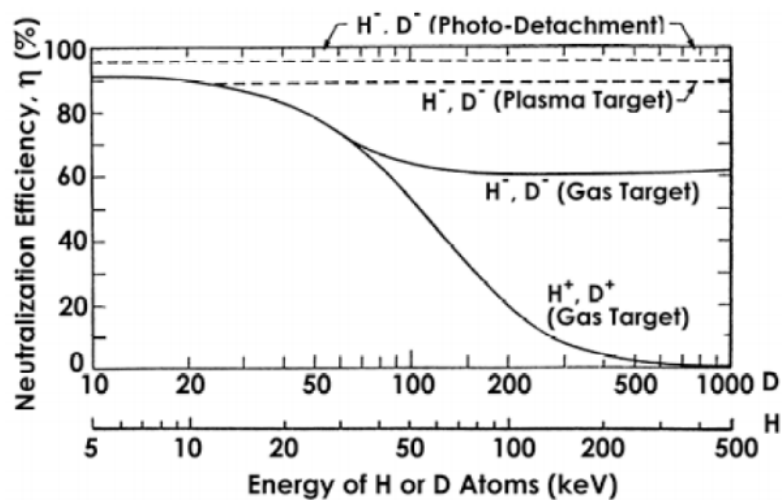

Figure 1.3 Neutralization efficiency vs ions energy for positive and negative particles.

1.5 Ion sources

The ion source for NBI is required to produce a high power ion beam of several tens of MW. To produce such a high power ion beam with high beam quality the plasma generator has to efficiently generate a dense, quiescent plasma, uniform over a wide area and at a low operating gas pressure.

Basically the plasma into ion sources can be generated in two different ways [6]:

- the first source type is composed of a hot cathode, for example made of a tungsten filament, which emits electrons by thermionic effect; the filament is electrically biased so that a plasma is generated by collisions between electrons, are forced towards the anode (the source walls) that are positive with respect to the filament, and the background gas. Tungsten filaments have to be replaced periodically in most ion sources for NBIs and the lifetime of the cathode material determines the maintenance frequency of the NBIs, moreover pollution in the plasma due to filament evaporation occurs.

- another possibility is represented by the Radio Frequency sources, in which a coil wound around the source wall is used to generate an inductive discharge. Due to the high-frequency electromagnetic waves emitted by the coil, acting as an antenna, the free electrons present in the source gain enough energy to ionize the background gas forming the plasma.

For ITER a negative RF type source has been chosen, since for the required energy of 1MeV the neutralization efficiency is larger than for positive ions [8], in which the plasma is confined by several magnets in a multi-pole configuration.

Negative hydrogen/deuterium ions are produced in two ways inside the source:

- **Volume production:** At first a neutral molecule have to be vibrationally exited by collision with a fast electron (E>20eV)

$$H_2 + e_{fast} \rightarrow H_2^*(v) + e_{fast} \qquad (1.12)$$
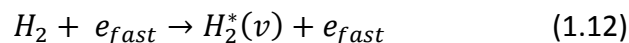
then a negative hydrogen/deuterium ions can be created by *dissociative attachment* involving a low energy electron (E<2eV) and the excited molecule as follows

$$H_2^*(v) + e_{slow} \rightarrow H^- + H^0 \qquad (1.13)$$
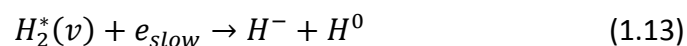
Since the binding energy of the additional electron is very weak (0.75eV) the stability of the negative ion is very low, in fact collisions with electrons with energy above 2eV destroy it.

On the other hand the cross section of the excitation reaction is greater for high electron energies, therefore the source has to be divided in two parts, a hotter upstream region called *driver*, where the main plasma heating is located and the electrons produce vibrationally excited molecules, and a colder downstream region called *extraction region*, where negative ions are produced and extracted. A magnetic filter allows to reduce the temperature of electrons diffusing from the driver ($Te>4$ eV) to the extraction region ($Te<2$ eV).

- **Surface production:** Since the survival length for the negative ions is reduced by the processes described above, the negative ion formation has to be maximized close to the extraction system where fast atoms (H^0) or ions (H^+) are converted to H⁻ions when colliding on the source walls. It has been shown that injection of cesium vapor in the source leads to a 3-10 times enhancement in H⁻production[9].This is due to the low work function of cesium (2.1 eV [10]) that forms a thin layer on the source walls thus lowering the work function of the metal surface itself on which particles hit extracting electrons. Also in this case a magnetic filter is required to reduce the density of high energy electrons near the extraction region.

Negative sources beside maximizing negative ion productions have to be polarized with negative potential with respect the extraction region, in this way only negative charges will be extracted by the electric field.
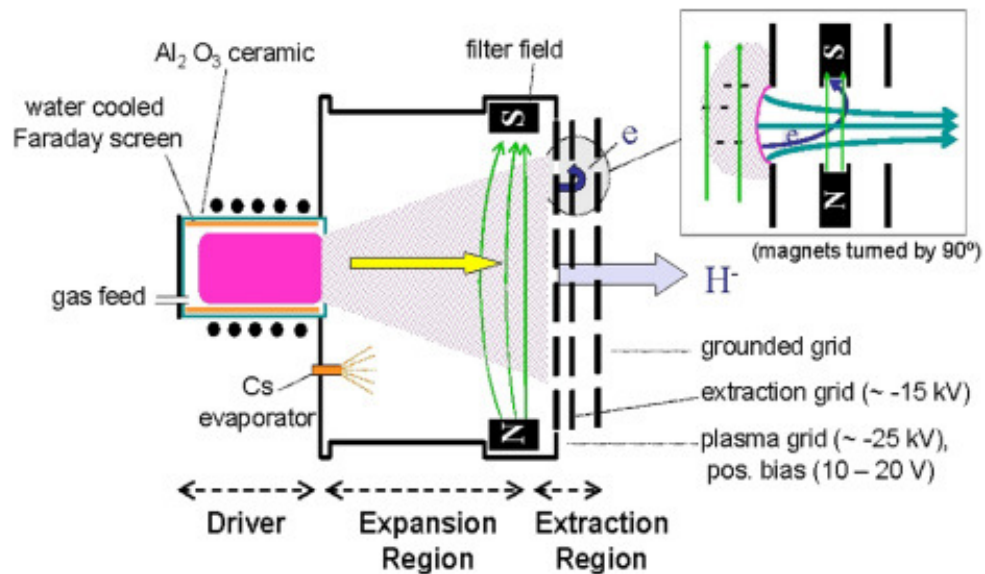A typical layout of an RF ion source is shown in Figure 1.6.

Figure 1.4 Typical layout of an RF source.

1.6 Accelerators

The principle of extractors can be understood from the simple case represented by the diode configuration [Figure 1.7][10]that consists of two electrodes polarized at different potentials. The electrode facing the plasma in the source is called Plasma Grid(PG) and it is biased more or less as the source which is negative respect to ground, the other one is at the ground potential and is called Grounded Grid(GG). In this way the electric field drive negative charges from the Plasma grid to Grounded Grid providing both extraction and acceleration of the negative particles.

The boundary region between the plasma and where the charged particles feel the extraction voltage is called *meniscus*. It is defined as the surface with a potential of zero. The shape of the meniscus should be a convex lens, which determines the initial beam quality.
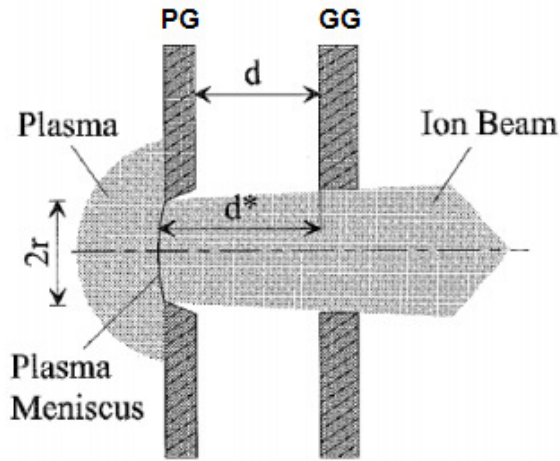

Figure 1.5 Sketch of a simple diode type acceleration system.

Maximum extractable ion current density is the amount of ions at the plasma meniscus and is determined by the balance between the electrical potential applied to the electrodes and the space charge of the negative charges between the electrodes; in fact the extractable current density cannot grow without limit but saturates since the negative charges accumulated in the extraction region screen the electric field as expressed by the Child-Langmuir Law [1] in Eq. 1.14 which is valid in the case of a planar and infinite emission area and of ions having zero initial energy along the longitudinal direction:

$$j_i{}^{max} = \frac{4}{9}\varepsilon_0 \left(2\frac{Ze}{M}\right)^{\frac{1}{2}} \frac{V_{ext}^{\frac{3}{2}}}{d^2} \tag{1.14}$$

where V_{ext} is the extraction voltage applied to the electrodes, d is the distance between the electrodes, Z is the ion charge number and M is the ion mass number.

It should be noted that the maximum ion current density $j_i{}^{max}$ increases as a function of the extraction voltage as $V_{ext}{}^{3/2}$.

Analogously the ion current extracted from a circular aperture of radius r is given by 1.15:

$$I_i{}^{max} = \pi r^2 j_i{}^{max} = \frac{\pi\epsilon_0}{9}\left(2\frac{Z_e}{M}\right)^{\frac{1}{2}}\left(\frac{2r}{d}\right)V_{ext}^{\frac{3}{2}} \tag{1.15}$$

The previous equation can be written as:

$$I_i{}^{max} = P_0 V_{ext}^{\frac{3}{2}} \tag{1.16}$$

where the coefficient **P₀** is called the "*perveance*" of the extraction system.

In a real ion beam the current density in (1.14) depends on the ion density at the plasma meniscus, furthermore the distance d^* between the meniscus and the extraction electrode has to be used in place of d in (1.15), for example for a concave boundary as in Figure 1.7, d^* >d and the beam perveance P^* that considers the real current instead the maximum theoretically available is reduced with respect to P_0.

To describe the beam optics, as reference parameter the normalized perveance P*/P₀ is applied, due to its correlation with the *beam divergence*, which is an index of the beam widening caused by the space charge expansion.

Assuming that the distribution of the angles between the beam axis and the velocity vector of the beam particles after the extraction system is a Gaussian distribution with standard deviation σ, the divergence angle ε is defined as:

$$\varepsilon = \sqrt{2}\sigma \tag{1.17}$$

Generally, the beamlet divergence ε depends on the perveance (hence on the extracted current and the extraction voltage).

The optimum normalized perveance condition is reached when the divergence is at its minimum value: with increasing P*/P₀, the divergence decreases (this region is called *under-perveant region*) reaching its minimum, then it increases again (*over-perveant region*). As the extraction system can be considered as a system of electrostatic lenses, the normalized perveance is connected to the focus point of the beam. This explains also the dependence of the divergence on the normalized perveance: three cases with different perveances are shown in Fig. 8 where the optimum value is shown in the central image.
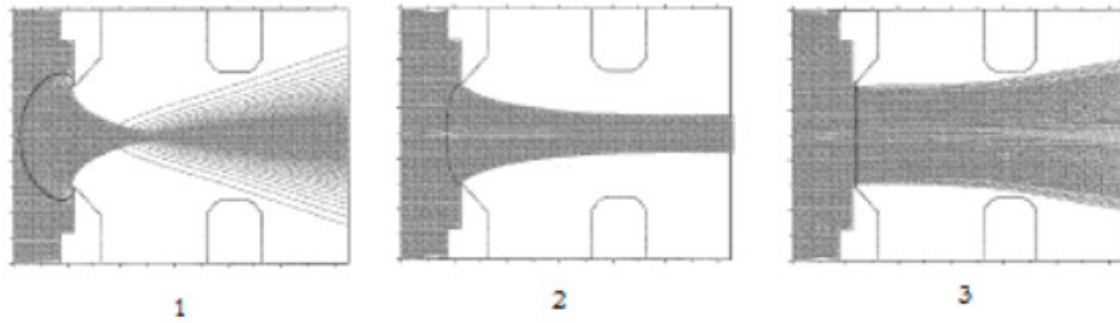
Figure 1.6   Sketch of the beamlet shape for three different cases where focus point is: too close to the PG (1), downstream to the EG   (3), nearby the EG (2) and this is correlated to a good optics.

In order to increase the maximum current with respect to the optimal value according to the Child-Langmuir law, while keeping as low as possible the beam divergence, more sophisticated extraction systems are used, for example the triode type, in which a third electrode called extraction grid (EG) is placed between the plasma grid and the grounded grid in which divergence is function of normalized perveance and on the ratio of the extraction voltage (voltage between PG and EG) to the acceleration one (voltage between PG and GG).

$$\epsilon = F\left(\frac{P^*}{P_0}, \frac{V_{ext}}{V_{acc}}\right) \qquad\qquad (1.18)$$

The ion sources for NBIs use a triode acceleration system (SINGAP) for low acceleration energies (e.g. less than 50 kV). As the required energy increases, with triode acceleration it becomes difficult to produce high power density beams due to electrical breakdown problems among the grids. For higher energy acceleration, a multi-stage acceleration system has been used. Compared with the triode acceleration system, a multi-stage system has additional grids called "gradient grids" or" intermediate grids", which reduce the breakdown problems and provide the capability of electrostatic focusing[1]; a scheme of a multistage accelerator (MAMuG) compared with a triode (or single stage) is shown in Figure 9:
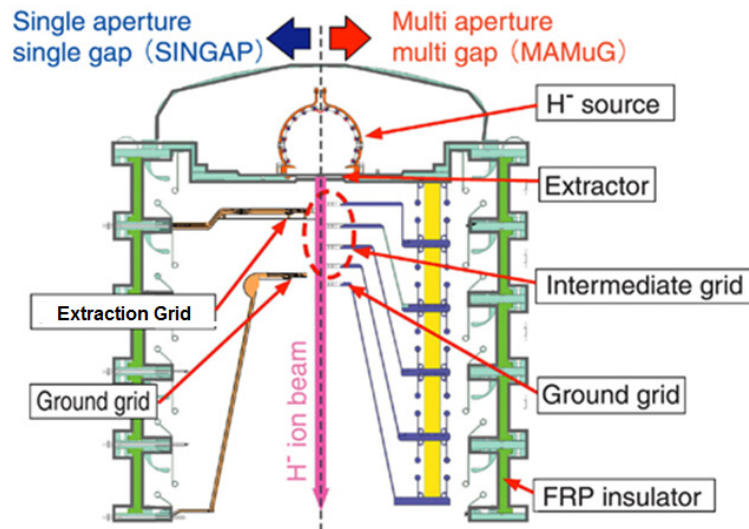
Figure 1.7 Sketch of SINGAP (left section) and MAMuG (right section) configurations.

Since the electrons have the same charge as the negative ions and a lighter mass, electrons are extracted and accelerated with the negative ions. Effective suppression of the electrons is critical in negative ion extraction.

In order to decrease the amount of co-extracted electrons, the plasma grid is biased positively against the source body (10-20 V). The beneficial effect is more pronounced by introducing an additional plate (*bias plate*, BP) in front of the plasma grid on the plasma side. The bias plate is electrically connected to the source walls: it decreases the biased area by extending the source potential near the apertures.[11]

The negative ions are extracted together with the electrons by applying an extraction voltage between the plasma and the extraction grids. Electrons are deflected by the dipole magnetic field produced by permanent magnets embedded in the extraction grid and deposited on the extraction grid itself.

Negative ions are scarcely deflected due to their higher mass and go through the extraction grid. The extraction voltage is selected up to 10 kV, because a higher voltage causes higher electron energy, resulting in a high heat load over the extraction grid; moreover another electrode so called *Repeller* can be present after the Grounded Grid, it is slightly positively biased in order to suppress the back-streaming of positive ions created after the acceleration column due to the ionizing of the background gas due to the beam particles.

1.7 PRIMA Facility

Padova Research on ITER Megavolt Accelerated (PRIMA) identifies all the R&D facilities that will be realized and hosted at Consorzio RFX in Padova in the framework of international

agreements with all the different actors: ITER Organization, Europe and the Host (Consorzio RFX) with contributions from the other ITER Parties, Japan and India, directly involved in the procurements of the neutral beam systems. The PRIMA activities include the design, construction, installation and exploitation of two experimental test stands: the ion source SPIDER and the neutral beam injector MITICA; the aim of this Facility is to develop a reliable NBI system for ITER.

SPIDER

SPIDER (Source for Production of Ions of Deuterium Extracted from Rf plasma) will be a radiofrequency (RF) ion source with the same characteristics expected for the ITER NBI but with beam energy limited to 100 keV in a SINGAP configuration. SPIDER mission is to increase the understanding of source operation and to optimize the source performance [12] and in particular to develop:

- the necessary ion current density
- the lowest possible pressure
- the required uniformity
- the lowest percentage of co-extracted electrons
- pulse duration

The SPIDER nominal parameters are reported in Table 1.1 and an overall picture of the whole experiment can be seen in Figure 1.8.

SPIDER	H	D
Beam energy [keV]	100	100
Maximum Beam Source pressure[Pa]	<0.3	<0.3
Uniformity [%]	±10%	±10%
Extracted current density [A/m^2]	>350	>290
Beam-ontime [s]	3600	3600
Co-extracted electron fraction(e$^-$/H$^-$ or e$^-$/D$^-$)	<0.5	<1

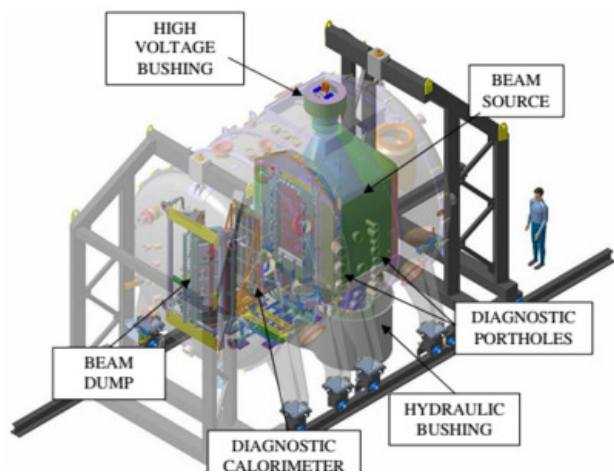**Table 1.1 Design requirements of SPIDER**

Figure 1.8 SPIDER rendering

MITICA

MITICA (Megavolt ITER Injector & Concept Advancement) is the full-scale prototype of the ITER injector, with a similar scheme, layout and power supplies. MITICA will aim to study the whole injector operation, including the beam acceleration, focalization and neutralization. [12]

The injector is being designed in order to be able to produce a beam of neutral particles of deuterium, accelerated up to the energy of 1 MeV by means of an electrostatic accelerator with an acceleration voltage of 1 MV in a MAMuG configuration.

The beam shall be able to transfer a power of 16.5 MW to the plasma for 3600 s, continuously.

Diagnostics, as well as in SPIDER are essential in MITICA to qualify and optimize the NBI for ITER and to assess the amount of information on the source and beam that cannot be gathered by means of the reduced set of diagnostics, mainly thermocouples, available on the real ITER NBI.

Main technical specifications are shown in Table 1.2

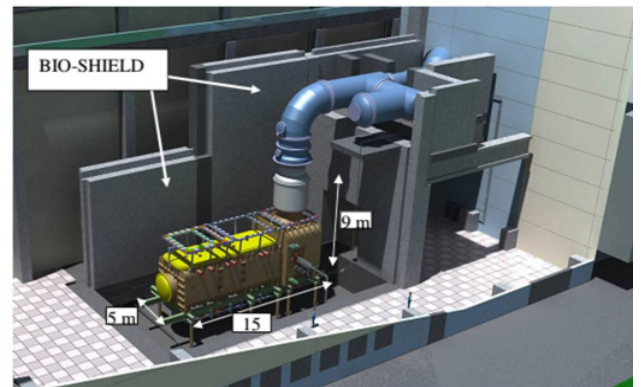| MITICA	H	D
Beam power[MW]	16.5	16.5
Beam energy [MeV]	1	1
Maximum Beam Source pressure[Pa]	<0.3	<0.3
Acceleration current [A]	49	40
Beamlet divergence [mrad]	≤7	≤7
Beam-ontime [s]	3600	3600
Co-extracted electron fraction(e^-/H^- or e^-/D^-)	<0.5	<1

Table1. 2 Design requirement of MITICA

Figure 1.9 MITICA rendering

2 NIO1 experiment

NIO1 (Negative Ion Optimization phase 1) is a relatively compact, modular and very flexible radio frequency type ion source developed by Consorzio RFX and INFN (Laboratori Nazionali di Legnaro).

The aim of this experiment is to provide a test-bench in the framework of the NBI test facility described in 1.7, in particular the target is to investigate the optimal configuration for ion beam production, to analyze the main issues regarding electrostatic accelerators and to validate relevant numerical codes.

The experiment is capable of producing 9 beamlets each having 15mA of H^- accelerated up to 60kV and extracted from 9 apertures of 3.8mm radius arranged in a 3x3 square matrix for a total area of about $400mm^2$ providing an ion current density of $300A/m^2$ as nominal ratings.

NIO1 is composed of 3 main parts:

- the source, in which plasma is generated by an RF coil
- the accelerator, based on a triode system, in which negative charge particles are extracted from the source and accelerated
- the diagnostic tube where many beam diagnostics can be placed.

The source is a tower of several disk assemblies sealed by O-rings and connected in tower configuration forming a cylindrical chamber with a radius of 5cm in which plasma is generated by a water cooled RF coil made of 7 copper turns made from a pipe with 6mm external diameter wound around an alumina cylinder of 78mm height forming the source chamber.

The coil is coupled to the source and it can provide a power up to 2.5kW at the adjustable frequency 2MHz ± 10% and it is embedded in a Polysulfone shell to keep the turns in place; an air flow is injected inside the shell in order to cool mainly the alumina cylinder.

In the source walls magnets are inserted, arranged in a multipole configuration with a periodicity of 7 in order to confine the plasma; they are water cooled by several independent circuits.

The source is provided with some vacuum windows, four just 26mm before the Plasma Grid with lines of sight (LOS) parallel to the grid and four in the back side with LOS parallel to the beam direction; furthermore other apertures are present respectively for cesium injection and for the gas inlet where also the pressure gauge (Pirani sensor) is connected. A sketch of the source is shown in Figure 2.1.
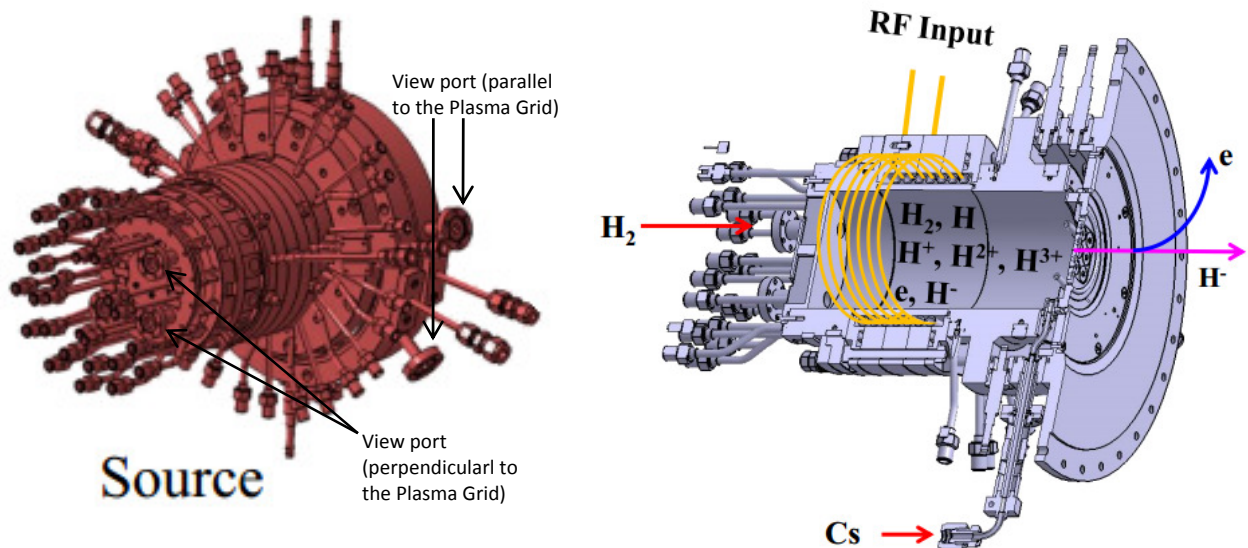
Figure 2.1 Source overview.

Two additional components are present in the source block:

- **Plasma Grid**
- **Bias Plate**

As regards the Plasma Grid (PG) it is at the source output, facing the plasma; it is a copper plate, with 9 holes having 7.6mm diameter arranged in a 3x3 matrix and spaced by14mm, electrically insulated from the source; in this way the PG can be biased at some volts (≤30V) with respect to the source; more precisely in NIO1 the reference potential is the Plasma Grid, which can be polarized up to -60kV with respect to ground.

The bias plate is located just before the PG and it is composed by two different insulated elements:

- "*magnetic bias plate*" that is a sort of rectangular frame and it provides the return path for the current of the magnetic filter so called Plasma Grid Filter (PGF) and coming from PG that acts so as to deflect hot electrons reducing the amount extracted through the PG holes.
- "*electrostatic bias plate*" that is a round frame, exposed to the plasma, that can be biased up to 20 V with the aim to attract electrons by modifying the charge profile in the source in the meniscus zone.

The whole assembly is shown in Figure 2.2 (right) and is called generically Bias Plate, then Plasma Grid is shown in the left side of the figure.
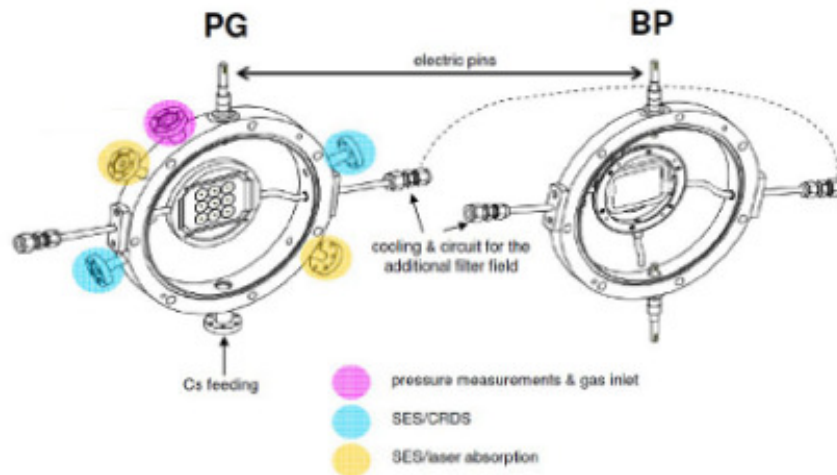
Figure 2.2 Plasma Grid and Bias Plate.

The acceleration column basically is made of:

- **Extraction Grid (EG)** which can be biased with respect to Plasma Grid up to +9kV (-51kV from ground reference), in this way negative charges coming from plasma grid are extracted and partially accelerated, moreover the polarization voltage is completely tunable from 0 to 9kV allowing to adjust the beam optics (divergence of the particle trajectories).Like Plasma Grid it is made of copper and 9 holes in a 3x3 array are present in order to let the particles go through it; with the purpose to deflect co-extracted electrons 4 magnets are embedded inside the grid with magnetic axis along the direction of the beam with alternating polarity; the magnets are arranged in the vertical direction.

- **Post acceleration grid (PA)** that is built like the others and is at the ground potential

- **Repeller grid** is placed just after the PA and can be biased with positive voltage (up to 150V) with respect to ground in order to prevent positive ions (generated by background gas stripping for example) from going into the accelerator where they would be accelerated upstream up to the source damaging it by sputtering.

All the grids are water cooled and the extraction grid is insulated from post acceleration grid by two insulating ceramic rings made of alumina; another ring insulates the EG from the PG.
Finally the third part is the diagnostic chamber (NIO Vessel) that is a metallic tube (length=1.5m inner diameter= 350mm), connected downstream to the acceleration column, in which several view ports are present for different diagnostics to be used to characterize the beam; moreover inside the diagnostic tube the beam dump is placed, which can be a cooled copper plate or a carbon fiber composite tile, described in the next section, used for calorimetry purposes; then a turbo-molecular pump and a scroll pump are connected to one

flange (on the pumping cross) in order to keep the pressure in the apparatus at a controlled value and also a dual pressure gauge (Pirani and Ionization) is present. In Figure 2.3 a view of main components described above is shown.
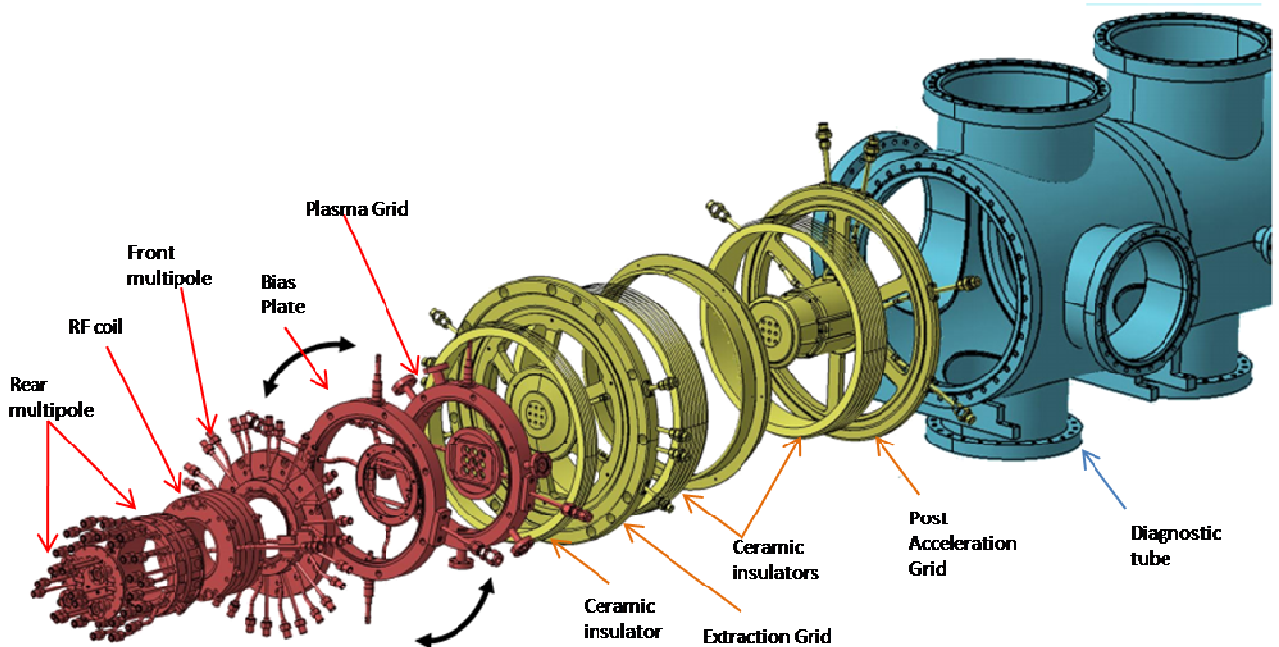

Figure 2.3 NIO1 Exploded view drawing of NIO main components.

2.1 Diagnostics

In NIO1 many diagnostic systems are expected to be installed; up to now some of them are already present. Here a brief description of the diagnostics not already implemented will be given in order to show the full potentiality of the experiment; then more focus will be placed on the diagnostics employed in the current experimental campaigns. In Figure 2.8 an overview of the main diagnostics already installed and planned is shown.

Diagnostics will be installed both to analyze the plasma characteristics in the source and the particle beam exiting the accelerating column; they are summarized below:[5]

- **Optical emission spectroscopy (OES):** from the radiation spontaneously emitted during the interaction of molecules or atoms in the source or of the beam with the background gas a great variety of plasma parameters can be deduced like impurities in the plasma, electron temperature and density, neutral hydrogen and cesium density. To evaluate these parameters, currently on NIO two spectrometers are installed: the

first one is a low resolution spectrometer (HAMAMATSU mini-spectrometer), with a wavelength resolution of 1nm in the spectral window from 200nm to 800nm.anda high resolution spectrometer (CINEL) with 0.05nm resolution in a spectral window of several tens of nm in the visible region.

- **Plasma light detection (PLD):** this diagnostic can be based both on a photodiode or a photomultiplier and provides useful information about the plasma state; for example plasma ignition or switch-off can be detected as well as the type of plasma coupling with respect to the RF field (E-mode or H-mode)[6] and in general the plasma dynamics.
  On NIO1 a photomultiplier module (PMT) is present, connected to one of the rear ports in the plasma source; the light emitted by the plasma is collected by means of an optical head which focus the light into an optical fiber of 0.4mm diameter connected to the PMT. This device collects photons and generates electrons (photoelectric effect) which are multiplied thanks to the secondary emission phenomenon in order to have a suitable value and finally they are collected at the PMT output as a current proportional to the input light. This current is converted into a voltage by a trans-impedance amplifier with a gain of 1V/µA, then the voltage at the output of the PMT is processed by a home-made amplifier with tunable gain which amplifies the signal up to 2 orders of magnitude providing the required output for the acquisition system indifferent light intensity conditions.

- **Luxmeter:** Also this diagnostic is employed to measure the light emitted from the plasma in the source as a cross check with the PMT, its line of sight is parallel to the beam axis since it is installed in one of the rear ports of the rear multipole.

- **Beam emission spectroscopy (BES):** It allows to verify if the ion beam is present, then uniformity and divergence can be evaluated. This technique is based on the interaction of energetic ions with the molecules present in the background gas inside the diagnostic chamber.
  When an energetic ion hits a neutral particle, it receives an electron from the background gas particle and reaches the excited neutral state; therefore a photon will be emitted in correspondence to de-excitation of the atom. The most intense emitted radiation corresponds to Hα transition of the Balmerlines.[7].
  In the frame of reference of the laboratory the velocity of the particles causes a shift in the wavelength of the peak due to Doppler effect, hence the peak that has to be measured is at the wavelength expressed from the following equation:

(2.1)

$$\lambda' = \lambda_0 \frac{1 - \beta \cos(\alpha)}{\sqrt{1 - \beta^2}}$$

where λ' is the shifted wavelength, λ_0 is the unshifted one (656.2nm for Hα), β is the ratio between the speed of ions and the speed of light (calculable from the potential between the PG and PA grids) and α is the angle between the observation direction and the direction of motion of the de-excited neutral.

In NIO1 BES is performed by the high resolution spectrometer whose optical heads can be installed both in horizontal and vertical position with respect to the beamlet direction and for each view port three different LOSs aligned with the 3 beamlets will be installed in order to study each one of the 9 beamlets.

Thus, by measuring the distance between the shifted and unshifted peaks, β can be evaluated and so also the direction of the beamlets. Divergence and uniformity can also be calculated by other equations [7].

- **Fast emittance scanner (FES):** It will measure the beam particle velocity distribution; in NIO1 an Allison Scanner has been chosen to perform the measurement, which will be placed at 0.46m from the plasma grid either in the vertical or horizontal position.

- **Mini-STRIKE:** This diagnostic is currently installed on NIO1, it is a Carbon Fiber Composite (CFC) tile with dimensions of (120 x 90 x 12) mm^2 Figure 2.4 in which thermal conductivity exhibits anisotropic behavior, in fact the tile conducts mainly along the fiber direction, or rather along its shorter side, and much less in the plane perpendicular to the fibers.

Figure 2.4 Mini-Strike calorimeter: the CFC tile.

Mini-STRIKE is arranged in the diagnostic tube just after the pumping cross [Figure 2.8] with horizontal orientation and is perpendicular to the beam direction with the fibers parallel to it. The aim of this diagnostic is to evaluate the intensity pattern of the beam impinging on its surface: the beam deposits a thermal flux (on the tile surface facing it) proportional to its intensity distribution, hence a thermal pattern will be present on the front side. Since the thermal flux crosses the tile mainly along the fiber direction,

the thermal pattern on the back side [Figure 2.5] will be just slightly distorted; therefore it can be observed by an infra red (IR) camera, and then by means by an inversion algorithm[1], the thermal flux at the front side and thus the beam intensity can be calculated.

On NIO1 the thermal camera is located outside the diagnostic chamber in front of the end of the tube and observes Mini-STRIKE by means of a dedicated view port.

The study of this diagnostic is collocated in a wider framework since in SPIDER a bigger CFC calorimeter so-called STRIKE (Short-Time Retractable Instrumented Kalorimeter Experiment) will be installed[2].
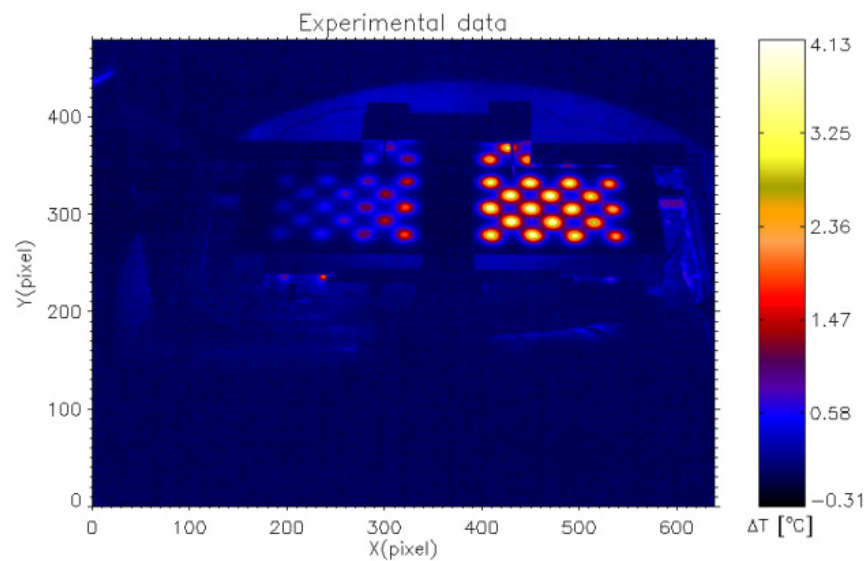

Figure 2.5 Typical thermal pattern on mini-STRIKE backside.

- **Thermocouples:** Since in NIO1 a lot of components in contact with plasma is water cooled, like the grids of the acceleration column and the source, it can be possible to measure the difference of temperature between inlet and outlet water of each cooling circuit which will be proportional to the power (or part of it)deposited by the plasma onto each component (or part of them).

  For example in the source there are five cooling groups respectively four in the front multi-pole and one in the rear multi-pole, and for the Extraction Grid assembly the cooling system is made of 4 circuits : two for the flange and two for the copper grid as shown in Figure 2.6 where the water flow paths are signed; it is clear that the particles impinging on the grid deposit a power proportional to their flow and to their energy, hence it is possible to evaluate the intensity of the beam particles by thermal equations if the inlet and outlet temperatures are known.
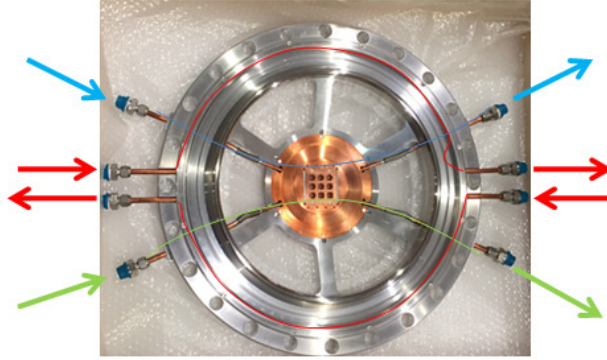
Figure 2.6 Extraction grid cooling circuit.

In NIO1 thermocouples (TC) have been chosen to measure these temperatures both for calorimetry and protection purpose; furthermore this type of thermal transducer has been adopted in order to test it in a very noisy environment (due to RF and electromagnetic field produced by plasma), where also many components are biased at high voltages; this represents a useful test-bench for thermal measurements in SPIDER in which several hundreds of TCs are being installed.

Currently on NIO1 8 thermocouples are placed distributed on the cooling circuits of the source, Plasma Grid and Extraction Grid. E type has been selected for their high sensitivity as reported in chapter 4 where also practical issues related to the current installation are discussed and a new design for the conditioning circuit board is presented.

In future it is planned to extend the use of thermocouples also on Mini-STRIKE in order to have a cross-check measurement with the thermal camera.

As regard of those diagnostics not already implemented and planned we have:

- **Laser absorption diagnostic (LAD):** It is based on the absorption spectrum of a laser tuned to the resonant transition (852nm)of atomic cesium. This diagnostic can measure the neutral cesium density wandering inside the source with no plasma, unlike OES. This fact is crucial because the two diagnostic systems measure different parameters: OES requires the plasma but in that case a lot of cesium would be at ionized state hence it will not be detectable by LAD.

- **Cavity ring down spectroscopy (CRDS):** It allows to measure the negative ion density in the source; CRDS consists in two highly reflecting mirrors mounted in two collinear vacuum windows. A laser pulse is forced to bounce between the mirrors several times. If negative ions are presents, the laser pulse is gradually absorbed by the photo detachment phenomenon in which the energy of the photons is transferred to the ion that therefore loses the additional electron. Finally by comparing the decay of the light intensity with and without plasma (even without plasma the light decays due to the

fact that the reflection coefficient of real mirrors is slightly less than 1) and measuring it by means of the light leaking through one of the mirrors the negative ion density can be evaluated.

• **Visible tomography:** This diagnostic will be used in order to obtain the intensity profile of the beam by means of two CCD (Charge-Coupled Device) cameras placed in two view ports which will be able to measure the integral of Hα radiation along many LOSs; then an inversion algorithm is used to compute the spatial distribution of the emissivity.

• **Static calorimeter:** Another NIO1 actively cooled component is the static calorimeter[3]. It consists of a copper plate target with 13 parallel tubes inside. The tubes which have a diameter of 6mm are spaced by 5mm and continue out of the plate towards the rear side where cooling circuits can be connected [Figure 2.7].
By measuring the difference of temperature of the water between the inlet and the outlet of each tube with two thermocouples, the power deposited by the beam **P$_{th}$** can be calculated with the following equation [Eq.2.2] where **$\dot{m}$** is the water flow rate and **c**is the specific heat of the water.

$$P_{th} = \dot{m}\,c\,(T_{out} - T_{in}) \qquad (2.2)$$
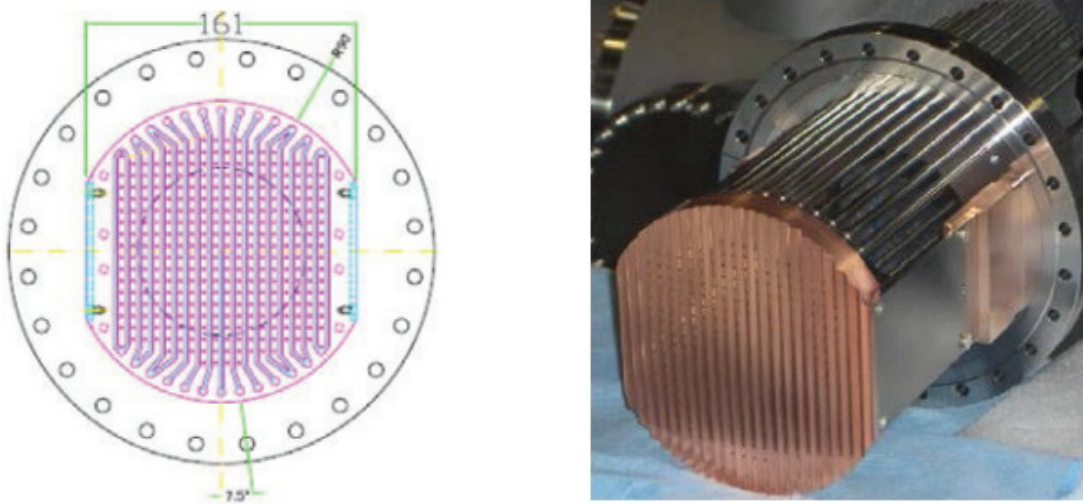

Figure 2.7 Static copper calorimeter.

This calorimeter can be rotated by 90°C in order to measure the 2D pattern of the beam by combining the two measurements; since the calorimeter is in vacuum and it cannot be rotated without vacuum losing, the two measurement have to be done in the same conditions. This calorimeter can be used for cross checking with Mini-STRIKE and tomography as regards the intensity pattern of the beam.

The calorimeter hosts also a square matrix of 1.5 mm diameter holes, through which part of the impinging particles is transmitted to a molybdenum pinhole mask on the back side; then a scintillator and a CCD camera are placed behind the mask in order to estimate the beam emittance pattern.[5]
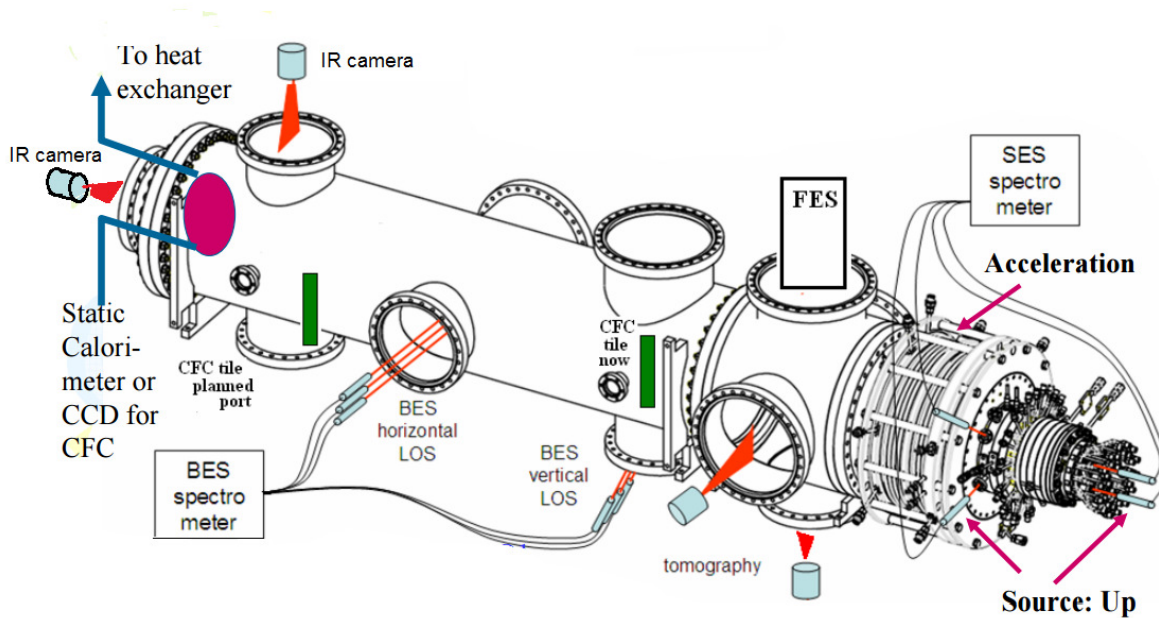
2.8 Overview of the NIO diagnostics [4].

An overview of the whole installation is given in Figure 2.9: an insulation transformer powers the equipment at source voltage, in particular the high voltage deck positioned near the ion source. This contains the RF generator and its matching box, the EG grid voltage supply, the high current supplies for biasing the source electrode, gas regulation and measurement of the source pressure and supports the source cooling connections.

On the High Voltage Deck also the Digital Acquisition Rack (DAQ) is present where diagnostics and components sitting at high voltage are connected; then the signals are insulated and the system can communicate optically with the external PCs of the control desk where the operators work.

For safety reasons (X-ray emission) the HV deck, the source and the diagnostic chamber are surrounded by lead shielding and the whole experimental area is locked during operation.
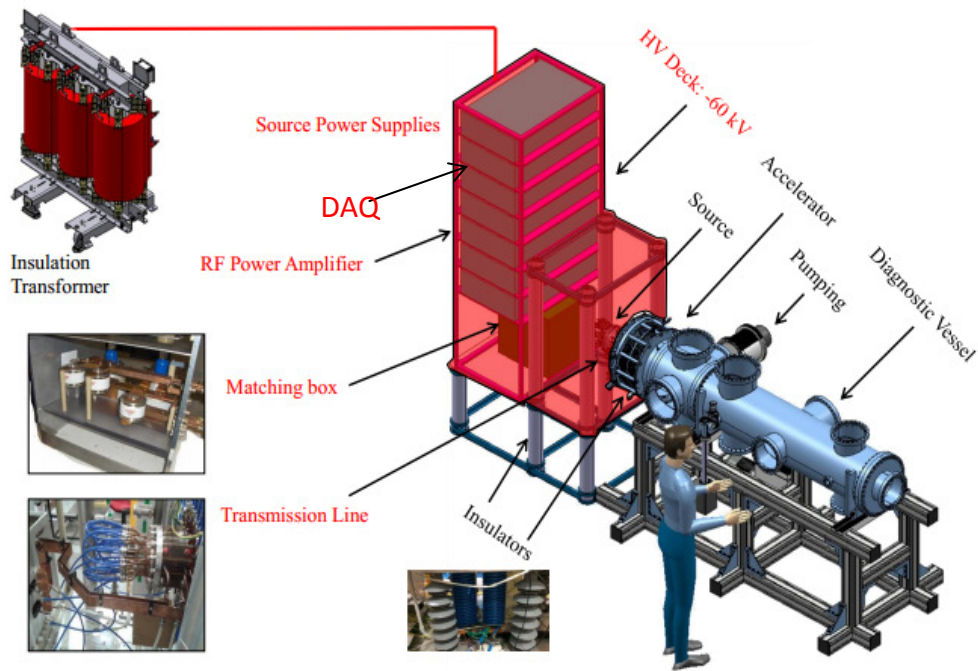
Figure 2.9 NIO overview.

2.2 High voltage circuit

The electric circuit of NIO1 consists of several power supplies and components. In this section a description of the main elements is made.

In NIO1 the plasma source operates at high potential (up to -60kV voltage) and the beam extracted is accelerated and hits the beam dump (CFC tile) which is at ground potential. The beam is extracted from the source by a 10kV HV power supply called extraction grid power supply (EGPS) connected between the plasma grid (PG) and extraction grid (EG), the acceleration of the beam is powered by the Acceleration Grid Power Supply (AGPS) connected between the PG and ground. A sketch of HV circuit with power supplies and grid connections is reported in Figure 2.10.
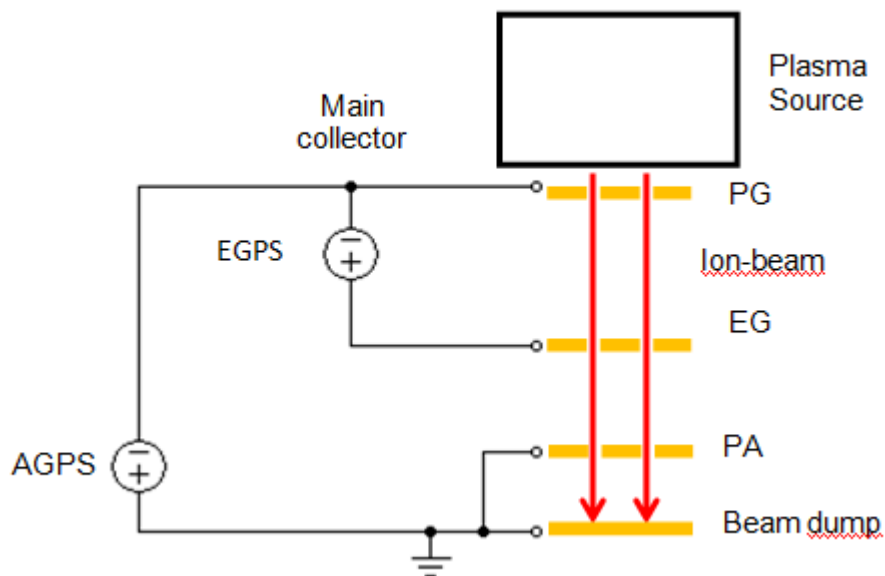
Figure 2.10 HV circuit basic layout.

The power supply and diagnostic equipment is working at the ion source potential, thus the facility was equipped with a high voltage platform called High voltage Deck (HVD), insulated from ground potential by ceramic insulators, where all these components are installed. Then the devices on the HVD are fed by an insulation transformer (70kV and 50kVA). A detail view of the system is visible in Figure 2.11. In the picture are detailed also the connections and the components of other systems of NIO1:the Bias Power Supply (BPS) and the Bias Plate Power Supply (BPPS) which will polarize the plasma source and the Bias Plate (currently BPPS is used to adjust the valve for the gas injection, so that the bias plate is connected to the source walls)with respect the Plasma Grid, finally the Plasma Grid Filter Power Supply (PGFPS) which is an high current power supply.

Since the HV power supplies have a "High Voltage Multiplier Stage" made of high voltage diodes and capacitors in which rectification and multiplication of the voltage are performed, a resistor with suitable value, called bleeder resistor, is connected in parallel to the HV output in order to insure dissipation of the electrostatic energy stored in the capacitors when the output is off.

The value of these resistors have to be a compromise with respect to the time needed to discharge the HVPS and the current drained during the normal operation where the output is active.

On NIO1 two bleeder resistors (R_{ap} =300MΩ, R_{bp}=4x50MΩ) are present respectively at the AGPS and EGPS output.

Two high voltage dividers are present, the first one polarizes with respect to the PG a spacer flange placed between the two alumina isolation rings embedded between the EG and the vessel; since the first resistor is placed in parallel both to the ring insulating EG and PG and to the first ring located between EG and PA whereas the second resistor is in parallel only to the second ring between EG and PA the polarization resistors do not have same values (440MΩ

and 360MΩ) in order to keep more voltage on the thicker one. The other divider, $R_{bp,}$ is made of 6 series resistors (which are also bleeder resistors), 50 MΩ each, connecting the HVD to ground and polarizing the H_2 pipe which feeds the source.

Another power supply placed on the HVD is the Radio Frequency Power Supply called RFPS which is connected to the Matching Box (MB), which contains adjustable capacitors, and is needed in order to have a good coupling between the RFPS and the plasma in the source; then a transmission line connects the MB to the RF coil.

Main characteristics of the power supplies are shown in Table 2.1

Power Supply	Model	Specifications
AGPS	Spellman ST 70	-70kV voltage 171mA current
EGPS	Spellman SR 10	10kV voltage 600mA current
RFPS	Comdel Cx 2500	2.5kW 2MHz±10%
BPS	TDK-Lambda Gen 30-50	30V 50A
BPPS	TDK-Lambda Gen 20-70	20V 70A
PGFPS	TDK-Lambda Gen 8-400	8V 400A

Table 2.3 Main specifications of power supplies.

Finally also connections to ground are shown in Figure 2.11, in particular an earthing switch and two earth sticks.
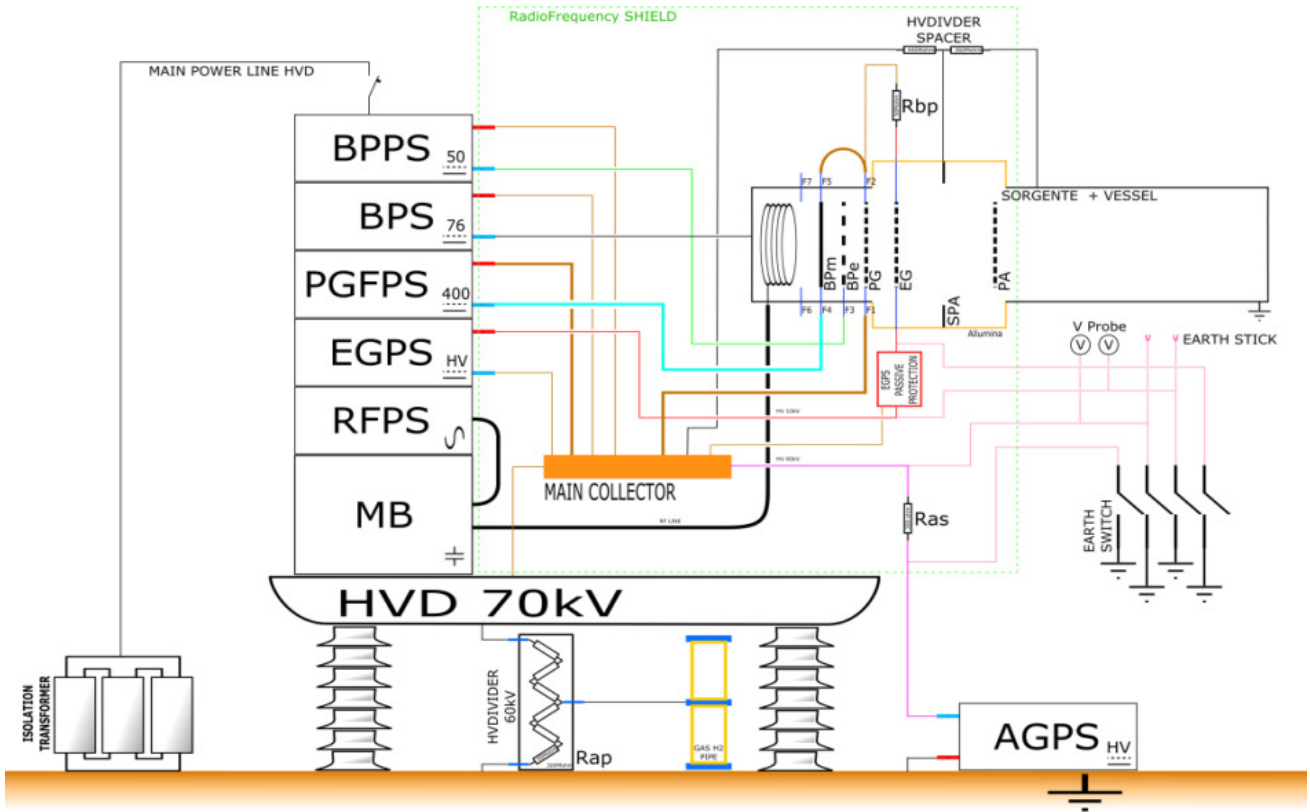
Figure 2.11 Whole electric circuit of NIO1.

3 Upgrades and first operations

In this chapter, several upgrades implemented on NIO1 during the thesis period will be presented; special focus will be placed with respect to the high voltage electric circuit on which electrical tests were conducted in order to characterize the discharge profiles with the aim to test the new protection circuits previously designed, Fast Protection Unit and Passive Protections. Furthermore 2 current sensors for Fast Protection Unit, two Rogowski coils, were built, tested, analyzed and characterized.

Finally the Electrostatic field generated by NIO1 during high voltage operations was evaluated and a map of values in different zones was made. Finally the improvement of the limits of the magnetic filter in the source (Plasma Grid Filter) will be described.

3.1 Vacuum leak recovery

NIO1 operations stopped in July 2015 since the alumina cylinder embedded in the source cracked, probably due to an imperfect alignment in the source assembly combined with the relatively high thermal power deposited by the plasma on it, since the RF power supply was used at the highest value reached so far, 1700W.

In order to understand the order of magnitude of the thermal specific flux deposited by the plasma particles on the source walls it has been evaluated from the following equation[1] that is valid in the case in which all particles (Maxwellian population) orthogonally hit the surface.

$$q = n \sqrt{\frac{2(k_b T)^3}{\pi m}}$$

where n is the plasma density, k_b is the Boltzmann constant and T and m are respectively the temperature and the mass of the particle species considered.

In the present case the thermal effect of ions can be considered negligible since they are cold; electron temperature and density have been evaluated[2] and for the pressure of 2.4Pa and 1700W were n=$2 \cdot 10^{17}$ [1/m^3] and Te=3eV; therefore q has been calculated in q= 55641W/m^2.

Afterwards it has been assumed that just about 1/2 of the potential heat flux was deposited on the alumina surface since electrons are magnetically confined since the RF field is mainly along parellel direction to the cylinder axis.

Then since the Alumina cylinder is 78mm long (L) and has an inner radius of 50mm the total inner surface has been calculated in 245 cm^2 Figure 3.1, then with the calculated flux the total power deposited on the surface $\dot{Q}$ was about 680W.
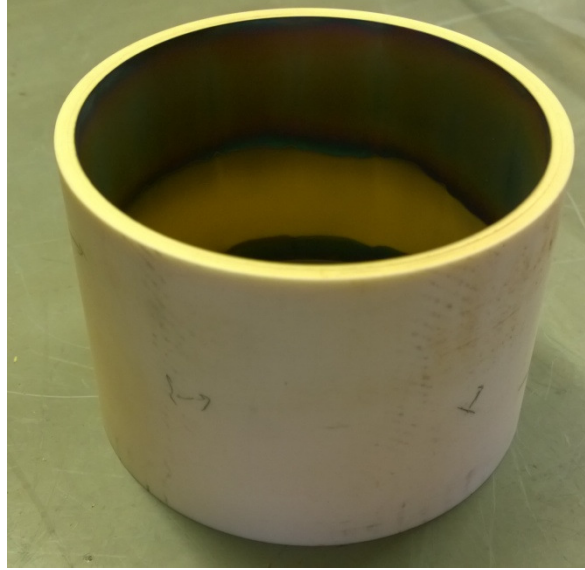
Figure 3.1 NIO1 Alumina cylinder.

Temperature difference of 4.4°C between the inner and outer surface of the ceramic cylinder has been evaluated from[7]

$$\dot{Q} = \frac{\Delta T}{R_{th}}$$

where $\dot{Q}$ is the thermal flux in W and R_{th} is the thermal resistance of the alumina cylinder calculated from[7]

$$R_{th} = \frac{Ln\left(\frac{R_{ext}}{R_{int}}\right)}{2\pi L \lambda} = 0.0065[\frac{K}{W}]$$

in which R_{int} and R_{ext} are the inner and outer radii respectively, 50mm and 55mm, L is the length and λ is the thermal conductivity that for alumina is 30W/m·K.[8]

Therefore it can be concluded that, if the air flow is sufficient to enough cool the external side of the cylinder and it is installed correctly, no problems due to high temperatures caused by the plasma heating should arise since the thermal gradient is very low.

After the leak another solution was adopted for the following campaigns: instead of the alumina cylinder a Pyrex cylinder was used since it is less expensive and the breakage probably was due to an imperfect installation. Therefore even if Pyrex has a thermal conductivity about 30 times less than Alumina (1 W/mK)[8] no problems due to the higher temperature on the inner face are expected; in fact the thermal gradient has been calculated as 130 °C (30 times larger than alumina case) and by assuming an outer temperature of about the ambient temperature since the cylinder is cooled by a huge air flow the inner temperature will not be over the maximum temperature allowed (500°C).

At first the Pyrex insulator was tested with a leak detector, then the source was cleaned with acetone since an evident deposit was present, probably due to the copper surface sputtering. In Figure 3.2 the Pyrex test and the deposit on the source components are shown.

Figure 3.2 Leak test on Pyrex cylinder (left) and metal deposit on the cover of the rear multi-pole (right).

Since the metal deposit inside the source can modify the electromagnetic field, for example by modifying the electric field at the plasma edge, and pollute the plasma, a molybdenum covering was added on the source walls since; molybdenum is the most suitable material due to its very low sputtering yield [3].Then the source was carefully assembled, with fine mechanical adjustment especially of the spring washers that keep the source assembly compressed so as to have perfect fitting of the components with compression forces as balanced as possible.
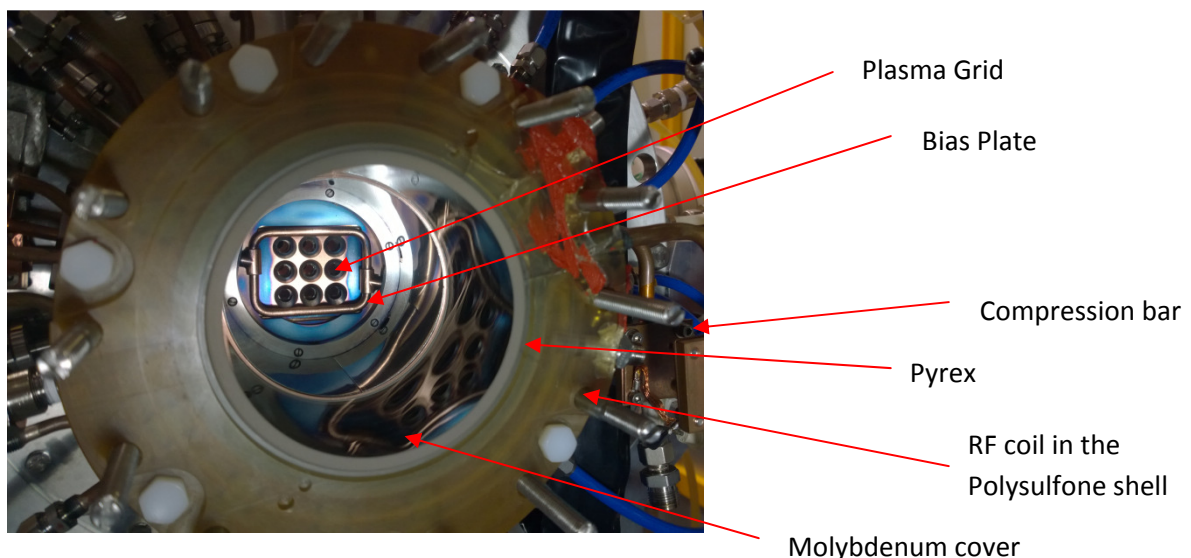

Plasma Grid

Bias Plate

Compression bar

Pyrex

RF coil in the Polysulfone shell

Molybdenum cover

Figure 3.3 New source assembly.

After closing the source, the NIO1 chamber was pumped in order to reach a vessel pressure of the order of 10^{-7} mbar, which is a suitable value in order to have negligible impurities in the chamber, for example due to wall degassing, with respect to the injected filling gas during

plasma operations; then cooling and electrical connections described in next paragraph were restored and other upgrades were installed.

3.2 Fast Interlock

In neutral beam accelerators, and thus also in NIO1, electrical breakdowns are expected during operations. These discharges might deposit a lot of energy on the grids of the acceleration column and might damage them and also the diagnostic equipment.

In order to be sure to preserve the power supplies from damages due to the high arc current a system called Fast Protection Unit (FPU) was developed, installed and tested on NIO1.It should be said that each HV power supply has its internal protection system that in case of arc switches off the HV output and generates a fault bit (ARC), nevertheless the manufacturer does not guarantee a total protection against arcs. Moreover whenever just one power supply is subjected to an arc, the other one has to be switched off as fast as possible in order to prevent another arc for example due to the first one [See Chap6]

Therefore FPU is required to switch off both high voltage power supplies as fast as possible in case an arc occurs.

Another feature of this system is to monitor the plasma light coming from the source and in case the light goes off, the FPU switches off the High Voltage Power Supplies (AGPS and EGPS) and RFPS since the reflected power would be higher and could damage the RF power supply itself.

The board is equipped with current sensors (Rogowski coils) that detect the arc by sensing the current along the AGPS and EGPS circuits; the plasma light detector is not implemented yet. Summarizing the logical operations of the board are the following:

- If an arc is detected on the AGPS or/and EGPS (by the Rogowski coils or by the power supply itself) the FPU drives to zero the output of both HV power supplies
- if the plasma light commutes from on to off HV power supplies outputs are set to zero

Logical operations are processed by a Field Programmable Gate Array (FPGA) ALTERA® EP2C5 which is a very fast integrated circuit, it is very flexible and it has a lot of input/output ports for possible future upgrades; in Figure 3.4 a scheme is reported with the connections on NIO1.
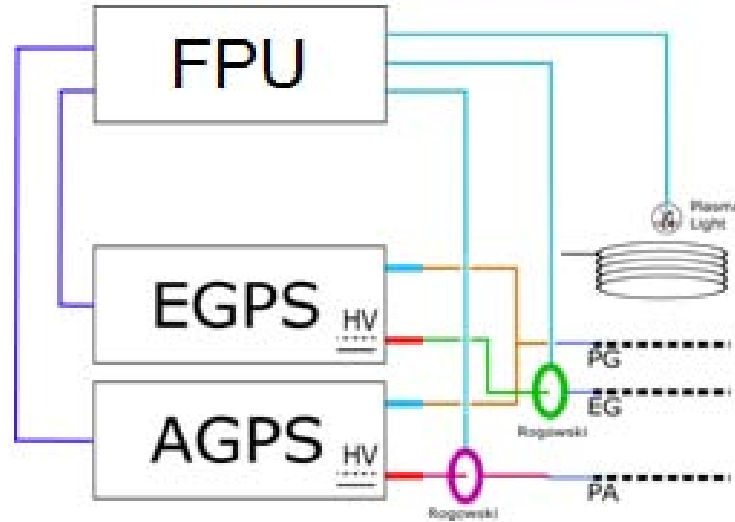
Figure 3.4 Fast Protection Unit connections.

As regards the analog input signals coming from the two Rogowski coils, each one is processed by a dedicated circuit involving a comparator. In this stage the voltage coming from the coil is compared with a tunable threshold in order to adjust the sensitivity of the circuit, finding the right compromise between detection capability and spurious triggers (for example due to electromagnetic interference).Then the digital comparator output is sent to the FPGA. The communication between FPU and AGPS is provided by an optical fiber since the board is placed on the HVD and the power supply is referred to the ground potential.

3.2.1 Rogowski coils

In this section the main characteristics of the current sensors for the FPU are described; after construction they were tested in order to have a whole characterization of the Rogowski coils, with the aim to check whether the response is suitable for the detection of the arc current in NIO1, and to validate the analytical model of the coil.
The Rogowski coil working principle is based on the Faraday-Neumann law: a winding, the Rogowski coil, linking a variable magnetic flux produced by a variable current **i**, experiences an electromotive force **E** as reported in Eq. 3.1 where **M** is the mutual inductance between the Rogowksi coil and the current carrying conductor.

$$E = -M \frac{di(t)}{dt} \qquad (3.1)$$

Generally the Rogowski core is made of non-magnetic material, in this way saturation phenomena are absent. The Rogowski coil output voltage depends on the variation of the

linked current, the frequency response of the coil and the load. The behavior of the coil is due to the combined effect of: the resistance R_{rog} of the wire, the parasitic capacitance C_{rog} between winding turns and the self-inductance L_{rog}. A further contribution, modeled by a capacitance C_s, is due to the presence of the screen that covers the entire winding and acts in order to reduce the noise due to electric coupling with the external circuit.

As the Rogowski coil provides an output voltage signal proportional to the linked current derivative, it is usual to process it with an integrator stage providing a voltage signal proportional to the linked current. In the present case a passive integrator was used, composed by a parallel between a resistor R_L and a capacitor C_L.

The equivalent circuit (lumped model) of Rogowski coil and integrator is shown in Figure 3.5 (right) where C_C represents the stray capacitance of the coaxial cable that connects the Rogowski coil with the integrator circuit.
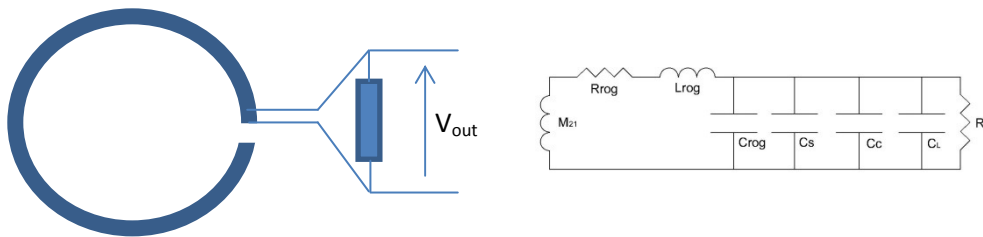

Figure 3.5 Rogowski coil picture with winding and return conductor (Left). Equivalent low frequency circuit (lumped parameter model) of the Rogowski (Right).

The Rogowski coil design was developed according to preliminary simulations of breakdowns that showed a rate of change of the arc current in the order of 100 A/µs .The current has to be detected on a 16mm diameter cable and in order to provide a high ratio of signal to noise, the coil output voltage has to be in the range of 20V during the fast current variation.

For reasons of simplicity a rectangular cross section was chosen for the coils and DELRIN was chosen as the core material. Figure 3.6 reports a view of the Rogowski coil with main geometrical dimensions.
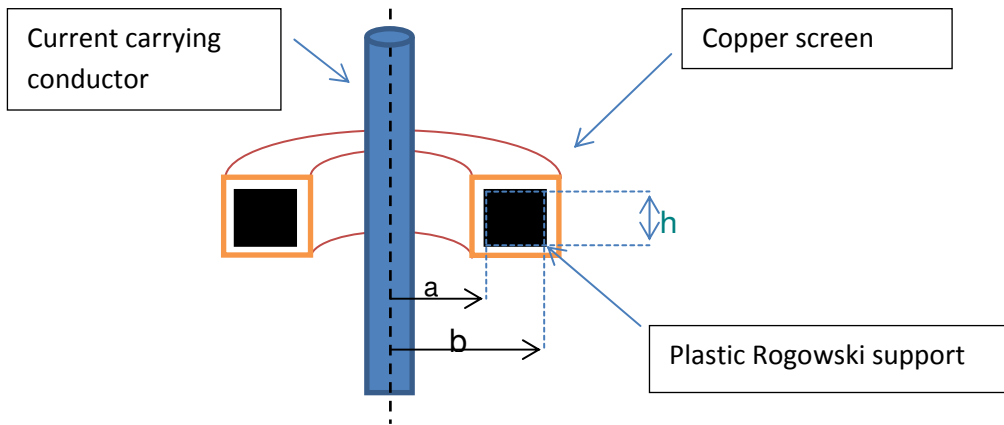
Figure 3.10 section of the Rogowski coil.

The dimensions of the core were assumed (see Table 3.1) and the number of turns N was evaluated from Eq.3.2 and M was calculated from Eq.3.1.

$$M = \frac{\mu_0 N h}{2\pi} ln\frac{b}{a} \quad (3.2)$$

Item	Value
Minor radius a	25mm
Majour radius b	35mm
Core edge length h	10mm
Square section h^2	10x10mm2
Number of turns	230
Support Material	Delrin

Table 3.1 technical specifications of the Rogowski

Since the Rogowski coils will carry just small and impulsive currents, no thermal constraints are present as regard the minimum section of the wire, thus the diameter of the wire was evaluated as ratio of the internal circumference of the core and the number of turns in order to cover the whole ring, therefore a 0.7mm enameled copper wire was chosen.

In order for the return wire loop to be exactly at the middle of the turns, a V-shaped groove was drilled on the outer circumference of the DELRIN core, so the effect of external electromagnetic field can be neutralized as well as possible; furthermore the Rogowski coils were covered with a self-amalgamating tape to provide voltage isolation and a copper shield

was wrapped around the sensors and connected to the grounded pole of the Rogowski coil output to provide a shield against electrostatic transients (dV/dt).

In Figure 3.7 the pictures of the developed Rogowski coil during the main construction phases are shown.

The design, as described in the following sections, has considered also the identification of suitable parallel resistive-capacitive load (passive integrator) to the Rogowski to provide better frequency performances of the current detection.
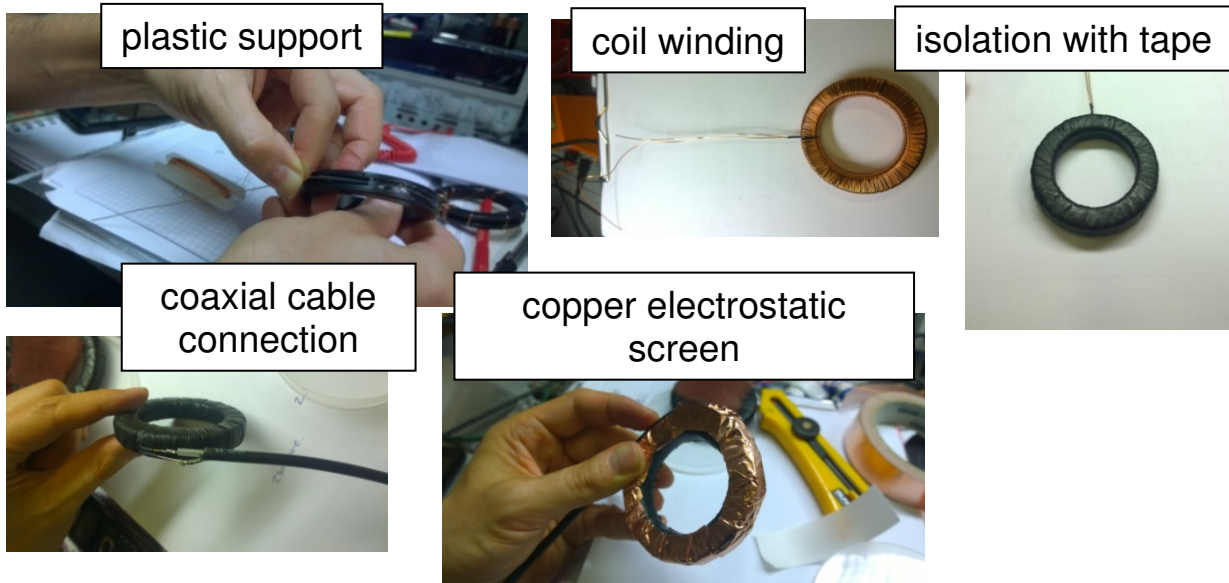

Figure 3.7 Rogowski coil construction phases. From the upper left: plastic support with central groove to host the return copper thread; wrapped copper thread completed phase, coil after electric isolation with plastic tape; detail of coaxial cable connected to the Rogowski coil; coil after electrostatic screen wrapping.

The resistance R_{rog} of the winding was calculated by the length of the wire *l* = 9.2m evaluated by the number of turns N = 230 and their perimeter l_s(4cm),and the kilometric resistance **r** of the D = 0.7mm diameter copper wire, 43.75 Ω/km.

$$R_{rog} = r \cdot l$$

Self-inductance L_{rog} has been calculated by the formula:

$$L_{rog} = \frac{\mu_0 N^2 h}{2\pi} ln \frac{b}{a}$$

The winding capacitance C_{rog} is affected by different contributions: dielectric support, real geometry and real distance between the windings; it is analytically difficult to evaluate precisely C_{rog}. Furthermore the real contribution, in the order of few pF, is expected to be negligible with respect to the other capacitances, C_S and C_C.

The stray capacitance of the winding with respect to the grounded copper screen C_S was calculated by assuming a parallel-plates capacitor model in which the surface area A is calculated by the mean circumference of the coil $2\pi R_m$ (where R_m = (a+b)/2) multiplied by the perimeter of the square section of DELRIN and the distance between the plates is the thickness d=0.2mm of the self-amalgamating tape with relative permittivity ε_r=2.5.

$$C_s = \varepsilon_0 \varepsilon_r \frac{A}{d}$$

The capacitance C_C of the RG58 cable connected to the output of the winding was obtained by the self-kilometric capacitance (101pF/m) of the cable for 0.5m length.

In this simple model, skin effect, RG58 cable inductance and resistance were neglected. In Table 3.2 the electrical parameters of the Rogowski coil are reported.

	Calculated equivalent parameters
R_{rog} [Ω]	0.4025
L_{rog}[uH]	35.6μH
C [F]	830pF(C_s)+50 pF(C_c)

Table 3.2 equivalent electrical parameter of the Rogowski coils.

In order to verify the response of the output voltage with respect to the frequency of the input current, the transfer function was analyzed. Furthermore in the flat portion of the transfer function, the sensitivity of the Rogowski coils was evaluated; this parameter expresses the ratio of output voltage to input current.

The transfer function was measured by the Network Analyzer HP 4194A connected to the circuit shown in Figure 3 which is composed of a 2.73Ω shunt resistor R1 in series with the blue wire wound through the Rogowski coil 10 times; in this way the current linked to the coil is amplified 10 times for a better measurement; the current is proportional to the voltage on the shunt resistor connected to the 'Reference' Network Analyzer input.

The coil output is measured by the 'Test' Network Analyzer input with and without the RC load.

With this setup the transfer function expresses the ratio between the output voltage and the shunt voltage with respect to the frequency variation and its value is expressed in decibels.

The results of the measurement are shown in Figure 3.9 for the cases with and without RC load. Without load the bandwidth above -3dB was found between 200 kHz and 3.8 MHz and the magnitude of the transfer function in the flat zone is -2dB. In order to increase the bandwidth and to have suitable value of the sensitivity, different types of RC loads were tested and the better results in terms of detector overall response was obtained with R_L=20 Ω

and C_L=330pF. Considering this load the bandwidth of the Rogowski detector was found between 65 kHz and 3.9 MHz and the magnitude is -12dB.

The sensitivity was calculated for the flat band by the following equation:

$$20Log\frac{Vtest}{Vreference} = T/R[dB]$$

then after measuring Vtest/Vreference, the result was multiplied by R1 in order to have the ratio with respect to the current of the shunt; furthermore the results have to be divided by 10 because of the 10 turns crossing the coil. Table 3.3 reports a summary of the bandwidth and sensitivity of the Rogowski detector with and without RC load.
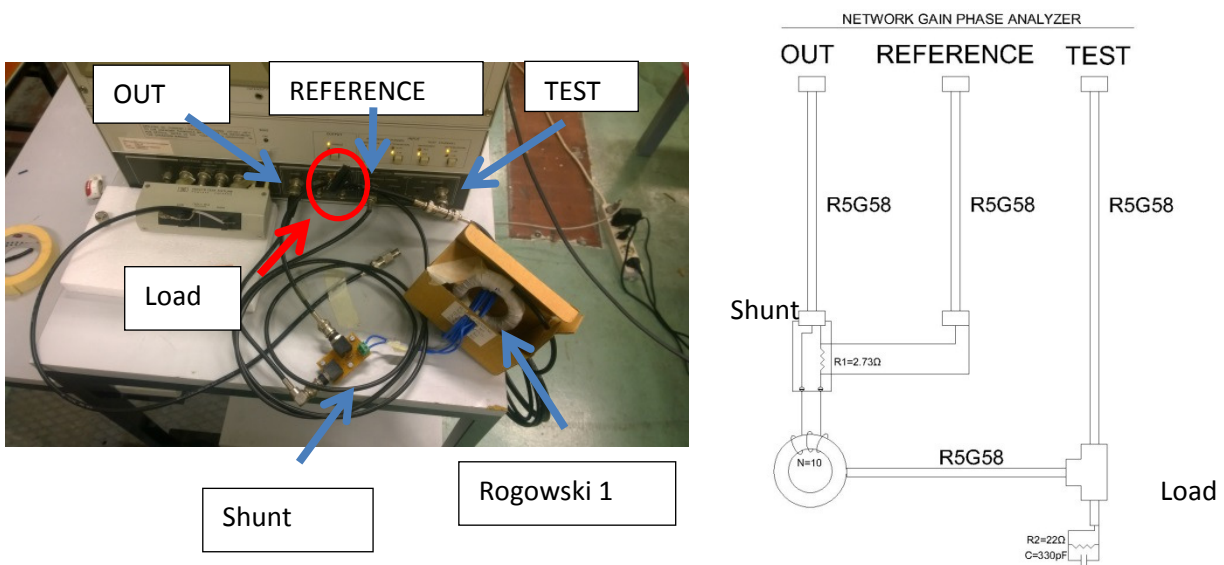
Figure 3.8 (left) transfer function measurement with network analyser, (right) measurement layout.
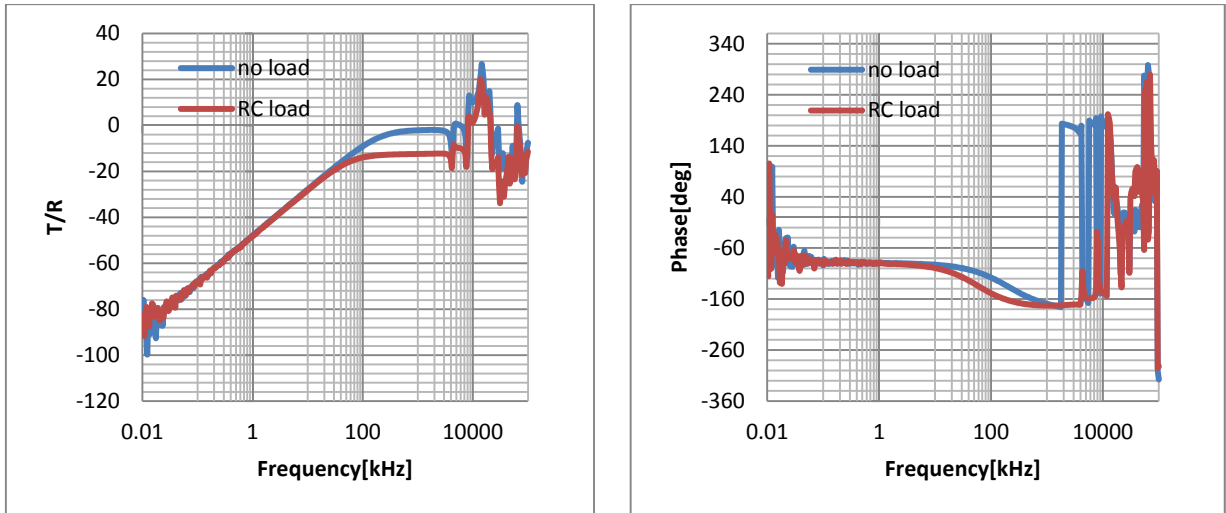
Figure 3.9 transfer function of Rogowski coil no. 1 with and without load.

	No load	RC load
Bandwidth	200kHz-3.8MHz	65kHz-3.9MHz
Sensitivity (V/A)	0.22	0.068

Table 3.3 summary of the bandwidth and sensitivity of the Rogowski detector with and without RC load.

Impedance measurement was provided by a Network Analyzer (HP 4194A) connected by an RG58 cable to the Rogowski coil as shown in Figure 3.10.

The aim of this measurement is to characterize the two current sensors provided by their own impedance amplitude and phase with respect to the frequency variation.
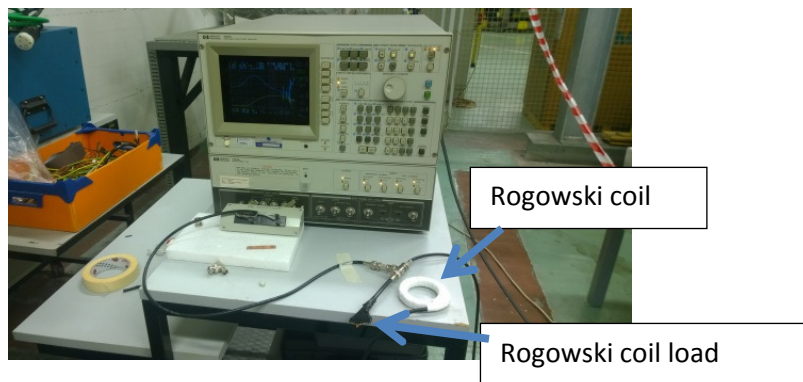
Figure 3.10 setup of Rogowski coil impedance measurement.

The first set of Rogowski coil measurement was made on both Rogowski coils, named rog1 and rog2, without any load connected to the output. The frequency response was measured in the range 100 Hz- 40 MHz and it shows a first resonance peak at about 1.3 MHz [Figure 3.11] mainly due to the effect of the coil self-inductance and the total capacitance which is associated with: the RG58 cable connected to the coil, the copper shielding and the winding.

In the picture the analytical results of the Rogowski coil output impedance(green line) is plotted based on the Rogowski coil parameters and model previously identified and reported in Table 3.2. The accordance with the measured values for amplitude and phase is good up to the first resonance at about 1.3 MHz; only a slight difference is present at lower frequency.
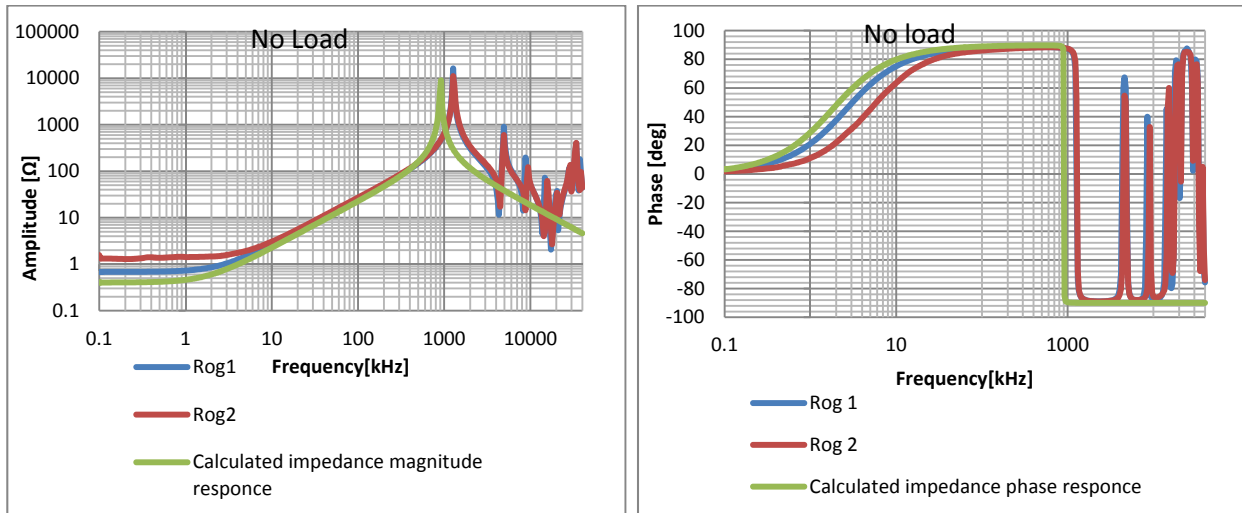

Figure 3.11 frequency response of Rogowski coils 1 and 2 without load. In green the calculated impedance and phase form the Rogowski electrical model previously evaluated.

The second set of measures, see Figure 3.12, shows the two coils loaded with the RC parallel load (C_L = 330 pF, R_L = 22Ω).

The Rogowski coil loaded with the R_LC_L circuit is seen by the network analyzer as the previous resonance parallel circuit, see Figure 3.11, but with a higher capacity value due to C_L contribution and with a parallel resistor R_L. At the resonance, the impedance peak has about the resistance value. This behavior is well shown by the analytical and measured frequency response reported Figure 3.12 (Amplitude) where the peak value was found 22 Ω, which is the R_L value. Regarding the phase chart in Figure 3.11(Phase), the response has the usual pattern as expected for a parallel resonance circuit. At the resonance frequency the phase is 0°, the lower frequencies are affected by the inductive part of the circuit and the phase tends to 90°. At higher frequency the phase curve exhibits a capacitive behavior but it is affected by other multiple resonances.

Furthermore the amplitude chart depicts a flat shape of the impedance amplitude from 200 kHz to 4 MHz. The wider maximum value of the impedance is due to the load resistor R_L, with respect of the case without loading the Rogowski.

For all previous cases the measured impedances, up to about 3MHz, is quite aligned to the analytical model (green curve) associated to the simple circuit of the second order shown in Figure 3.5 (right).
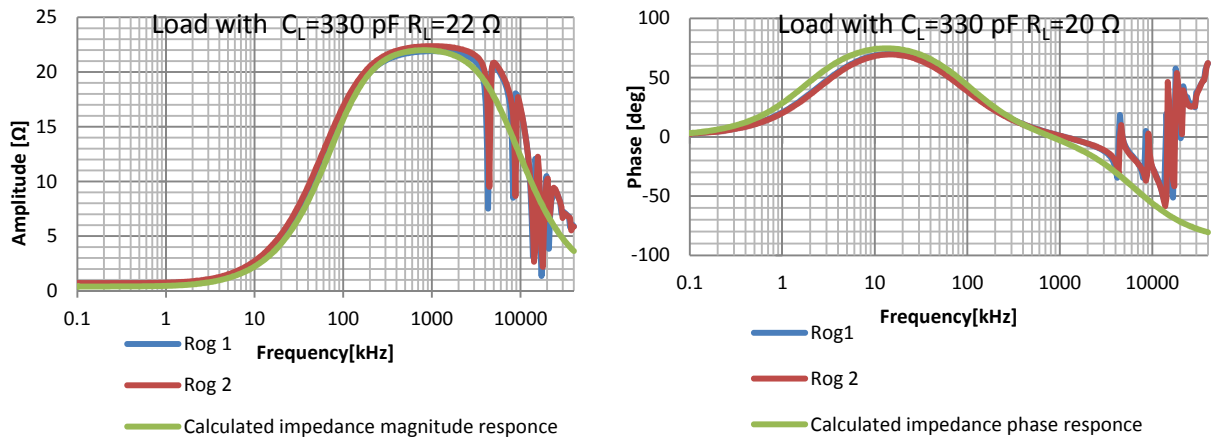
Figure 3.12 frequency response of Rogowski 1 and 2 with load: R= 22 Ω in parallel with C=330pF.

3.3 High voltage tests

Another upgrade on NIO1 consists in the installation of some passive protections needed for the protection of the EGPS, especially when an arc occurs between EG and PA. Even if the power supply has its self protection for short circuits at the output, the protection is not guaranteed because it has been designed for stand-alone configuration.

In the particular case of EG-PA breakdown the two high voltage power supplies are brought to work in parallel configuration, hence AGPS tries to force a current into EGPS.

Basic layout of the passive protection circuit and also the arc between the extraction and post acceleration grids are shown in Figure 3.13
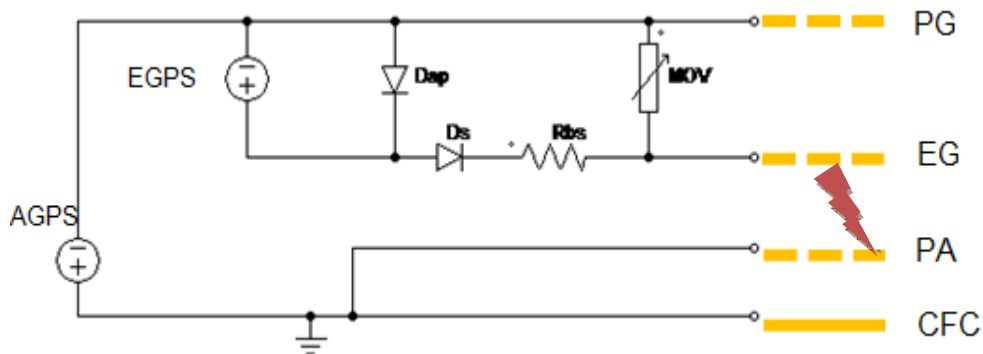

Figure 3.13 Passive protections basic layout.

The working principle of the protection circuit can be explained as follows: when the AGPS tries to force a current into EGPS, the path is blocked by the series diode (D_s). which is counter polarised, hence the current path is closed thorough a Metal Oxide Varistor (MOV) which

51

clamps the voltage between PG and EG at a controlled level of about 10kV that is a tolerable value for the power supply. Shown below, in Figure 3.14, is a typical current-voltage characteristic curve of a MOV that provides excellent transient suppression performance . When a large voltage is applied across the varistor the impedance changes by many orders of magnitude. The varistor changes from an open circuit, allowing voltage applied to the electrical circuit, to a highly conductive level, where the system goes to ground. This highly conductive level reduces the voltage to a safe operating level[4].

Another dangerous condition for EGPS is represented by the situation in which the potential on the Plasma Grid goes higher than the Extraction Grid, for example during a PG-EG breakdown, where the current would be forced to flow into the power supply; for this reason an anti parallel diode D_{ap} is used in order to divert the current from the EGPS through the diode itself; during the normal operation the diode D_{ap} is counter polarized by the EGPS voltage and thus it is like an open circuit, furthermore a series resistor R_{bs} (100Ω)is present to reduce the arc current in case of PG-EG breakdown.
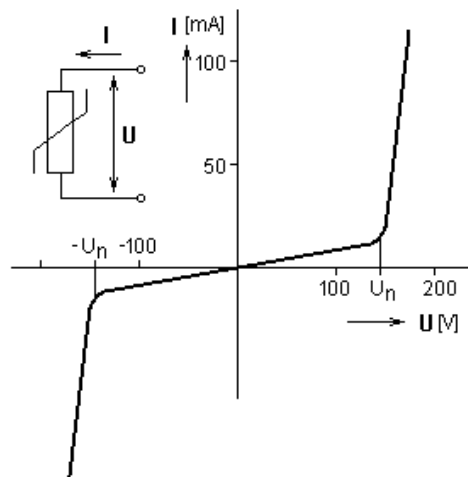

Figure 3.14 MOV typical characteristics.

For preliminary operations the circuit has been designed for a reduced operational regime for both power supplies, 5kV instead of the nominal rating of 10kV for EGPS and 20kV instead of 60kV,nominal rating for AGPS,where the design of a suitable HV protection circuit is less critical. The assembly is made of several components grouped in series and parallel according to the principle scheme shown in Figure 3.13 to fulfill the requirements in terms of voltages and currents expected in NIO1. The setup of the HV protection circuit then permits the operation of NIO1 in order also to acquire important information on real current and voltage waveforms triggered by the breakdown in the HV circuit; a second phase will follow where the knowledge acquired from the previous one will be applied to address properly the definition of the full load HV protection circuit for future campaigns.

The components of the circuit were tested and assembled on a board, and then installed on the HVD as shown in Figure 3.15, therefore a breakdown campaign was performed in order to test and characterize the circuit.
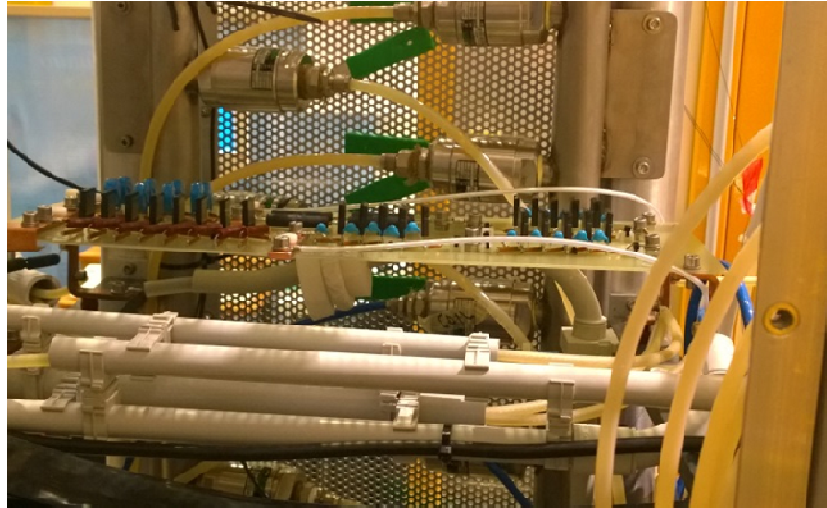
Figure 3.15 New passive protection circuit installed on NIO1.

The tests reported in the following are performed on NIO1 site and comprise the study of two configurations of the NIO1 circuit, to test separately two breakdown conditions: the PG-EG breakdown and the EG-PA breakdown. Each of these breakdown occurrences are likely to happen during normal operation of NIO1 as shown in Chapter 6 in which the following plasma campaigns are described. Along with gathering information on the protection circuit behavior the tests permit to identify clearly for the first time the actual electrical waveforms triggered by the breakdown in the NIO1 HV circuit. This information is fundamental to allow the design of future full voltage rating protection circuit of NIO1 HV circuit as already mentioned above.

The short-circuit device is a spark gap with the electrodes in a closed gas-tight plastic chamber. The chamber can be pressurised with air and the air can be evacuated by operating a pneumatic system see Figure 3.16. For the operation it is necessary to find the proper spark gap working condition in terms of gas pressure and electrode distance since increasing either one or the other parameter can increase the breakdown voltage of the device; then the ignition of the spark is triggered by the release of the air inside the spark gap.
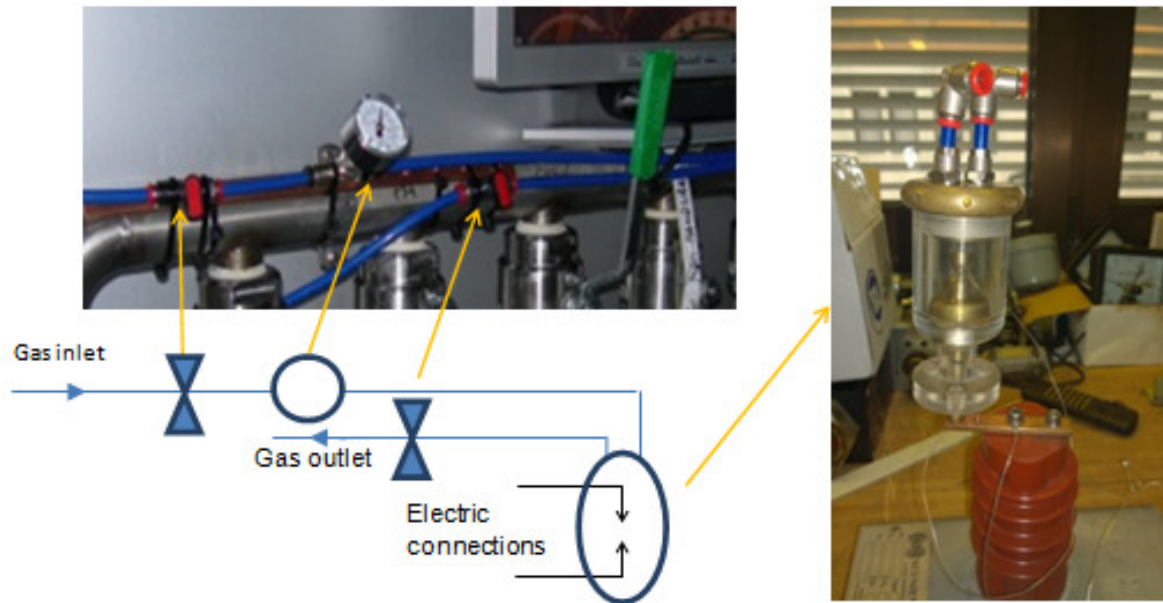
Figure 3.16 Arc triggering circuit (left) and Spark Gap device (right).

3.3.1 PG-EG breakdown

The configuration of NIO1 circuit for the test is reported in Figure 3.17: the HVD was set at ground potential, the AGPS was disconnected and the AGPS Rogowski coil was used to measure the current flowing from the main collector (at HVD potential) to ground. A spark gap was inserted in the PG-EG gap to induce the breakdown.

EGPS current waveforms are read from a current probe, marked "A" in the figure, and by both Rogowski coils, marked with "R" in the figure. They are all recorded by an oscilloscope referenced to the HVD potential.
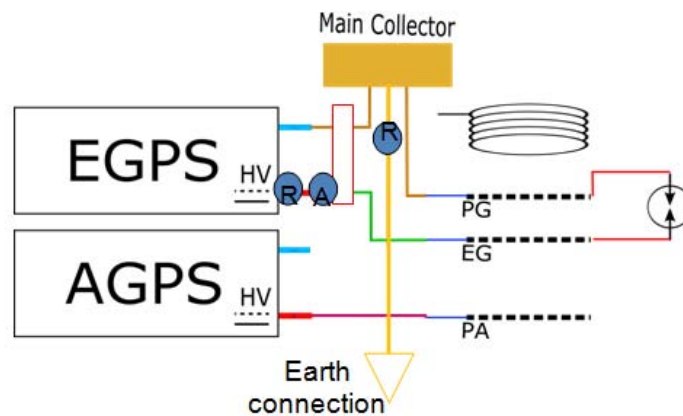

Figure 3.17 Circuit layout used to induce and characterize the PG-EG arc.

A set of measurements were performed to characterize the system up to 5kV EGPS voltage. In Figure 3.18 and Figure 3.19 the current read from the current probe and Rogowski coils are reported for the full test voltage of 5kV. The EGPS current read, about 35A, was found well within the specifications of the D_s diode which can carry a breakdown current up to 70A[5]; this demonstrates the proper design also in transient conditions.

Figure 3.20 reports the peak breakdown current acquired during the campaign. In particular a linear relation is clear between EGPS voltage and peak current.
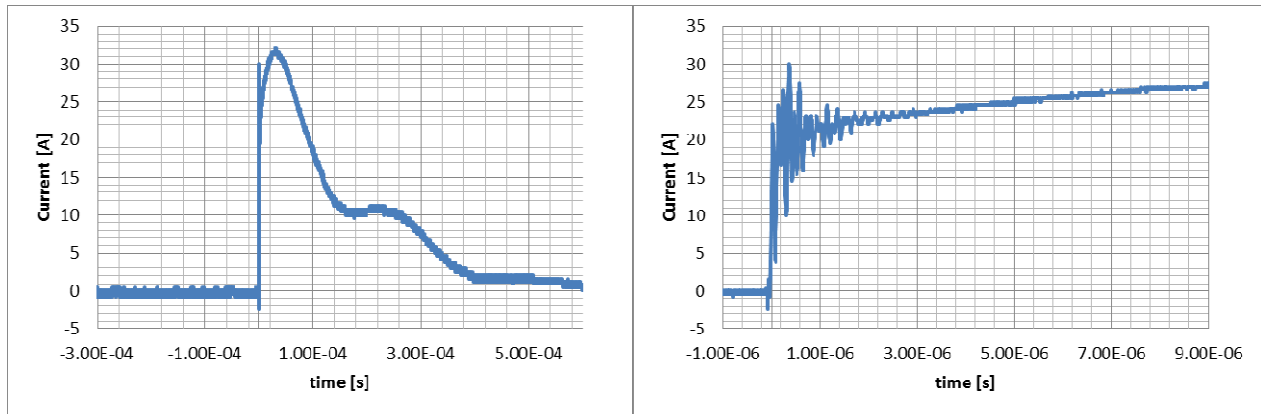

Figure 3.18 EGPS breakdown current read by the current probe in a 5kV test voltage. In the right picture a zoomed views of the left plot is visible.
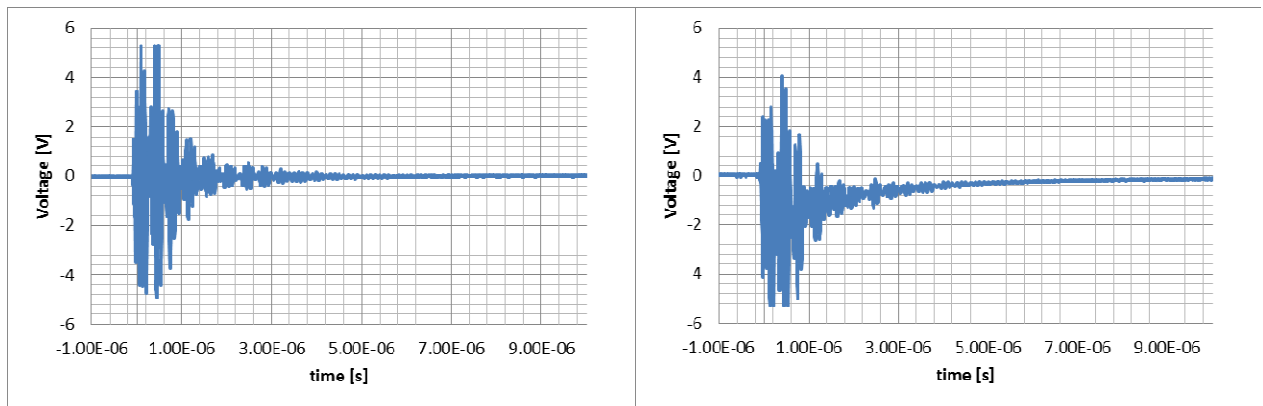

Figure 3.19 5kV EGPS test voltage. On the left theAGPS Rogowski voltage is displayed; on the right the EGPS Rogowski voltage is displayed.

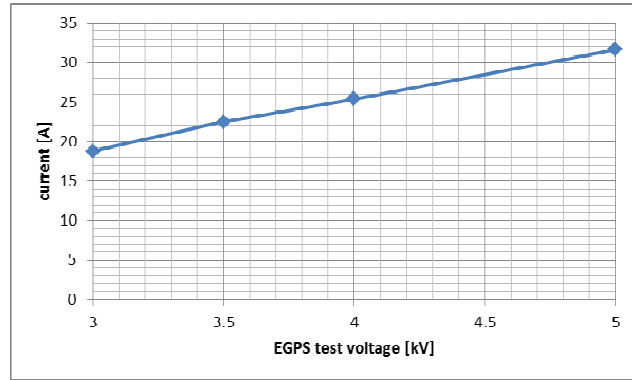| EGPS test voltage [kV]	EGPS current peak [A]
3	18.8
3.5	22.5
4	25.4
5	31.65

Figure 3.20 Peak values for EGPS arc current at different voltages.

3.3.2 EG-PA breakdown

In this section the effect of the EG-PA arc is presented. The configuration of the HV circuit for this test is reported in Figure 3.21. The current on the EGPS and the AGPS output was measured; see the mark "A" in the figure. Also the HVD voltage with respect to ground was measured, see the mark "V" in the figure. As visible in Figure 3.21, the voltage probe was measuring with respect to the HVD potential.

Furthermore, because of the EG-PA arc, the HVD voltage reading gives a measure of about the PG-EG voltage gap (upon assuming that the arc resistance is negligible) and finally the Vp varistors branch voltage.
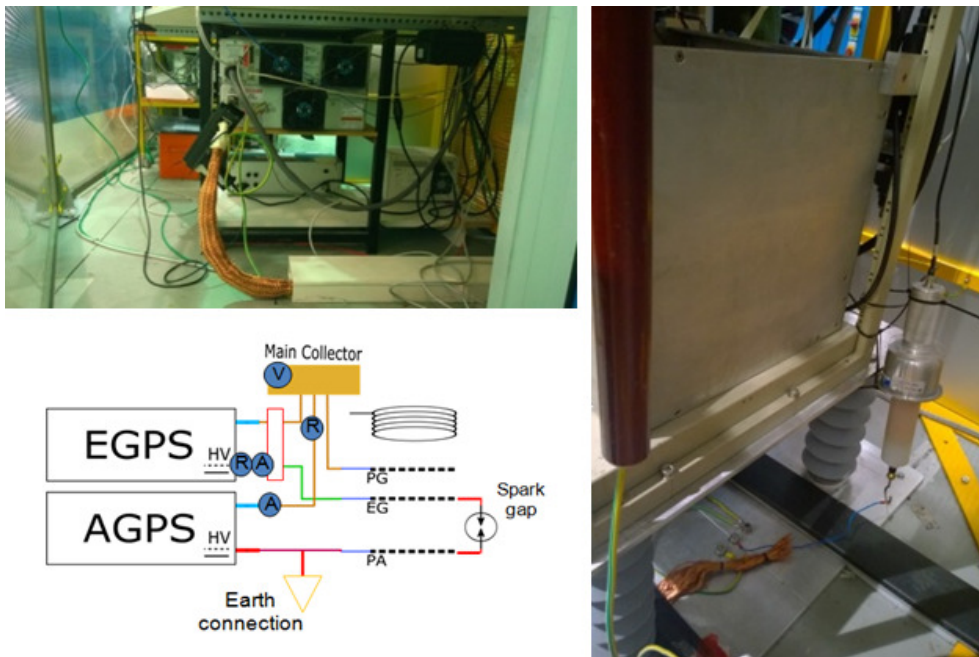

Figure 3.21 Layout for the EG-PA induced breakdowns.

Both EGPS and AGPS were operated simultaneously for the first time and breakdowns are induced up to the condition with EGPS=5kV and AGPS =20kV. In Table 3.4 the main results of the tests are reported. The HVD voltage and EGPS current was recorded. The first measure, as already mentioned, reports actually on the PG-EG gap, the second measure was set up in order to provide a clear evidence, in case a significant current were detected, that the series diode might not work properly, since an inversion in the current has been recorded [Figure 3.22] and finally the EGPS protection circuit could be faulty. The occurrence of such a current affects the EGPS operation because it tends to charge the output stage of this PS.

Shot number	AGPS test voltage [kV]	EGPS test voltage [kV]	HVD voltage clamp (2us after breakdown) [kV]	AGPS peak current [A]	EGPS peak current [A]
25	10	5	8.6kV	10.7	5
27	12	5	8.7kV	13.25 slightly saturated	7.5
29	15	5	8.7kV	26.45 slightly saturated	9.58
33	18	5	8.6kV	41.25	16.24
40	20	5	8.7kV	51.65	23.6

Table 3.4 Main results of induced breakdowns at different AGPS voltages.

The EGPS current waveform measured in the campaign, see Fig.3.22, exhibits similar behaviour in all conditions explored with a noisy phase at the breakdown event. The high peak current measured has a magnitude of some tens of amperes in the worst case. The current measured does not show the overall evolution as seen in the previous dedicated EGPS breakdown but just a fast and short (few hundred of nsec) noisy waveform. It is not clear at the moment if these are real currents or induced effect.

A clear behaviour experienced during the campaign is the complete absence of HVD voltage polarity inversion. In all test conditions the behaviour observed is similar to the right-hand side of Figure 3.22: the HVD voltage experiences a rapid variation from the AGPS test voltage and within a fraction of microsecond it reaches the clamped voltage due to the operation of the varistor V_p. In all tests the value of the camped voltage was found 8.7kV, a value compatible with V_p characteristics. Furthermore, the AGPS maximum peak current observed

in the AGPS 20kV test voltage was found 52 A, a value well tolerated by the V_p design which allows up to 200A of impulsive current [5]. In Figure 3.23 the signals detected by the Rogowski coils in the AGPS and EGPS circuits are shown. The waveforms are quite similar even if the current experienced by the two power supplies are different. This is an aspect that deserves further investigations because it may indicate, as already mentioned, possible cross-talk between the measuring cables. The FPU detected all breakdowns, with actually some false detection events due to the high noise detected by the EGPS Rogowski coil, and it has properly commanded the HVPSs to the switch off state as required.
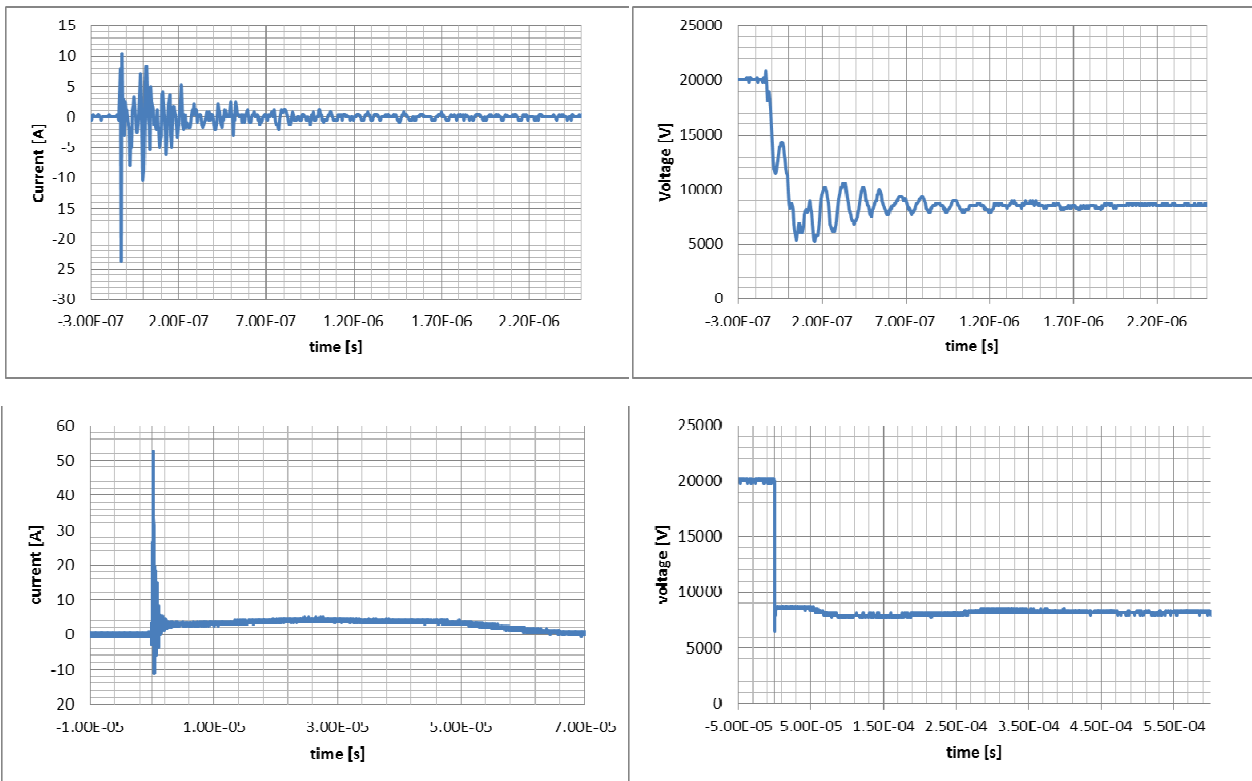

Figure 3.22 pulse with 20kV AGPS voltage and 5kV EGPS voltage. (Upper line left) EGPS output current; (Upper line right) HVD voltage respect to ground. (Lower line left) AGPS output current. (Lower line right) HVD voltage respect to ground (time zoom), pulse with 20kV AGPS voltage and 5kV EGPS voltage (10Ms/sec).
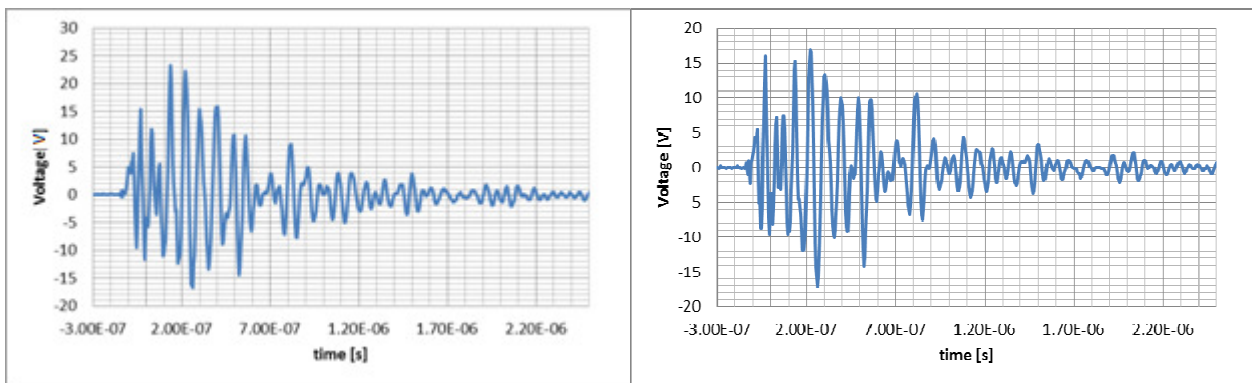

Figure 3.23 AGPS voltage 20kV and EGPS voltage 5kV. Rogowski coil voltage:(left) AGPS circuit; (right) EGPS circuit

58

3.4 Electrostatic field measurement

During first NIO1 operations after vacuum leak, a measurement of the electrostatic field around the NIO1 box was done in order to evaluate the magnitude of the E field in different points and to assess the exposition of the operators during NIO1 operations and to verify the adequacy of the electrostatic shielding.

In this test the layout of the electric circuit was reconfigured by disconnecting the EGPS from the HVD and by short-circuiting the EG with the zero collector and hence with the PG; furthermore the gas line was filled with pressurized hydrogen (1bar) in order to prevent discharges according to the Paschen law since the hydrogen feeding tube can act like a discharge tube; the Ethernet cable of the Pirani vacuum detector was disconnected as usual when the HVD is polarized since it is connected between the source and ground.

The test was made by a mono-axial electric field mill and its principle is briefly recalled below.[6]

The instrument is basically composed by a metallic rotating blade called shutter connected to a small motor; the shutter is usually grounded thorough the shaft of the motor itself; then aligned with the shutter there is a metallic insulated fixed vane connected to an amplifier.[Figure 3.24]
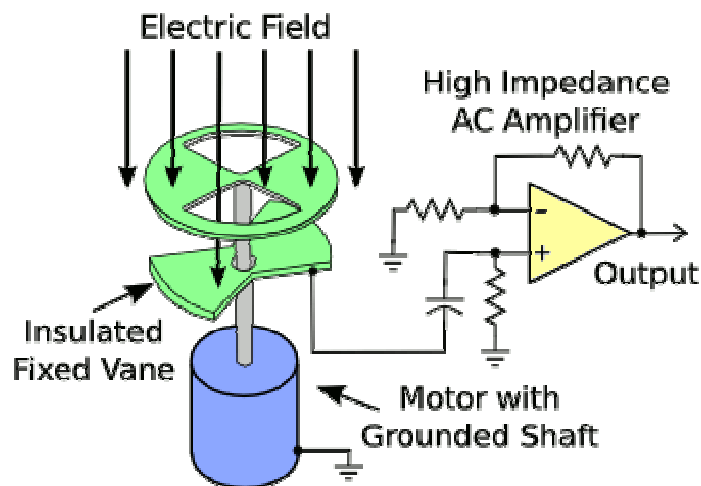

Figure 3.24 Electric field mill principle scheme.

The working principle is based on the first Maxwell equation (Gauss law) that in the integral form is reported in Eq.3.3

$$\oiint_{\partial\Omega} \mathbf{D} \cdot d\mathbf{S} = \iiint_{\Omega} \rho \cdot dV \qquad (3.3)$$

In this application Ω is the volume of the vane and since it is made of a homogenous material, in steady state conditions and by considering just the normal component for the E field, the equation can be easily integrated and rewritten as follows:

$$\varepsilon E A = Q \qquad (3.4)$$

where ε is the vane permittivity, E is the normal electric field, A is the total area of the vane and Q is total electric charge induced from E and accumulated on the vane.

During the operation the shutter periodically covers the vane, and as it is grounded, it acts as an electrostatic shield; in this way the charge stored on the vane is proportional to the portion of A that is uncovered.

For each revolution the vane is covered and uncovered two times by the shutter, and thus if the angular speed ω' and E are constant the uncovered area A(t) and hence the charge q(t) have a linear variation with time as shown in Figure 3.25.
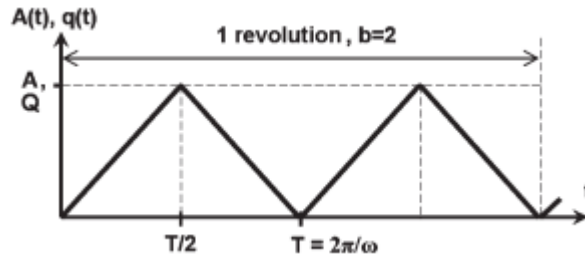

Figure 3.25 stored variation on the Field Mill due to constant rotation

Since the charge variation in time is a current, Eq.3.4 can be rewritten as shown in the following equation (Eq.3.5)

$$i(t) = \frac{dq(t)}{dt} = \varepsilon E \frac{dA(t)}{dt} \qquad (3.5)$$

The period T shown in Figure 3.25 is defined as the time to expose and cover the sensor once. Given a rotation speed ω and the number of the blades of the shutter b, the signal frequency ω can be expressed as:

$$\omega = b \cdot \omega'$$

Rewriting A(t), in the time interval 0 ≤ t < T/2, with the previous equation finally yields:

$$I = \frac{\omega}{\pi} \varepsilon A E$$

This means that the electrostatic field can be evaluated from the current generated by the field mill since the angular speed ω' is known.

On NIO1 measurements have been done in different positions and with different heights and orientations for the instrument by searching the maximum value of the electric field for each measurement point.

The field mill was placed on a dielectric easel and then connected with the ground as shown in Figure 3.26.
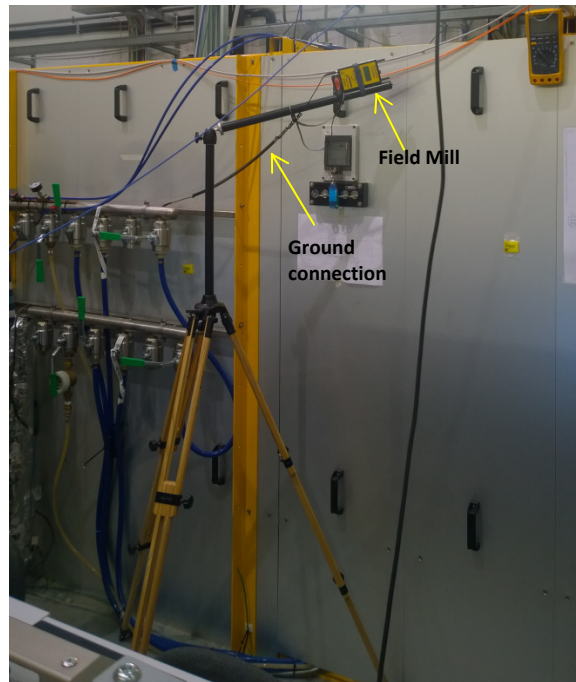

Figure 3.26 Electrostatic field measurements.

First set of measurement has been done in pos 7 (see Figure 3.27), between the console and the NIO1 box, the instrument height was 1.90 m and it was oriented to the HVD with the purpose to find the maximum value for the field; then the HVD voltage was increased from 0V up to 60kV with 5kV steps and the results of the measurement is shown in Table 3.5.

Then the voltage was lowered to 0V and raised again up to 60kV in order to verify if a hysteretic phenomenon was involved; the measurement result showed about the same values for all three sets, hence no hysteresis was found.

VAGPS [kV]	E [kV/m]
0	-3
5	-4.5
15	-5
20	-5.8
25	-6
30	-7.2
35	-7.8
40	-8.6
45	-9.3
50	-10
55	-10.7
60	-11.4

Table 3.5 Electrostatic field in position 7.

A second measurement set was performed in position 2, where spectroscopists are usually seated.

The E-meter was oriented to the insulating transformer at the height of 1.1 m and the field was measured just at 50 and 60 kV, furthermore in the same position the field mill was raised at 1.90 m and oriented vertically in order to check if some field lines coming from the HVD can go over the electrostatic shield installed over the lead panel; with this configuration the magnitude of the field was reported in the third column of Table 3.6.

VAGPS[kV]	E[kV/m]	E[kV/m]
50	-2.8	-11
60	-3.2	/

Table3.6 Electrostatic field in position2.

A third measurement set was made in position 4 at 1.5m (just above the enclosure) both in the vertical and the horizontal position.

It resulted that even with 0V on the HVD a high value for the field was present as shown in Table 3.7.

	Vertical	Horizontal
VAGPS [kV]	E[kV/m]	E[kV/m]
0	-2.8	-9
50	-7.6	-14

Table 3.7 Electrostatic field in position 4.

These results showed that electrostatic charges stored inside dielectric materials (for example the enclosure) can strongly affect the measurement by an offset comparable with the magnitude of the field coming from NIO1.

The last measurement sets have been made respectively in positions 8 and 9 at 50kV with the gauge at 1.5m height, with vertical orientation; results are shown in Table 3.8

VAGPS [kV]	E[kV/m]	E[kV/m]
0	-4.4	-3.5
50	-5.6	-5.5

Table 3.8 Electrostatic field in position 8 (first column) and 9(second column).
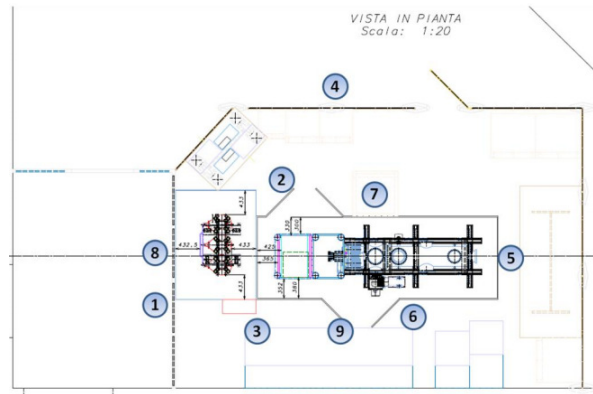

Figure 3.27 NIO1 topographic plant.

All previous measurement have to be considered for information only, since the European Directive does not consider electrostatic fields dangerous for health[ICNIRP]; however a Russian regulation exists (GOST 12.1.045-84) in which maximum limits are defined:60kV/m for 1h per day; for a magnitude between 20kV/m and 60kV/m the maximum exposition time has to be calculated by t[h]=(60/E)^2;values below 20kV/m do not involve specifications on the maximum exposure.

It can be concluded that the measurement are strongly dependent on the electrostatic charges present in the environment; nevertheless the field measured in pos 7 is expected to be coming from the NIO1 rack; furthermore in this zone operators are usually present for several hours; even if there are no health risks for the operators, one solution to decrease the field could be to extend the electrostatic shield over the rack.[Figure 3.28].
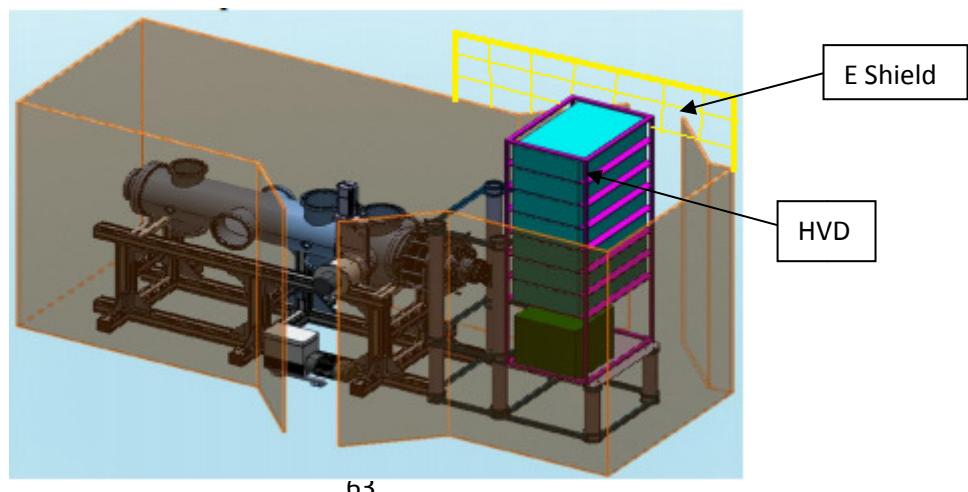

Figure 3.28 NIO1 electrostatic shield box.

3.5 PGF improvement

Up to the beginning of the thesis period the so called Plasma Grid Filter (PGF) had been used with a maximum current of 200A although its power supply (PGFPS) has a capability of 400A.

The main problem is represented by the heating of the circuit components, in particular a high current copper braid and MACOR feed-throughs might achieve high temperature and consequently be damaged.

As regards the braid the problem affects the isolation which can be subjected to premature aging or even melt; on the other hand, the feed-through might crack if excessively heated.
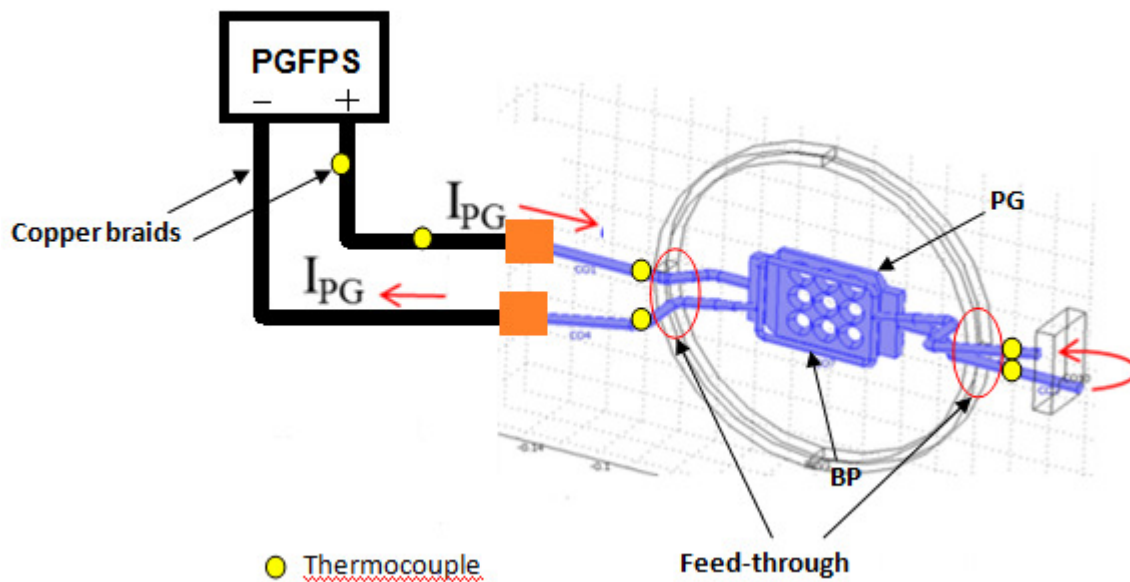
A scheme of the filter circuit is shown in Figure 3.29.

Figure 3.29 Plasma Grid Filter.

For the above reasons a thermal test was performed by deploying 6 thermocouples as follows: 4 of them were connected as close as possible to each feed-through in order to measure the temperature as much as possible like the one inside the pipe; another thermocouple was embedded between the braid and its insulating sheath; the last one was installed later in another point between the two braids near the power supply. Since the thermocouples provide just a local measurement, another system of measurement was installed for the purpose to have an integral measurement of the temperature, especially to evaluate the average temperature of Plasma Grid and Bias Plate since they are in vacuum and it is not possible to have a local measurement with thermocouples without opening the vessel. Therefore three volt-amperometric insertions were performed: the voltage drop along Plasma Grid, Bias Plate and the whole braid were measured, hence three voltmeters were connected; the current was measured by the power supply internal circuit.

All three elements are made of copper, hence the temperature T was evaluated by eq.3.6 linking the resistance with the temperature.

$$R(t) = R_0[1 + \alpha(T - T_o)]$$ (3.6)

Where R_0 is the resistance at the starting temperature T_0 and α is the temperature coefficient of the material, for copper 0.0039 [°C^{-1}].[10]

For the bias plate and plasma grid it a starting temperature of 24°C was assumed and 27°C for the copper braid: these were the thermocouple measurements at the beginning, when the system is thermalized. The test was carried out starting from 100A and then continuously checking the temperature in order to prevent excessive overheating.

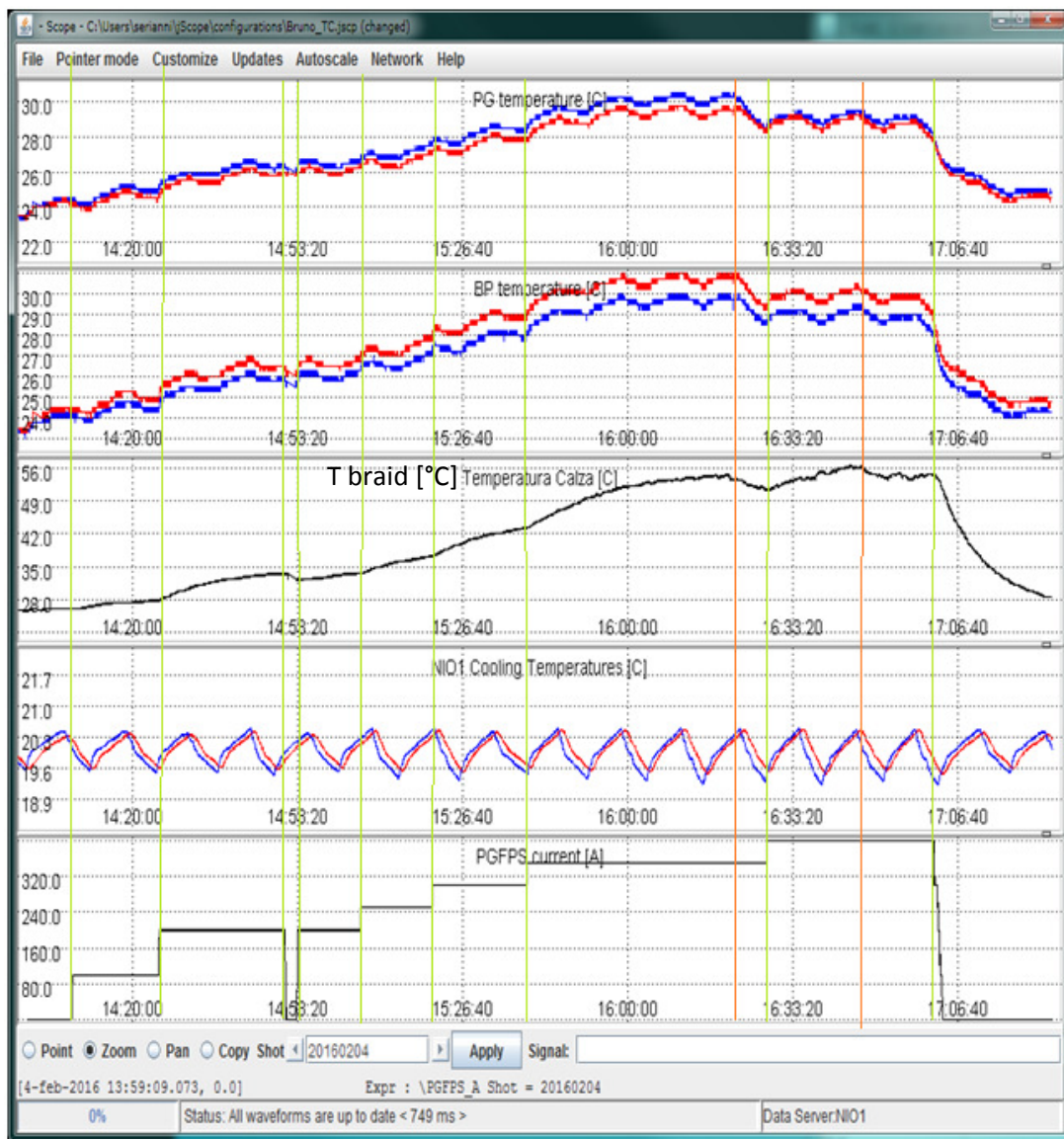The test showed the following results [Figure 3.30] and [Figure 3.31]

Figure 3.30 PGF test status monitor.

In previous graphs the redlines represent temperatures at the outlet of the respective circuits. It can be observed that Plasma Grid and Bias Plate exhibit a wavy behavior since they are water cooled and the water temperature is subjected to cyclical variations as shown in the 4th panel.

During the test quite different values were obtained between the temperature of the copper braid given by the thermocouple and the volt-amperometric estimate [Figure 3.31]; therefore just before the first orange line in figure an inspection of the braid was made since the temperature measured by the thermocouple was about 55 °C but the volt-amperometric indicated over 70°C.
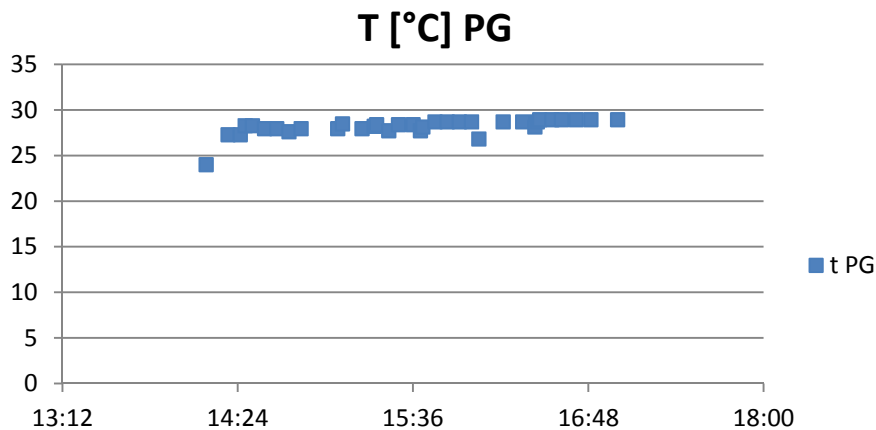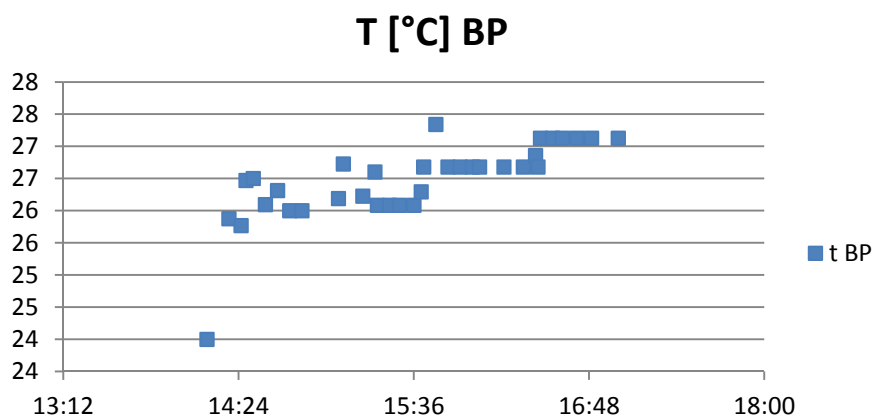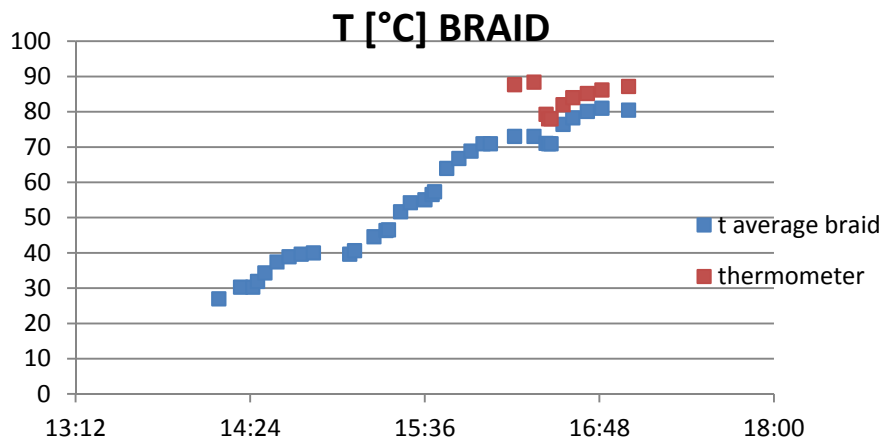
Figure 3.31 Thermal measurement from volt-amperometric insertion

Preliminary inspection was been made just by touching the braid in different points: it was found that the temperature near the power supply was clearly higher than the point where the thermocouple was placed; therefore a thermometer was used in order to acquire the new measurement point and the temperature was found almost 90°C; hence a fan was added (first orange line in Figure 3.30); after that also the air cooling of the RF coil was activated (second orange line). A picture of the layout is shown in Figure 3.32.

The different readings on the braid were due to the fact that in the path near the source, where the first thermocouple was installed, a lot of air produced by the cooling fans of the

source was present, so that the volt-amperometric measurement showed the average temperature of the copper braid.

As regards PG and BP it was observed that after the insertion of the fan [Figure 3.32] both temperatures decreased, suggesting that probably heat produced by the braid heated even the inlet cooling water; nevertheless no dangerous values were reported for PG and BP.

In conclusion, from this test is resulted that no heating problems are present on the grid feed-through even for 400A in steady state, as regard the braid it can work over 300A only if a definitive new fan is installed and preferably not continuously; in the future the braid has to be replaced by another one (or more in parallel) with a bigger cross-section, particularly when a new magnetic filter will be designed; currently an improvement up to 1kA is discussed; in chapter 6 the effects of the improvement of the filter will be analyzed.
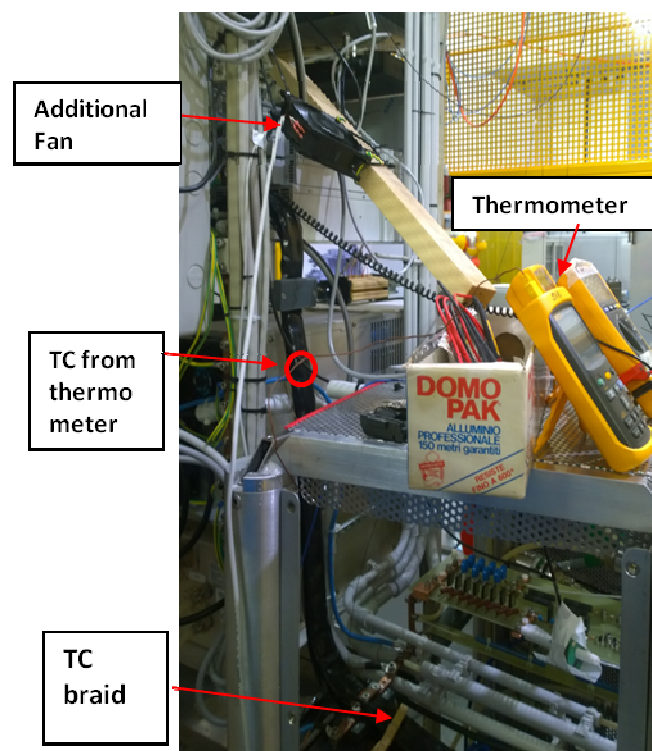

Figure 3.32 Picture of experimental setup.

4 Thermocouples

In NIO1, thermocouples are used both for calorimetry and for the safety of the device. In fact, the temperatures of the source and of the acceleration grids are continuously measured. Transducers based on thermocouple are widely used in several applications where a reliable, quick and robust measurement of the temperature over a wide range of values is required.

The working principle of the thermocouples is the thermoelectric effect (Seebeck effect). This phenomenon appears when a metal is exposed to a temperature gradient and exhibits at his edges an electromotive force E_σ (e.m.f) proportional to the temperature difference. Each metal is characterized by its Seebeck coefficient $\sigma(T)$, which depends on the temperature and relates the e.m.f dE_σ to the temperature gradient dT [1]

$$E_\sigma = \int_{T2}^{T1} \sigma(T)dT \quad .$$

In a fairly linear zone the Seebeck coefficient can be considered constant and therefore the e.m.f can be expressed as the difference of the temperatures through the metal as shown in Eq. 4.1

$$E_\sigma = \sigma(T_1 - T_2). \tag{4.1}$$

A thermocouple is made of two different metals joined at one end, the hot junction. Hence the electric potential varies in different way along the materials because they have different Seebeck coefficients and thus, since the potential at the common junction is the same, on the other side there is a potential difference dependent on the difference of the Seebeck coefficients of the two materials (Seebeck relative coefficient) and the temperatures at the ends is shown in Eq.4.2

$$E_\sigma = \int_{T2}^{T1} \sigma_A(T)dT - \int_{T2}^{T1} \sigma_B(T)dT = \int_{T2}^{T1} [\sigma_A(T) - \sigma_B(T)]dT \tag{4.2}$$

In order to read the voltage between the free ends, usually thermocouples are connected to other wires that carry the signal to the voltage sensor as shown in Figure 4.1. Whether these two wires are made of the same material and the new junctions are at the same temperature, actually the read voltage is the same as at the thermocouple termination because the contribution of the additional wires is a common mode voltage.
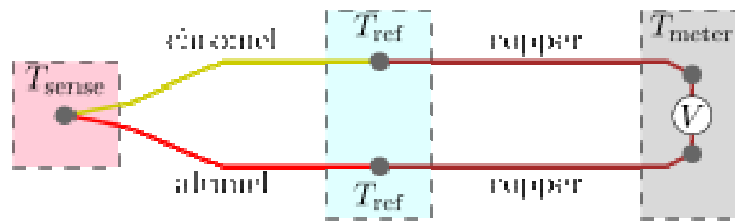
Figure 4.1 Thermocouple measurement system.

If a thermocouple shows a voltage V_a across it when its junctions are at T_1 and T_2 and a voltage V_b when the junctions are at T_2 and T_3, then when terminations are at T_1 and T_3 the voltage detected will be V_A+V_B.[1]

Temperature should be properly measured with the T_{ref} or cold junction at 0°C (ice point) (see Figure 4.1) in order to have a direct link of the voltage read and the temperatue of the hot junction as shown in Figure 4.2 since charts are referred to the cold junction at 0°C. In the case the cold junction is not at the ice point, in order to obtain the hot junction temperature an independent measurement of the cold junction is needed and typically it is performed by semiconductor sensors.

Then to compensate the reading, the voltage corresponding to the cold junction temperature has to be read and subtracted from the hot junction reading; therefore the result represents the right temperature of the hot junction.

4.1 Types and features

As previously said, different combinations of metals will produce different temperatures and these different metals will have different durability and strength levels. Thus some of these combinations have been standardized to exploit maximum outcome potential. Essentially on the market there are a lot of different types with different sensitivity, operating range and stability as summarized Table 4.1 [3].

TYPE	MATERIALS	TEMPERATURE RANGE [°C]	NOMINAL SENSITIVITY [μV/°C]
S	Platinum(10%)/ Rhodium -Platinum	-50/1760	9.6
R	Platinum(13%)/ Rhodium -Platinum	-50/1760	10.5
B	Platinum(30%)/ Rhodium - Platinum(6%)/Rhodium	0/1820	5
E	Chromel -Constantan	-270/1000	76
J	Iron -Constantan	-210/1200	58
K	Chromel -Alumel	-270/1370	41
T	Copper -Constantan	-270/400	52
N	Nicrosil -Nisil	-270/1300	36

Table 4.1 Main parameters for the common thermocouple types.

Since the sensitivity is not a constant parameter, but it depends on the Seebeck coefficient, the nominal sensitivity reported in the tab.4.1 has been defined as the linearization from 0 to 1000 °C (except T-type from 0 to 400°C) of the voltage-temperature characteristics [Figure 4.2].
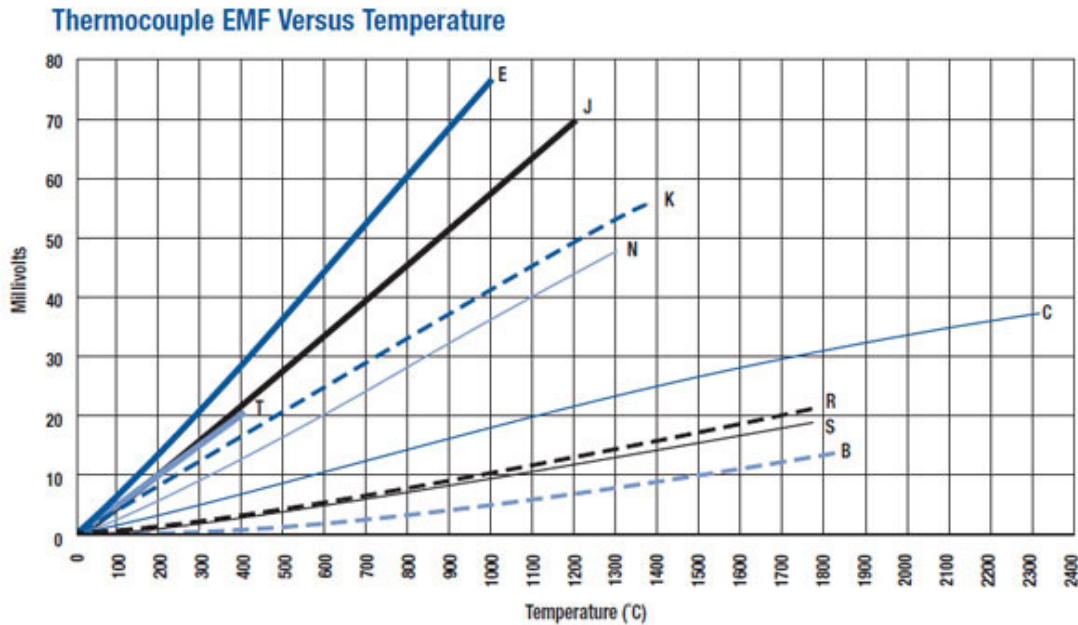
Figure 4.2 Voltage-temperature characteristics with cold junction at 0°C.

Looking at the main properties of the each type of thermocouple:

- T-type: this type is corrosion resistant in moist environment but the upper limit for the temperature range is the main disadvantage, and it is due to the fact that at higher temperatures there is copper oxidation if the thermocouple works in oxidant environment.

- J-type: like the T-type iron tends to oxidize for temperatures over 540°C, in fact the upper limit in the Tab. is related to O_2 free environment.

- E-type: this type is the most used because it has the highest sensitivity; the main disadvantage is that it is not suitable to reducing environment.

- K-type: they are resistant in oxidant environment but not suitable in vacuum because the chromium present in Chromel tends to evaporate; furthermore in poor oxygen environment corrosion problems are present.

- N-type: it shows greatly enhanced thermoelectric stability relative to the other standard base-metal thermocouple alloys because their compositions allow to virtually eliminate or substantially reduce the causes of thermoelectric instability[6]

- R, S, B types: these are the most stable thermocouples but the main disadvantage is due to the low sensitivity; therefore they are used only for high temperature ranges, furthermore the cost is higher than other types.

72

Usually thermocouples are embedded into a protection sheath made of metallic material or ceramic for high temperature applications. Depending on this sheath, three categories for each type of thermocouple are possible: ungrounded, grounded and exposed junctions.[Figure 4.3]
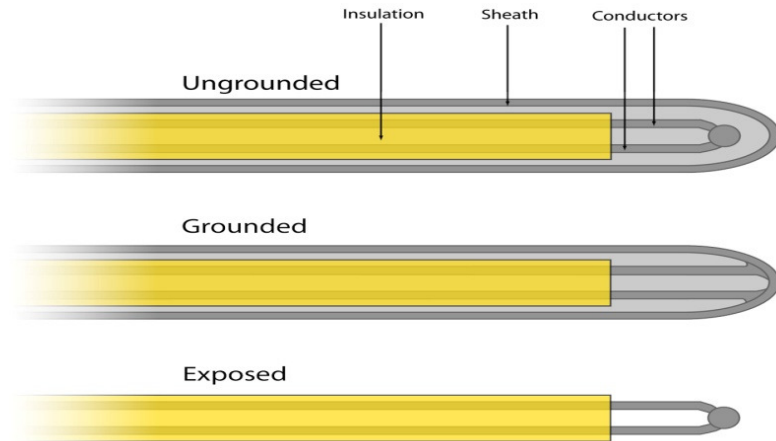

Figure 4.3 Thermocouples hot junction types.

In the ungrounded thermocouple, the hot junction is isolated from the sheath. On one hand this type of junction is suitable in the case of parasitic e.m.f that might distort the measure, on the other hand the response time is slower.

For grounded thermocouples, the sheath is connected to the hot measurement junction. In such way the thermocouple is both protected from external agents and the rising time is faster than the previous one; however ground loops can affect the measurement as described in the next section.

Thermocouples with exposed type junction have the fastest response but they might be subjected to ground loops and deterioration.

For all previous cases the time constant is proportional to the diameter of the probe as shown in Figure 4.4.
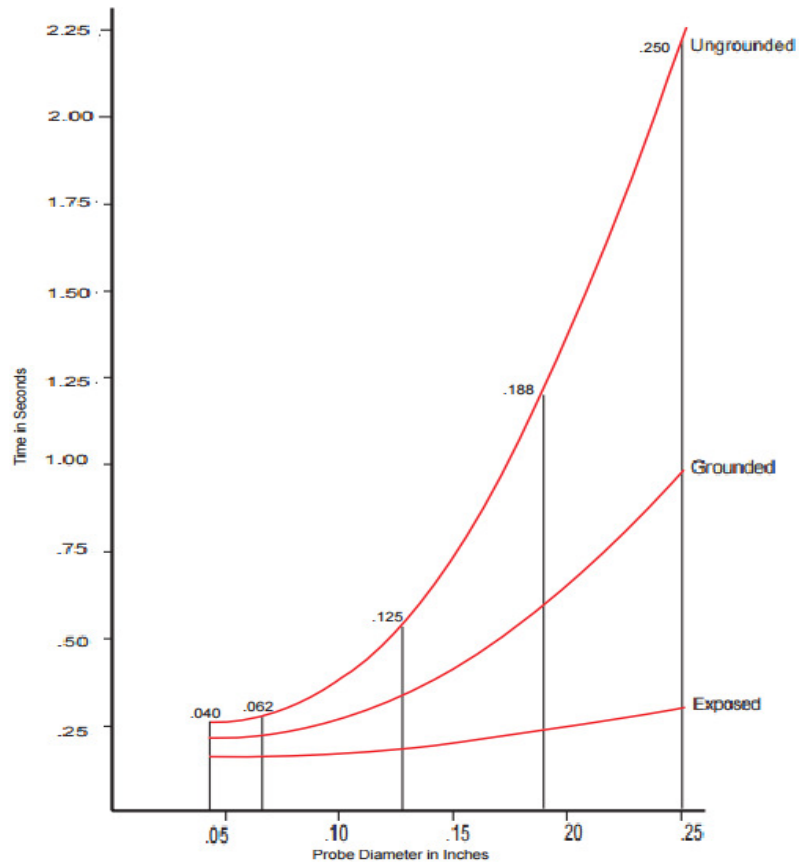
Figure 4.4 Time constant for junction types versus the diameter of the sensor.

4.2 Thermocouples board design

Thermal measurements are widely used in SPIDER, MITICA and NIO1 as described in *Chapter2*, as stand-alone diagnostic or complementary to other diagnostic system. So far, especially for those thermocouples which could suffer from HV breakdowns, commercial solutions (i.e. Analog Device conditioning modules series) capable of 1500 V rms continuous isolation have been adopted for the conditioning of the thermocouple output and integrated in the design of thermal measurement systems. Nevertheless, given the relatively high cost of these commercial solutions and their limited flexibility (i.e. 4Hz bandwidth, no temperature conversion), the development of a custom board for electronic conditioning of thermal measurements was required.

Special care must to be paid to the shielding of the thermocouples cables and the board itself in order to avoid the pick-up of the RF noise, which makes the environment very harsh.

Many layouts of the boards have been analyzed according to previous experiences collected in NIFS-RNIS (R&D Negation Ion Source, Japan), IPP-BATMAN (BAvarian Test MAchine for Negative ions, Germany) and the first prototypes of the boards for the grounded grid of SPIDER and for NIO1 [2].

Before presenting the details of the electronic board designed and realized during this thesis work, a brief description of the previous boards is reported as follows.

All previous boards had some main common stages [Fig.4.5]. First of all an *amplifier* typically with a gain of about one hundred is used in order to provide values suitable to the *ADC* (analog-to-digital converter). The ADC receives both the signal from the thermocouple and the signal for the cold junction compensation (another TC or a precision integrated-circuit temperature sensor). Once the signal is digitized, a *microcontroller* selects the channels one by one by means of *multiplexers* and sends the digital signal to a *transmitter* which communicates with the PC for the acquisition. Since the amplitude of the thermocouple signal is very small, particular care has to be paid in order to avoid RF noise affecting the signal before the amplifier stage.
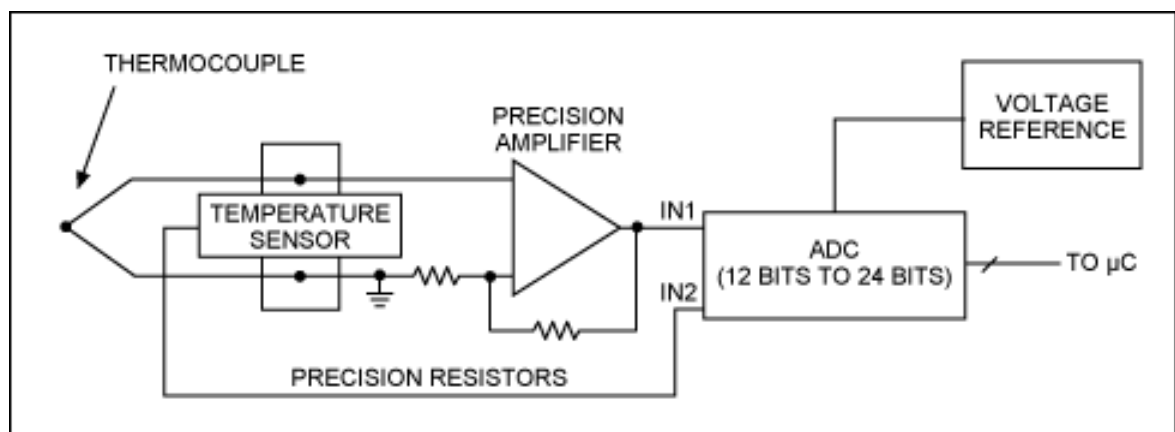

Figure 4.5 Schematic of a basic layout for the conditioning of the signal from a thermocouple.

The first board was developed for thermocouples embedded in the Grounded Grid of SPIDER, where grounded thermocouples must be used.

That board has 24 Channels and the sampling rate is 20S/s. Each channel is isolated from the others by Solid State Relays (SSRs) and from the transmitter unit by means of optical coupling. Signals coming from 24 single ended thermocouples are managed by a multiplexer scheme in which a microcontroller PIC® drives 3 multiplexers (1 every 8 channels) that activate the SSRs one by one letting the signal reach the operational amplifier.

Then the amplified signal is sent to the microcontroller PIC® for the digital conversion with 12 bits resolution; once the signal is digitized another channel is acquired until all channels are converted. When a complete package of 24 measurements is ready, it is sent through an optical fiber to the PC for the acquisition.

The optical fiber guarantees a total isolation between the board and the PC for the acquisition avoiding dangerous conditions for the operators and for the other several diagnostics that will equip SPIDER and will be connected to the same ground reference; it has to be reminded that during electrical breakdowns the potential of the SPIDER grounded grid can reach up to 20kV.

As regards the insulation of the board from the power supply, at first it was thought to use a battery which had to be placed inside the SPIDER vessel together with the electronic board; in this way there would be no electrical connections towards the outside of the vessel. Since the battery would be in the vacuum vessel it had to be charged by a small photovoltaic module located inside the vessel [Fig.4.15].

This solution is safe but there are some problems with respect to compatibility in vacuum due to the degassing of the battery, furthermore a very low power consumption design is required.

After this first release, for the experiments carried out at NIFS, a second layout of the board was developed [2]; this system was powered by an insulating transformer which can withstand up to 5kV since the expected overvoltages were weaker than in SPIDER.

The voltage coming from the transformer was filtered and rectified to the suitably value of 5V. Moreover an offset of 1.25V was added to the power signal in order to allow the operational amplifier to read also values for temperatures lower than the cold junction temperature (negative voltages).

In this way the temperature range was from -250 °C to 650°C with respect the room temperature covering the available voltage range of the amplifier.

As regards the other differences with respect to the SPIDER conditioning circuit, another type of SSRs was tested; the turn ON-turn OFF time was higher than the previous ones, 2ms were needed instead of 50µs, nevertheless the sample rate was 25S/s because of the reduced number of channels.

A third board was developed for thermal measurements in Mini-STRIKE installed in BATMAN, a revisited version of the previous one. Because the position of Mini-STRIKE along the beam line preserves the thermocouples from overvoltages, then the SSRs were removed; in this way the acquisition is faster because no time is lost for switching ON and OFF the relays.

In this board there were 8 thermocouples connected to the amplifier with differential configuration; therefore two multiplexers with 8 channels each were needed. The cold junction compensation was performed by a precision component, the LM35 integrated circuit, that detects the temperature on the electronic board. Like in the NIFS case, to allow the reading of temperatures lower than the cold junction, a 1.235V offset on the reference input of the amplifier was realized by LM385 integrated circuit.

Starting from experience gained with the boards previously presented, different components and layouts were chosen for the board developed during this thesis work and tested in NIO1 .

First, a new integrated circuit MAX31855, an analog-to-digital converter, cold junction compensated, was adopted instead of the operational amplifier.

The data output is a 14 bit signal with a resolution of 0.25 °C and the temperature range is from -270 °C to 1800°C; the sampling rate is 10S/s due to the time for the conversion of 100ms.

In the NIO1 board there are 8 channels, each one connected to a MAX31855, and there are no multiplexers. A PIC18F2423 selects one by one the channels by SD (select data) pin.

After a loop of the 8 channels the data output is converted to serial data (RS232) and sent to the port server.

The insulation between the board and the port server is provided by 2 optocouplers which can withstand up to 3.5kV; moreover the board is powered by an insulating transformer tested for 5kV that guarantees different references to the inputs side, before the optocouplers, and the output side, where the transformer is connected.

The aim of the work consists of the development of a new board which fits both with SPIDER and NIO1 requirements. All the previous cases have been carefully analyzed, highlighting the pros and cons for each board, in order to choose the best solution for the new conditioning circuit.

In fact boards based on the operational amplifier have higher sampling rates, mainly limited by the SSRs switching frequency, but a precision component for the cold junction compensation is needed and it has to be placed as close as possible to the amplifier where the cold junction is connected. Moreover a differential configuration for the thermocouples involves that 2 SSRs are needed for each channel, and an offset in the reference input of the amplifier is needed in order to read temperatures lower than the cold junction temperature.

As regards the conditioning electronics for TCs based on the MAX31855 the main advantages are represented by the high precision of the component (±2°C for temperature ranging from -200°C to 700°C), the wider range of conversion and the simple layout of the board; moreover the input from TCs is digitized, compensated and converted directly in the temperature of the hot junction.

Main disadvantage is due to the fact that during experimental tests on the old NIO1 board, it was noticed that when at least 2 exposed TC were placed on the same ground reference, a fault bit has been generated from the MAX31855 making the measurement not reliable. [Figure 4.6]

Figure 4.6 Fault detection signals from MAX31855.

The problem was investigated and was temporarily solved by insulating the TCs hot junction with Kapton tape; however the design requirement for the Grounded Grid of SPIDER is to use grounded junctions directly in contact with the grid in order to have the maximum sensitivity.

A research of another similar component, without fault detection, was made but only LTC2983 Multi-Sensor High Accuracy Digital Temperature Measurement System was found.

This integrated circuit has 20 input channels available, hence 9 thermocouples in differential configuration can be managed by a single component; the other 2 channels must be used for the cold junction compensation which can be made by a thermistor, RTD or a diode. The main limit of this component is represented by the time for the conversion, 167ms per channel, limiting the maximum sampling rate to 6S/s.

Therefore it was chosen to develop a new board by still using the MAX31855 and trying to fix the problem of the ground loop fault detection. As written in the component datasheet [Figure4.7] during fault detection switches S4 and S5 are opened, the internal ground reference S3 is open, S1 and S2 are closed.

In this phase the component checks if there are thermocouples shorted to the VCC or the GND of the component or if there is an open circuit; for each different fault the respective bit D2, D1 or D0 goes high.
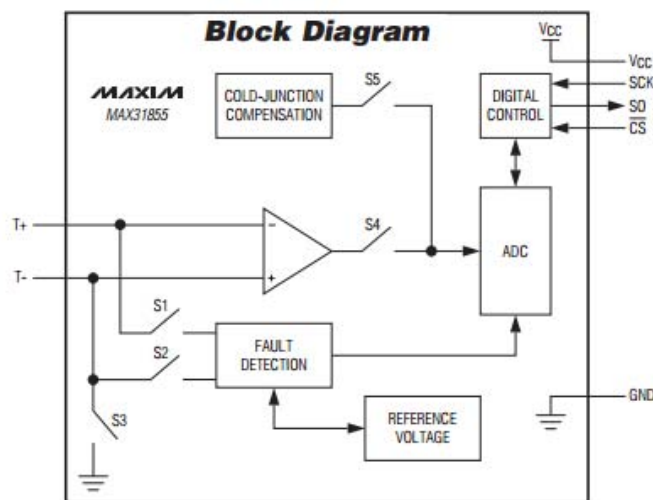

Figure 4.7 Max31855 block scheme.

78

It was found that the component, during the GND fault detection, tries to force a small current through the thermocouples wires. Only if there is a ground loop this current can flow and hence the component can detect it. [Figure 4.8]
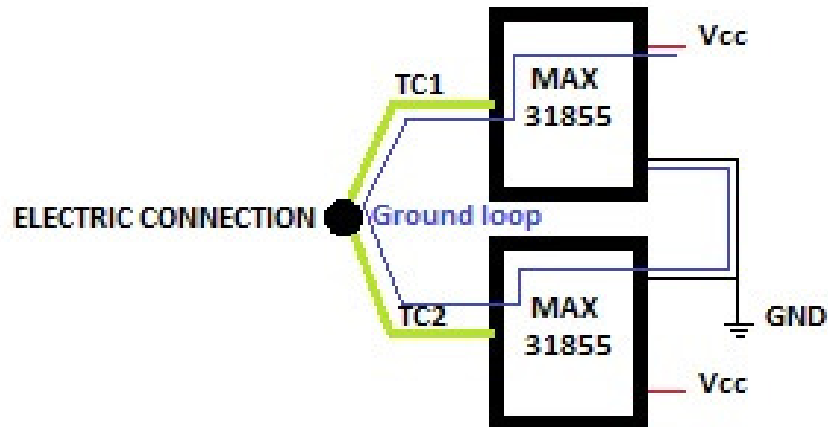

Figure 4.8 Ground Loop with 2 MAX at the same ground.

Ground loops have to be avoided in thermocouple measurements since the current which can flow along the thermocouples generates a voltage drop which alters the real value of the temperature.

In order to avoid the loop, the first solution discussed was the insertion of two analog switches between each thermocouple and the ADC converter input; in this way it is theoretically possible to acquire the signals from the different channels one by one with the other channels opened.

The main problem associated to this solution is represented by the synchronization of the analog switches and the MAX31855 serial interface protocol. To be more precise, during the conversion time (100ms) three functions are performed: the temperature conversion of the internal cold-junction temperature, the temperature conversion of the external thermocouple, and the detection of thermocouple faults; while chip select input CS is high, fault bits and temperature are updated; then when CS is forced low by PIC, the data are read.

In order to be sure to read only correct values, the firmware has to be set as follows: all switches have to be open except those ones associated to the channel that has to be read, during this phase CS has to be high; then, after the conversion time of 100ms, CS has to be forced to low state therefore reading is performed, moreover the two switches of this channel have to be open; after that cycle another channel can be read in the same way.

The problem associated with this firmware is the time needed for a whole cycle of 8 channels of 800ms, it means that the sample rate will be 1.25Hz.

For this reason, another approach was adopted: since the ground loop is expected to be due to the fact that all the ADC are connected to the same ground reference, a first test was performed in order to verify this fact by a very simple circuit built on a stripboard in which just one channel is present [Figure 4.9]
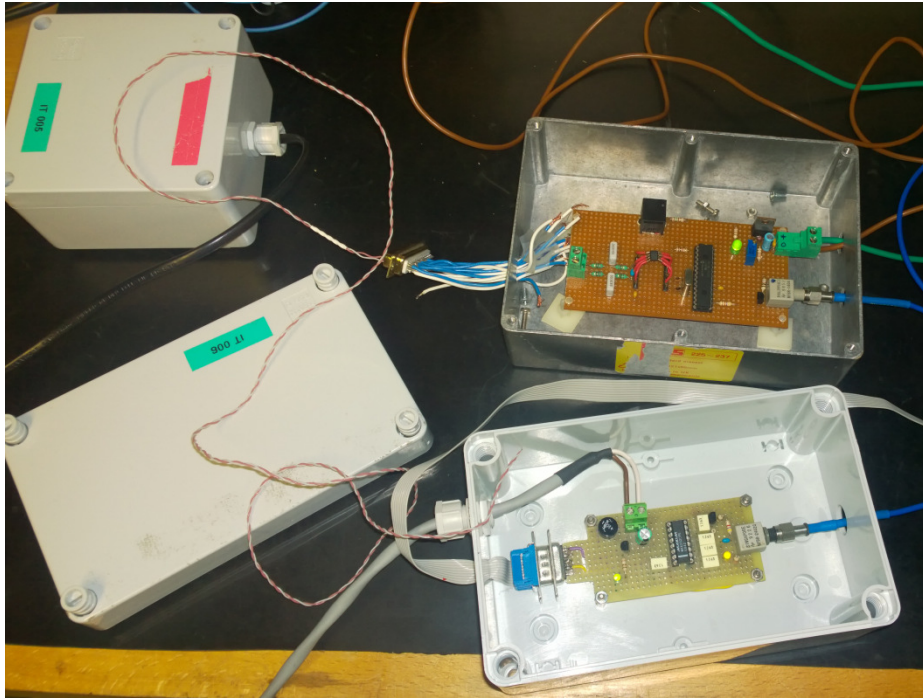
Figure 4.9 Preliminary test setup with 1 channel strip-board to investigate ground loops.

The test circuit was composed essentially by one exposed N-type thermocouple, one MAX31855 ADC converter and one PIC. The board was fed by a Bench Top power supply (which has an internal ground decoupling); the output data are sent through an optical fiber to an optical receiver where the digital signal is converted to the RS232 standard and sent to the PC for the acquisition.

First test was made by placing the measuring head in contact with some different points in order to check when the fault to GND was occurring; the selected points were the ground of the board and the ground of the workbench.

This test confirmed what had been supposed because the fault to GND was present only by touching the ground of the board with the thermocouple head.

A second test was carried out by using the test board with 1 channel and the board mounted on NIO1 at the same time. The aim of this test was to use two boards with different ground reference and check if the two systems can read the temperature when the thermocouples are electrically connected.

The test board was fed with the Bench Top power supply and the NIO1 board was powered by its own transformer with the primary winding connected to the electric socket of the workbench.

On each board one thermocouple was connected and then only the signal of the test board was monitored; otherwise two PCs would have been necessary for the acquisition. Then the two hot junctions were shorted and no faults were detected.

These tests revealed that the ground loop fault detection can be avoided by feeding each ADC converter with different power supplies, therefore two solutions for the development of the new board have been considered.

The first one consists in using 8 small transformers, one for each ADC. On one hand it represents the cleanest way to feed the ADC converters, on the other hand one rectifier is needed after each transformer, hence the layout would be a little bit complicated.

Another solution considered is to use 8 DC/DC converters instead of the transformers. This solution would be suitable because of the small size and the 8 rectifiers are not needed, however the noise due to the high commutation frequency of the DC/DC converters might compromise the accuracy of the MAX31855 reading.

In order to analyze the behavior of the ADC converter when it is fed through DC/DC converters, a first test was made by adding the conversion stage on the strip-board circuit previously seen. [Figure 4.10]
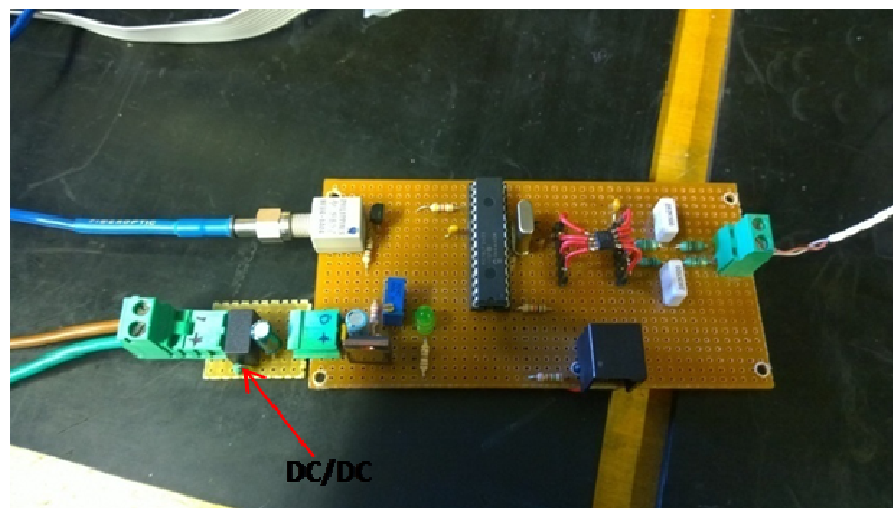

Figure 4.10 Test board improvement with DC/DC converter.

Then the signal from one thermocouple was acquired and it was compared with the signal previously collected with the board powered directly by the Bench Top power supply. It resulted that the noise produced by the converter is well rejected by the MAX31855 as shown in [Figure 4.11]; the small ripple of 0.25 °C is due to the resolution of the component.
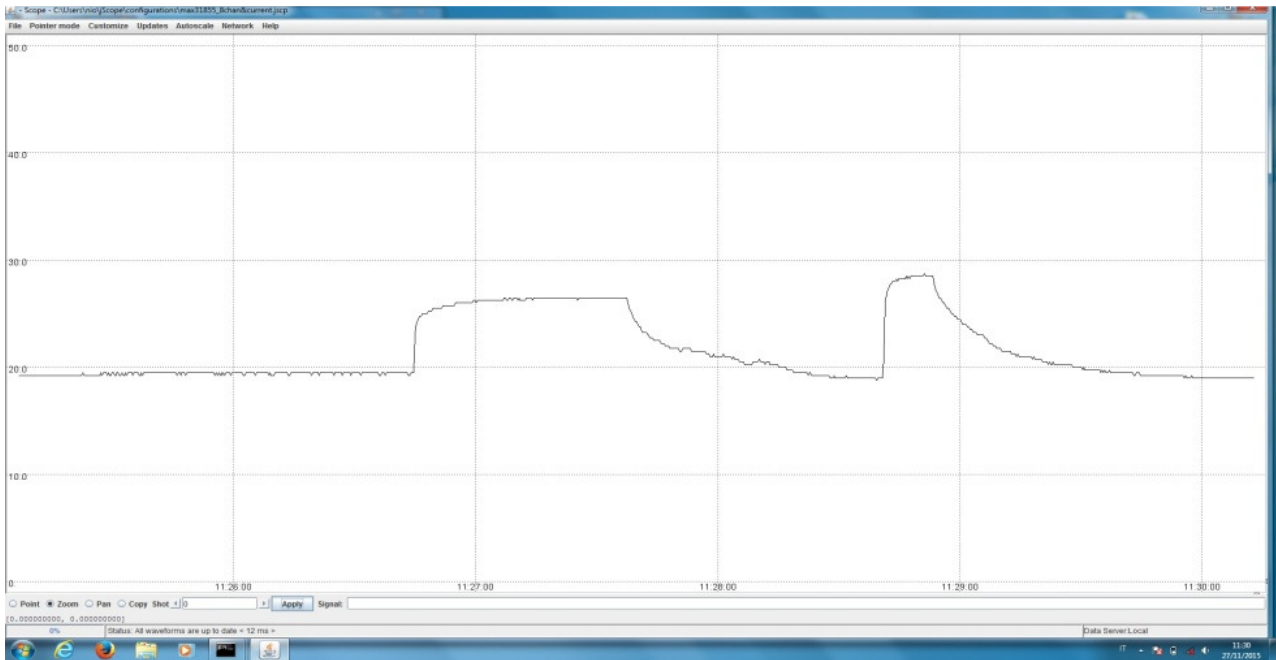
Figure 4.11 Temperature signal coming from test board with DC/DC converter.

The positive result of the tests drove the choice to use DC/DC converters, instead of transformers, in order to avoid the ground loops and hence also fault detections.

Before developing the full prototype with 8 channels a smaller board with just two channels was developed in order to test the new solution on NIO1 where RF noise and high voltages are present.

Thermocouples are connected to the board by two clip type terminal blocks, then each channel is filtered by a LC filter made of a ferrite bead and a 10nF capacitor; moreover a gas discharge tube (GTD) is connected to the thermocouple inputs in order to protect the board from the possible overvoltages carried by TC wires.

The signal is acquired by the MAX31855 which performs the amplification, the cold junction compensation and the digitization of the signal. Then it is sent by the signal output pin (SO) to one of the microcontroller (PIC18F2423) digital input pins through a high speed optocoupler.

Afterwards the data is sent from the PIC both to an optical head and to a transceiver, which synchronizes the output with the RS232 protocol; in this way the board is dual output providing more flexibility.

Each ADC is fed by its own DC/DC converter and since the microcontroller is powered by the main power supply of the board (battery or transformer), for the purpose of keeping the two ground references separated, two bidirectional optocouplers were installed on the connections between the PIC and each ADC.

In fact the microcontroller has to provide the serial clock signal, generated by an external 4MHz crystal oscillator, to each ADC in order to synchronize the operations, then it has to select the channel for the reading by chips select and the ADC has to send the output to the microcontroller.
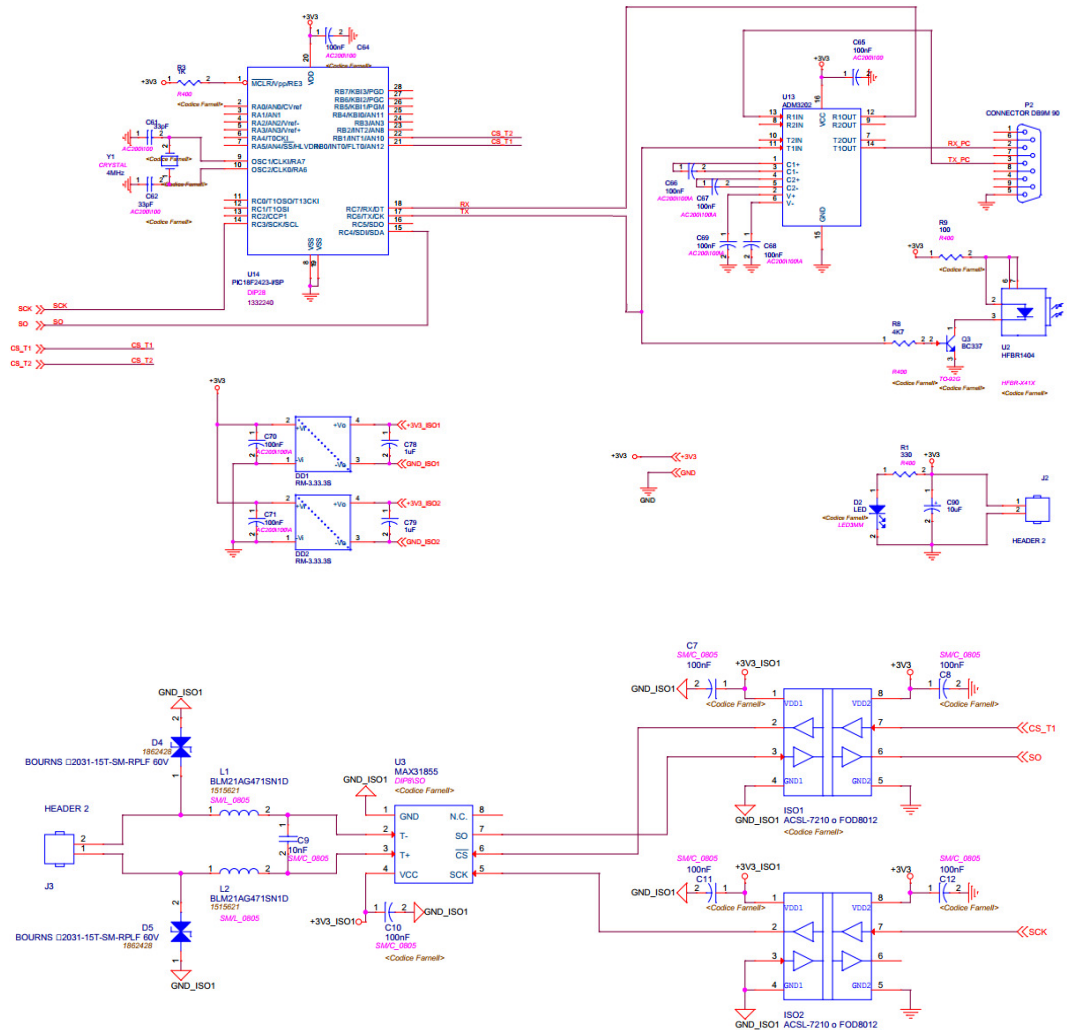
The schematic diagram is shown in [Fig 4.12]

Figure 4.12 Schematic of the new test board with two channels: master unit (upper), 1 channel (lower).

After the design phase, the board was machined and the components installed. In Fig.4.13 the main components are highlighted.
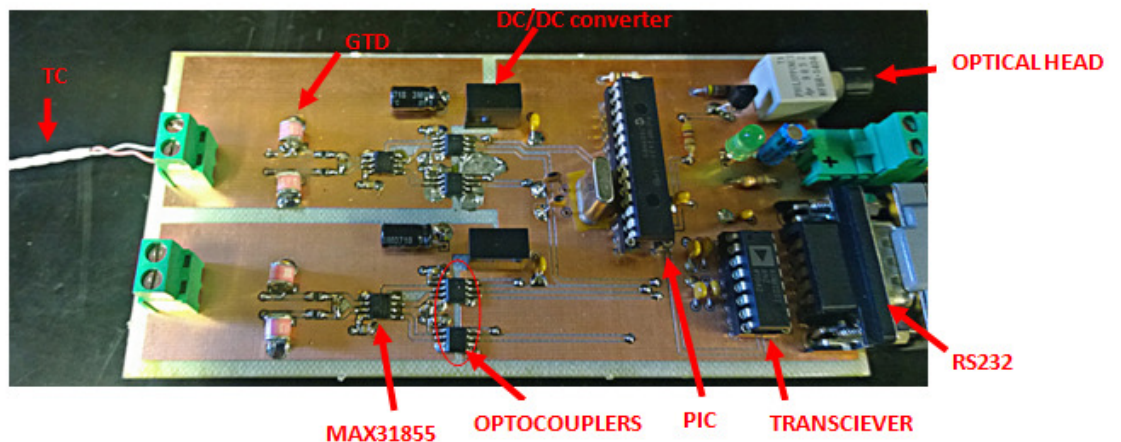

Figure 4.13 Picture of the new board.

83

Before installation on NIO1, the board was tested on the workbench by connecting two N-type thermocouples with the aim to verify the good quality of the signal measured and the absence of ground loops. During this test a problem arose: all 3 fault bits went high at the same time and hence no reading was possible. The problem was investigated using an oscilloscope, by watching the signal on the SO line and an anomaly was detected just after the optocoupler outputs. While the magnitude of the digital signal (SO) on the ADC side was a sequence of values between 0 and about 3V (Vcc is 3.3V), on the PIC side this signal was not the same, but another sequence of pulses with a maximum magnitude of about one volt was detected. A hypothesis was that, since the optocouplers are not three state chips, when one channel is activated for the reading by CS, the optocoupler on the SO of the other channel has its output at a low impedance state hence the digital signal coming from the reading is shorted. Therefore a diode was soldered on the output of each optocoupler on the signal output channels. Then a resistor connected between the cathode of the diode and ground was needed in order to let to the charge on the SO line flow out when the output is forced to low state for the 0 logical.

After this upgrade, the board was tested again and no fault bits occurred even if the two thermocouples were shorted, furthermore no noise or bad readings affected the measure.

The board was then placed on NIO1. In particular the acquired thermocouples are located on the Extraction Grid cooling circuit; one is on the inlet and the other is on the first outlet.

For the first test the board was powered by a transformer connected on the HVD and then the voltage is rectified, filtered and adjusted to 3.3V. Anyway the thermocouples are kept isolated from the EG pipes by several layers of Kapton.

The board was laying on the basement of the HVD, next to the Matching Box, and embedded into a metal box in order to provide an EMI shield, then the signal was acquired by an optical fiber and thus carried outside the NIO1 box to the PC for the acquisition.

Also thermocouple wires are shielded by a copper braid which is connected to the HVD at both terminations.

From the first tests some issues during the NIO1 operations emerged: when RF forward power was over 50 W, an offset in the temperature appeared, furthermore as long as the plasma was off the noise was proportional to the RF forward power. Then once the plasma was switched on a strong step in the measure was present until the plasma coupling became inductive where just a small offset of about -4°C still remained.

The problem was investigated by moving the board from the base of the HVD to a slot located in the highest part of the NIO1 rack (DAQ) in order to check if the noise pick-up was lower. Moreover as regards the supply unit, the transformer was removed and a battery with a voltage regulator was installed with the aim to check if the noise was due to the pick-up of the noise along the power line. In [Figure4.14] the behavior of the signals collected with the previous set up is shown, and it was the same as in the case of the transformer as a power supply; this test proved that the noise does not come from the power supply line, hence it comes from the thermocouple cables or from the RF noise induced in the board itself.
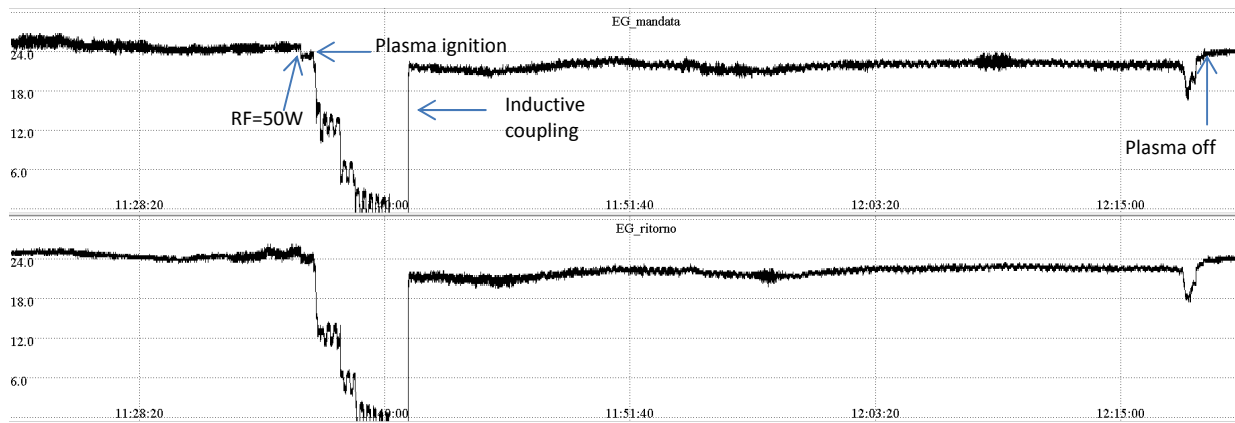
Figure 4.14 temperature signals from the new board fed with batteries and subjected to RF and Plasma noise. EG flange inlet (upper) and outlet (lower).

With the purpose to understand if the noise was carried by the thermocouples, a trick was thought: since if there are no thermocouples connected to the MAX31855, an open circuit fault bit is generated, thermocouples was removed from the board and a short circuit between the T^+ and T^- inputs was made.

Since the ADC converter detects a constant input of 0V, the output has to be the internal temperature of the chip, otherwise it means that RF noise is picked up from the board.

The test showed a very stable trace even during the plasma ignition, the maximum RF forward power given by the power supply during this session was 600W and no noise was present in the signal.

To summarize, during the operation of the last thermocouple electronic board there were two main issues to be solved: the galvanic insulation of the board and the possibility to use a system which works with the commercial electronic ADC converter (MAX31855), instead of the operational amplifiers, with grounded thermocouples.

About the galvanic insulation, the problem is due to the fact that in many cases thermocouples are directly in contact with components that may be biased at different potentials compared to the acquisition system and to the ground reference of the power supply of the board.

For example on NIO1 the TCs of the EG cooling systems are insulated by several layers of Kapton from the Extraction Grid, which can be biased up to 10kV compared to the potential of the HVD where the board is placed; this is not an optimal solution because the system is not as sensitive as the TC directly in contact with the pipe because the layers of Kapton act as a thermal insulation between the TC head and the measurement point of the cooling circuit. Furthermore it works like a "low pass filter" preventing the detection of fast variations of the temperature.

4.3 Thermocouples embedded in the Grounded grid of SPIDER

The aim is to develop a board that fits both on SPIDER Grounded Grid and NIO1 without any problem of insulation among the board, the PC for the acquisition of the signals and the power supply.

On SPIDER there are further constraints with respect to the NIO1 EG: from simulations the magnitude of the GG overvoltages during breakdowns will be up to 20kV, hence the insulation module must be placed inside the vessel because vacuum compatible electrical feedthroughs have lower breakdown voltage.

The insulation module will be placed in a box with the electronic board that will be located inside SPIDER vessel. In Figure 4.15 a sketch of the first prototype of the SPIDER thermocouple measurement system is shown.

For the new solution the thermocouple board will be mounted on a metal box fixed to the grounded grid frame below the termination box where the transition from Mineral Insulated Cable to Kapton insulated cable takes place. Since it will be in vacuum there are several problems for heat dissipation because the main way to thermal exchange is radiation, which is efficient at higher temperatures with respect to convection.
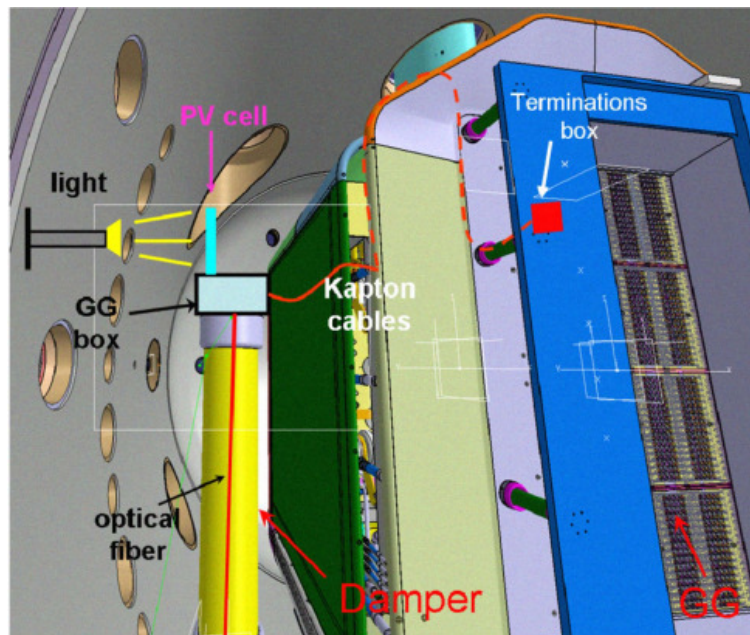

Figure 4.15 Position of the Grounded Grid Thermocouple BOX inside SPIDER.

For these reasons it was chosen to design a system that is small, with low losses, vacuum compatible and with a high breakdown voltage.

To choose the best solution many configurations for power supply were analyzed; the first idea was to search for a commercial integrated circuit based on wireless power transfer technology (WPT) which would have the main advantage to be a very compact solution that fits perfectly on the printboard and with very low power consumption. The main

requirements of the system were 5V DC or more as output voltage, 2VA of transferable power with minimum one centimeter distance between the two coils to ensure enough breakdown voltage by assuming 3kV/mm for dielectric strength; for SPIDER this is a cautionary value since at the high vacuum level inside the Vessel (<0.1Pa) voltage holding is higher and depends on the electrode distances.[5]

After a commercial search, the only components found with the previous features were Linear Technologies LTC4120 receiver and Texas Instrument bq501x receiver with its controller bq500210.

As regards the LTC4120 main disadvantage is due to the fact that the component works only with a battery as a load otherwise the control system of the output generates a "sleep mode" signal. This feature is aimed to detect bad battery status; hence a battery would be needed but the vacuum compatible constraint would not be satisfied. For the bq501x and bq500210 the problem is that, as shown on the datasheets, the transmitter circuit that has to be interfaced with the controller is quite complicated and it requires a lot of components and hence more space on the print-board with respect to a little insulating transformer.

For the previous reasons it was decided to use a small transformer which represents the simplest solution for the board galvanic isolation; however after a commercial search it was found that there are no transformers with the features needed. Therefore a preliminary design to choose the material, frequency, core size and number of turns was made and is presented in the next section.

4.3.1 Insulating transformer preliminary design

At first a preliminary design with ferrite cores already in stock was done; the number of turns was evaluated with the following model, Eq.4.3, which works in sinusoidal steady state:

$$V_{1n} \approx \sqrt{2}\pi f N_1 B_M S \qquad (4.3)$$

For the ferrite core, saturation induction is about 0.3-0.5T [4] hence to minimize number of primary winding turns N1, without increasing too much the magnetizing current that is proportional to BM, a value of BM= 0.25T was chosen; nominal primary voltage V1n was set to 24V that is a value easy to obtain by a commercial (220V/24V) transformer which will be placed outside SPIDER vessel; with this solution the number of primary turns is lower than the case with the direct 220V feeding and so also the thermal losses in the copper wires with same section.

With 24V for primary voltage and BM=0.25T an investigation was carried out to choose the size of the core with the constraint to have less than 100 turns for the primary winding with a

maximum outer diameter for the core of about 6cm in order to have a suitable footprint for the board.

Under these constraints some cores with different sections S were considered; thus for each one, the number of primary turns and the work frequency were selected in order to find the best compromise.

A suitable choice was a toroidal ferrite core (Wurth Elektronic 74270191) with characteristics shown in Tab.4.2
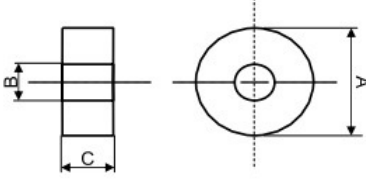
	A[mm]	61.0
	B[mm]	35.5
	C[mm]	20.0
	S[mm^2]	255

Table 4.2 Geometrical dimensions of the Ferrite core chosen.

This choice was made by choosing the core with the biggest section in order to keep the product N1f in Eq.4.3 as low as possible; in this way for a fixed frequency the number of turns is minimized: e.g. with a frequency of 1kHz the number of turns for the primary winding is 85.

Nevertheless having a few turns implies to work with a higher frequency with respect to the industrial one of 50Hz, increasing the complexity of the circuit by introducing an additional stage before the transformer, in which the needed frequency has to be generated.

For this reason another solution was evaluated: instead of the ferrite core an iron-silicon alloy core was analyzed since it saturates at higher values for the induction (1.5-2T)[7], hence the product N1f can be further decreased.

With the purpose of working at the industrial frequency of 50Hz, with an induction value BM of 1.5T, the number of needed primary turns was calculated (N1 =255) and the secondary (N2=59) evaluated by the voltage ratio K as follows (Eq.4.4), where V2n is the secondary nominal voltage set to 5V.

$$K = \frac{V_{1n}}{V_{2n}} \cong \frac{N_1}{N_2} \qquad (4.4)$$

These results have lead to the idea to decrease the nominal primary voltage up to 5V by the introduction of a 220V/5V small commercial transformer, which was found as a commercial device, to feed the isolation transformer, making it possible to reduce further the number of turns for the primary winding up to 59 like the secondary ones.

In this way the transformer will be easier to be wound and the minimum overlapping of the turns provide the best solution for the thermal exchange.

To summarise, the insulation module for SPIDER will be made of a small commercial transformer placed outside the vessel, then it will feed an insulation 5V/5V transformer placed inside the SPIDER vessel. In this way strong overvoltages brought inside the board by

thermocouples will not be dangerous for the external equipment since the secondary of the insulation transformer and also the board will be floating and the primary connected to outside will not be affected by overvoltages.

Further a numerical model of the transformer which takes in account the thermal exchange at low pressure, the conduction, the power losses in the core and the Joule effect in the winding should be done in order to choose the current density in the winding and therefore the section, by considering that the copper wire must not exceed a temperature of 200°C in continuous operations.[8]

5 Current measurements

With the aim to evaluate the beam current, different approaches are possible, the most direct method would be to measure the current delivered from the AGPS since the beam particles that cross the Extraction Grid are related to it. To be precise all charged particles at the HVD potential going to ground are taken in account in the AGPS current, therefore also the leakage current from the HVD flowing through ground connections (ceramic insulators, parallel resistors, water cooling pipes, gas pipe) have to be considered.

Theoretically the leakage current can be evaluated without plasma generation by a voltage scan and then it can be subtracted (at the corresponding extraction and acceleration voltages) from the current read during beam extraction; this way it would be possible to calculate the beam current.

In Figure 5.1 an AGPS voltage scan without plasma generation is shown; it has been obtained with the EGPS disconnected and without gas injection, in blue and red are signed respectively the voltage and current read from the power supply, then the ratio has been computed and the equivalent resistance at the AGPS output is shown in the bottom figure. Main problems connected to this approach are noise present in the current signal of about 0.5mA (see red curve) and the uncertainties for example due to the discretization of the power supply since it works on 12bit with a full-scale of 171mA and therefore less significant bit is 42µA.

Thus, in particular for first operations with extraction and acceleration, where the beam current is very low (less then 1mA) as described in Chap 6, other systems are needed in order to measure small currents.

Furthermore a good way to study the beam optics is to distinguish the beam current due to particles impinging on the PA grid from that carried by particles impinging on the CFC calorimeter; for these reasons two current sensors were developed as described in next sections.
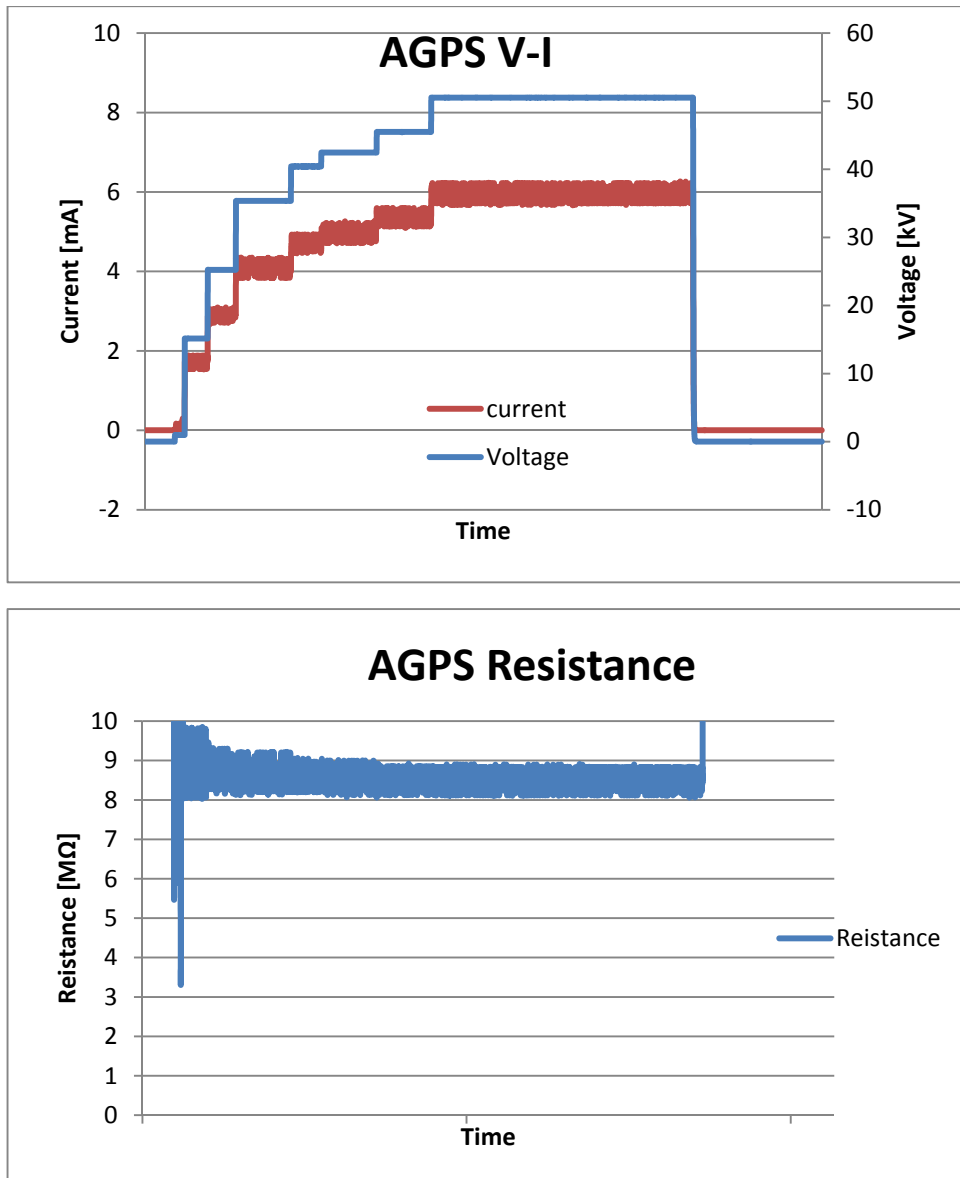
Figure 5.1 Voltage scan with EGPS disconnected and no gas injection (upper) and load resistance at the AGPS output (lower).

5.1 Mini-STRIKE upgrades

In this section a new equipment will be presented designed and installed on the CFC tile (Mini-STRIKE) that was designed, built and installed in order to measure the beam current collected by the tile.

Basically the system is made of a shunt resistor connected to the tile and the current is evaluated from the voltage measured by a digital multimeter upon knowing the value of the resistor.

This measurement is very useful, in particular where the magnitude of the current is low and the beam is not well focused because in this case the calorimetric evaluation is a very slow method compared with the previous one; the main limit of the shunt method is that provide an integral measurement of the current and the value of the resistance might change because of the heating due to the current flowing thorough the resistor, furthermore some electromagnetic noise might be picked up from the circuit.

In next chapter a comparison between the calorimetric evaluation and the direct measurement of the beam current is made in order to verify the accordance of the results from the different methods.

Since Mini-STRIKE is inside the vacuum vessel it was necessary to open the port near the tile and hence the vacuum was lost, then the tile and its metallic support were removed. [Figure 5.2]

Figure 5.2 Mini-STRIKE removal from the NIO1 vessel.

Afterwards the tile was analyzed and a round pattern was found at the center on the side facing the beam direction. Since the tile was cleaned before plasma operations with after the vacuum leak, it is expected that this round pattern is due to an impinging ion beam; furthermore the metallic support was modified allowing a vertical orientation for the tile in order to comply with the expected deflection of the particles due to the source magnetic fields during the following operations (see next chapter for details).

After that, a copper wire was connected between one pin of the vacuum feed-through and the tile support. Finally the tile was replaced inside the NIO1 vessel while insulating, the support from the vessel by a Kapton film [Figure 5.3], unlike the previous installation, in order to avoid any connection to ground other than the shunt; in this way all the current associated to particles collected by the CFC tile can be measured.
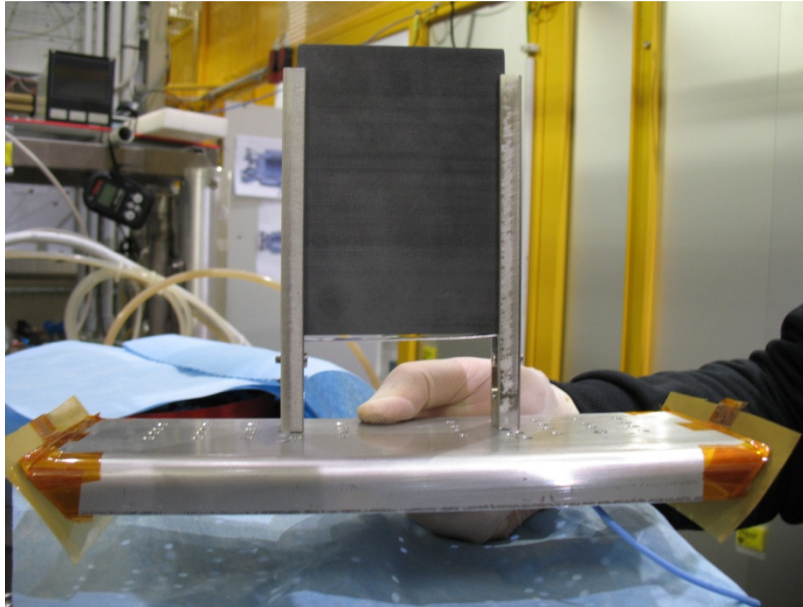
Figure 5.3 Rotation of mini-STIKE and support insulation.

5.1.1 Mini-STRIKE current sensor

With the aim to measure a DC current in the range from 1µA to 1mA, in accordance with the experimental results shown in the next chapter, two sensor types were considered: Hall effect sensors (LEM) and resistive shunt.

The main limitation for the first one is the small current range that has to be measured: sensors in the microampères range are quite expensive; moreover this system represents a transient solution because in future higher current is expected as the experiment performaces improve. Hence shunt resistor connected between the tile support and ground was chosen to have a cheap, simple and fast solution for current measurement.

Another issue is due to the fact that for each negative ion impinging on the CFC tile, many electrons present in the tile are extracted from the surface (secondary emission phenomenon). Therefore Mini STRIKE has to be polarized with positive polarity so that secondary electrons are kept inside the material and the current measured is due only to the beam.

Strictly speaking, like this the system is complete for the measurement. Nevertheless some safety problems might arise if the connection from the tile to ground breaks outside the vessel.

In this case the CFC tile will be like a capacitor and the tile will charge up to the potential of the plasma source with respect to the ground potential; for example a negative ion beam accelerated to 60keV will charge the tile up to 60kV.

For this reason it was decided to connect a passive protection made of MOVs, with a clamping voltage of about 100V, between the outer side of the vacuum feed-through and ground; and

another metal oxide varistor, with clamping voltage rating of about 30V, was connected in parallel to the voltmeter to protect the gauge in case of overvoltages. A scheme of this circuit is shown in Figure 5.4.
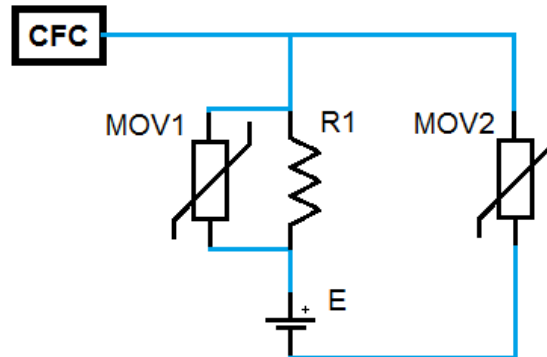

Figure 5.4 Scheme of the current measurement system of Mini-STRIKE.

The following components were chosen as available in stock:

- R1: R= 10 kΩ   P=1W
- MOV1: Clamping voltage=30V
- MOV2: Clamping voltage= 2 x 60V (series connection)
- E: Gps3303 Gw insteck Vout max= 60V

The resistance value was chosen in order to have suitable values for the voltages within the expected current range (1µA to 1mA): with 10kΩ the voltmeter can easily measure values from 10mV to 10V; the maximum power losses in the resistors with 1mA are 10mW.

On one hand MOV 2 must have a clamping voltage higher than the maximum rating from the polarization power supply E since the maximum voltage on the varistors is the power supply output plus the voltage drop on the shunt resistor and during normal operations leakage current through MOV2 has to be negligible; on the other hand too high clamping voltages would be dangerous for the operators. Hence 120V was chosen for the clamping voltage.
As regards MOV1 it will be subjected to maximum voltage on the shunt (10V), thus a clamping voltage of 30V is enough.
Power supply maximum voltage probably is enough to stop secondary electron emission like in the NIFS case [1], but this will be experimentally verified once the whole circuit will be in operation.
Finally the system was built and each varistor was tested with the aim to identify their real characteristics, in particular the leakage current during the normal operation of the experiment and the clamping voltage; two tests with different layout were made as follows.

TEST MOV1 (30V)

The purpose of this test is to evaluate the leakage current of the MOV1 by biasing it from 0 to 60V and by placing particular attention to the value for 10V, being it the voltage related to 1mA through the shunt resistor. The test circuit is shown in Figure 5.5.
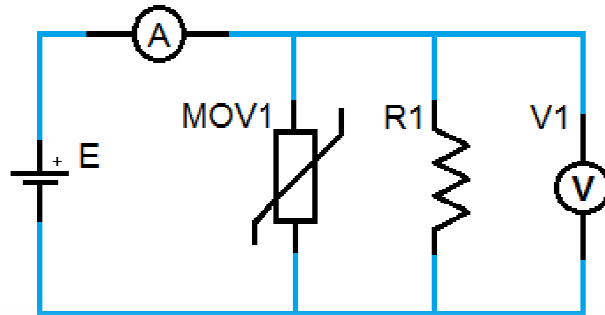

Figure 5.5Test circuit to evaluate the MOV1 V-I characteristic.

The current measured by the ammeter A is expected to flow mainly in the resistor because the voltmeter and the varistor impedance are greater by several orders of magnitude until the varistor begins to conduct; moreover since the resistor has a fixed resistance value of 9.96kΩ (heating is negligible with these values for the current) the current through the resistor can be calculated by the Ohm's law and then the current through the varistor can be evaluated by subtracting it from the total measured current (the small current absorbed by the voltmeter is neglected). The results of this test are shown in Figure 5.6.
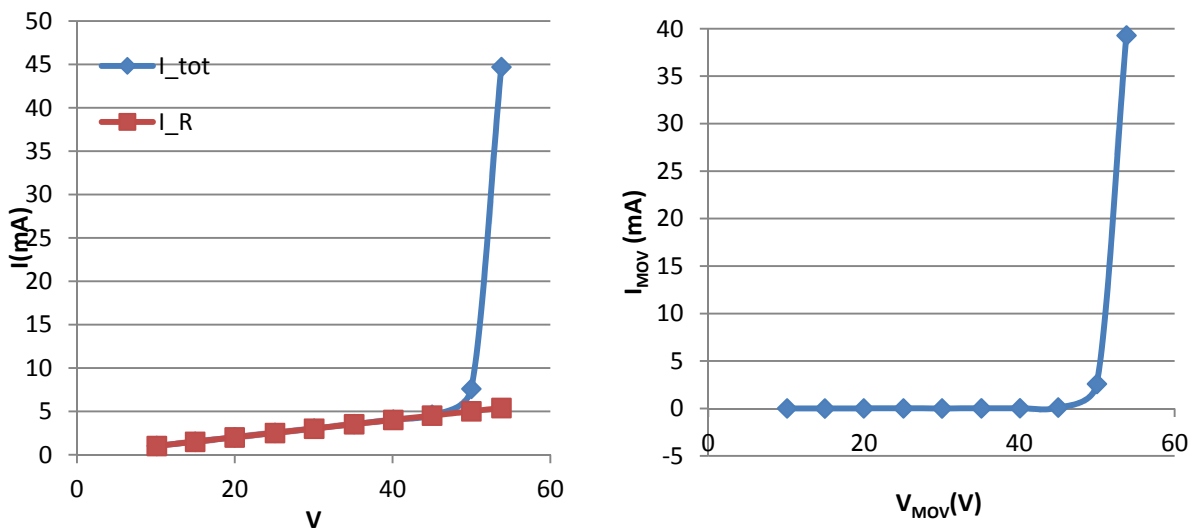

Figure 5.6 V-I characteristic of MOV1 parallel to R1 (left) and MOV1 characteristic of MOV1 (right).

The point at 60V is not present because the respective current of 461mA is out of range, furthermore the varistor was very hot at this value.

It is concluded that the varistor works and at about 45V it begins to conduct electric current (0.1mA), furthermore at 10V the current is negligible (15µA) with respect to that flowing in the resistor (1mA).

TEST MOV2 (120V)

In this test a different layout was tested in order to find both the characteristics of MOV2 (two varistors connected in series) and to test the whole circuit.

The aim of the measurement is to verify the leakage current of the varistor series block, in particular at the value of about 50-60V, which is the more critical condition for the accuracy of the measurement system in case of normal operation; furthermore the characterization has been made up to 120V.
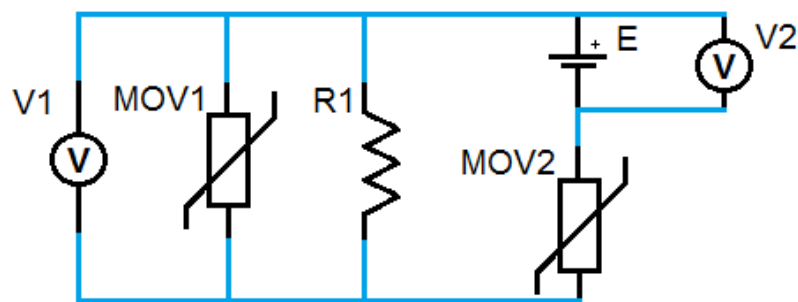
A sketch of the test layout is shown in Figure 5.7.

Figure 5.7 MOV2 test circuit in the whole measurement system.

The power supply E feeds the circuit, then the current is expected to flow in the R1 branch of the circuit in Figure 5.7 until MOV2 begins to conduct since the loop (MOV2-R1-E) represent a voltage divider where resistance of R1 parallel to MOV1 has a resistance smaller by several orders of magnitude compared to MOV2. Therefore the voltage drops almost entirely on MOV2 and MOV1 can be practically considered as an open circuit and hence R1 in series with MOV2.

The voltage on MOV2 is calculated as the difference V2-V1; then the current on the resistor is calculated by the ratio of V1 to R1.

As long as the voltage V1 is of the order of magnitude of mV, current on R1 can be considered the same on the series varistors (MOV2) as shown in the first test where no leakage current was measured for MOV1.

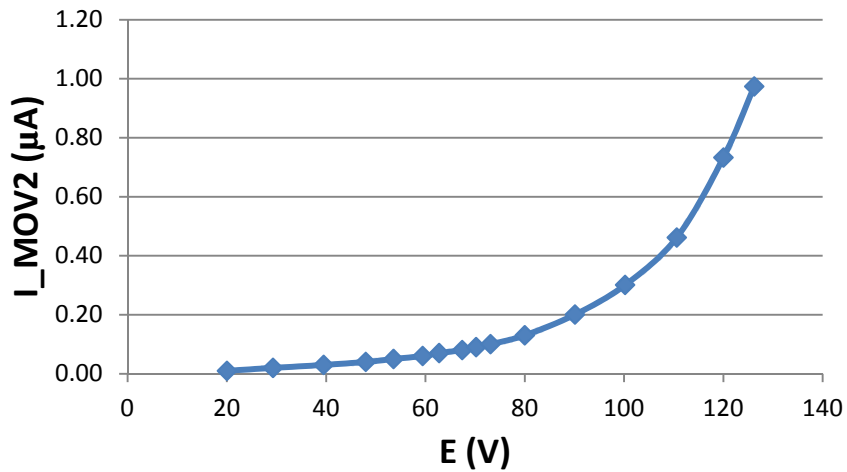The measured MOV2 characteristic is shown in Figure 5.8.

Figure 5.8 MOV2 V-I characteristic.

Finally it can be concluded that the leakage current is very low even at 120V, and for 50V the value is about 0.05µA then the previous hypotheses (current on R1 equal to MOV2 current) are well verified since the maximum voltage (V1) on MOV1 was 10mV and therefore MOV1 does not conduct as already shown in Figure 5.6.

The system was realized and installed on NIO1 by placing the series varistors as close as possible to the vessel providing the shortest path to ground in order to ensure the maximum safety and a small inductance; then all the other components were placed at the bottom of the vessel due to space constraints and twisted-pair connection was used in order to minimize noise pick-up.
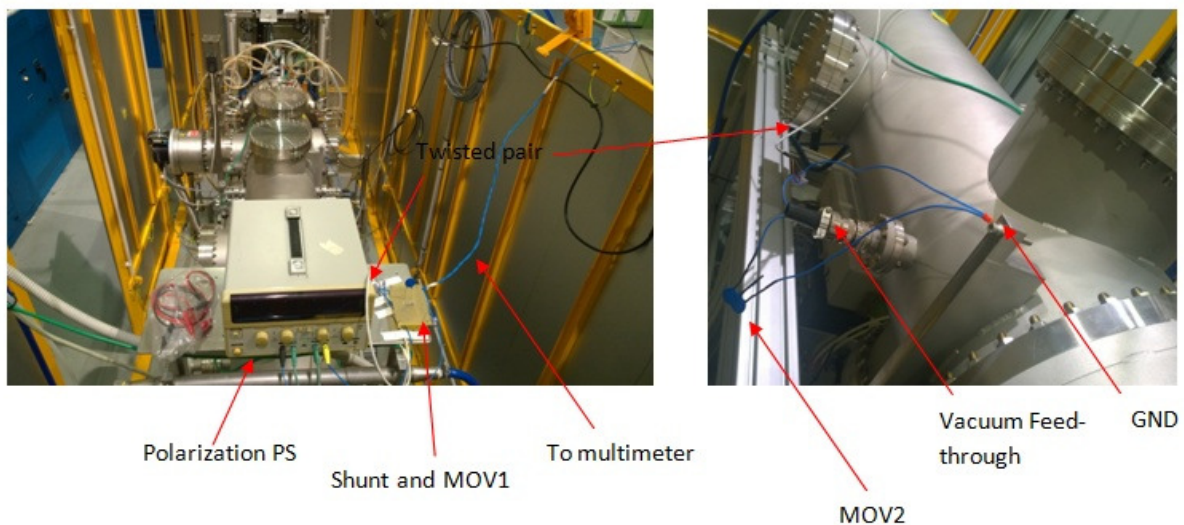
Pictures of the system are shown in Figure 5.9.Figure 5.9

Figure 5.9 Mini-STRIKE shunt installation on NIO1.

The bias effect to reduce secondary emissions was tested during operations described in next chapter. Two experimental results are reported herein for currents different by one order of magnitude [Figure 5.10]; during these tests overall conditions (pressure, RF power, HV power supplies and filters) are kept constant while the tile was biased from 10V to the maximum voltage available on the polarization power supply of 63V.
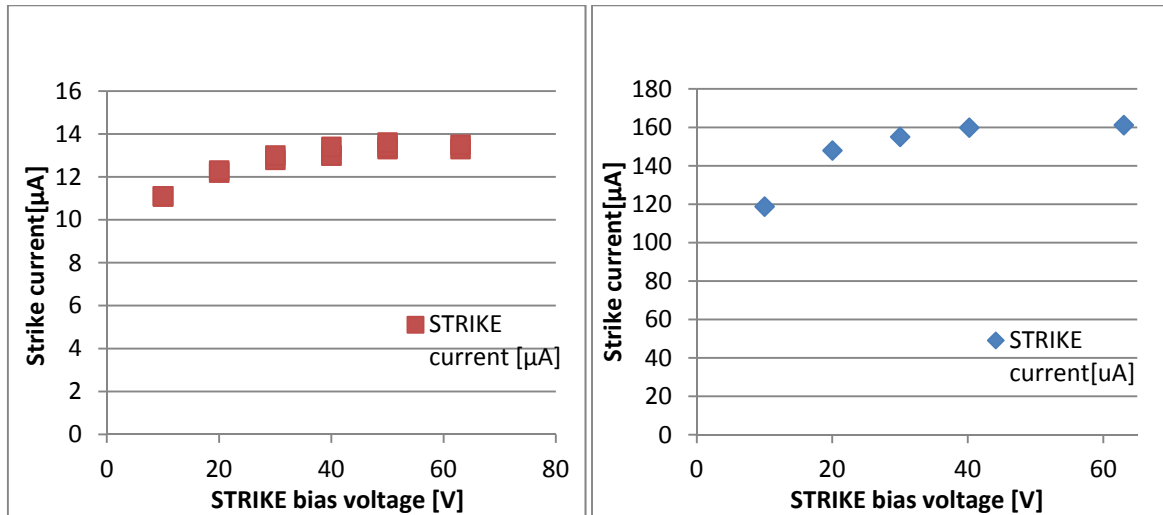

Figure 5.10 Mini-STRIKE current vs bias voltage for two orders of magnitude.

The previous graphs show that there is saturation for a polarization voltage above about 40V; therefore the power supply is adequate to collect secondary emission electrons.

This diagnostic will be very useful for data analysis provided in Chapter 6; moreover this preliminary system proved the feasibility of this measure as it will be shown in the next chapter where the measured current will be compared to the one estimation from calorimetry; for this reason it was decided to develop a new system like this but more sophisticated.

The new circuit will be made on a printed circuit board (PCB) where all components will be integrated, the reading will be automated and integrated in the NIO1 acquisition system and performed by a miniaturized PC (RASPBERRY) integrated on the board.

5.2 PA shunt

Another useful measurement regards the current on the Post Acceleration grid, which is due to net charges (electrons and ions) impinging on the PA grid.

Main issue as regards installation on NIO1 of any system to read the current on PA is due to the fact that Post Acceleration grid was poorly insulated from NIO1 vessel, hence the impinging charges can flow to ground through several undesired ground connections, located around the fastening of the PA cooling circuit.

For this reason a thin layer of Mylar was inserted at each contact point between the PA flange and the vessel [Figure 5.11]; in this way a single connection from PA to ground can be realized in which all the charges will flow.

The measurement circuit was realized and placed on the grid itself and it is composed of a shunt resistor of 13kΩ in parallel with a capacitor of (2.2µF) that provides to filter the high frequency noise due to the RF coil; a MOV (60V) has been inserted between the PA flange and ground in order to avoid dangerous overvoltages for example in case of EG-PA breakdowns.
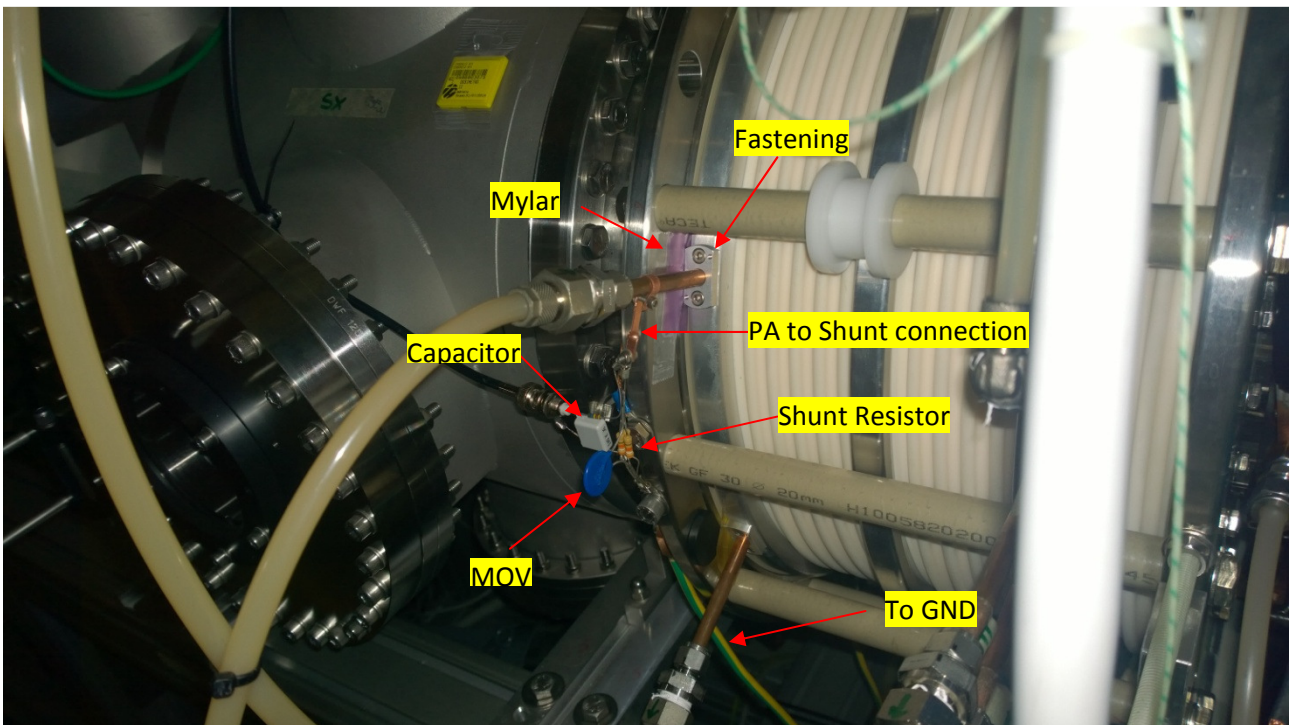

Figure 5.11 Post Acceleration Grid current measurement system.

6 Plasma operations

In this chapter some experimental results for 3 different types of filling gasses (Hydrogen, Air and Oxygen) will be presented; furthermore the HV passive protection circuit and fast interlock board have been tested and monitored in order to verify the overall behavior during normal operations involving real arcs between the grids unlike the artificially induced arcs as described in the previous chapter.

Special focus is placed on the topology of breakdowns for each gas type in order to understand which parameters are involved in electric discharges inside electrostatic accelerators and the real needs about the apparatus protection.

In this experimental campaign also acceleration was performed for the first time in NIO1, hence some useful diagnostics of the beam, like the PA shunt and Mini-STRIKE current measurement circuit described in the previous chapters, were subsequently installed as a consequence of the new requirements about beam characterization.

6.1 Electrical breakdowns

In order to understand the phenomenon of electrostatic discharges at low pressures between two electrodes a brief description of the physical process is done as follows.

The breakdown voltage V_b is a function of the product of the pressure **p** and the distance **d** between the two electrodes as shown in the following equation derived from Friedrich Paschen in 1889 [1]:

$$V_b = \frac{Bpd}{\ln \dfrac{Apd}{\ln \left(\frac{1}{\gamma}\right)}} \qquad (6.1)$$

where **A,B** and **γ** are constants and they are discussed below.

To understand the discharge dynamics a vacuum chamber is considered in which breakdown has not yet occurred; in this chamber there are always some free electrons due to gas ionization, for example thanks to cosmic rays.

If a voltage is applied between the two electrodes, the free electrons are accelerated towards the anode (electrode with higher potential), during this path they may collide with neutral atoms ionizing them. Afterwards the positive ions so created are driven to the cathode, because of the electric field, where there is a finite probability that secondary electrons will be emitted as a function of the secondary emission coefficient γ.

Then secondary electrons are accelerated towards the anode and may in turn create other ions. If the secondary electrons created produce enough ions to extract other electrons from the cathode the discharge is self-sustained and a breakdown occurs.

A graph of equation 6.1 for different types of gasses as a function of the pd product is shown in Fig.6.1
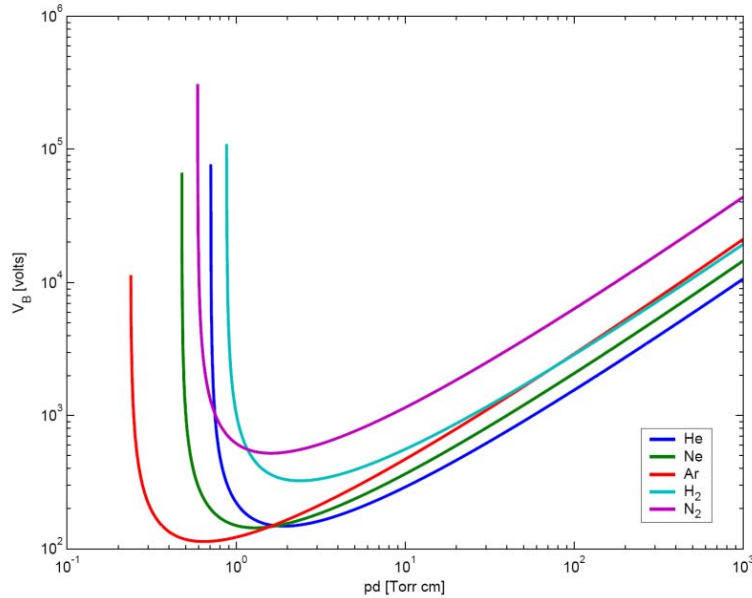

Fig 6.1 Paschen curves for some different gas types.

On the left side with respect to the minimum the breakdown voltage increases both decreasing the pressure or the distance between electrodes, thus even if many electrons are generated on the cathode the probability that they impact with a neutral during their path to the anode is very low; therefore increasing the distance or the neutral density (proportional to the pressure) the ionization probability increases up to a minimum.

As regards the right side, increasing **pd** means that collisions may be too frequent, hence electrons cannot acquire enough energy from the electric field because of their shorter mean free path in which the charges are accelerated. Therefore the voltage has to be increased in order to provide enough energy for ionization.

Then, solving the minimum with respect to **pd** the minimum breakdown voltage and its relative pressure can be obtained as shown in Eq.6.2 and Eq.6.3

$$(V_b)_{min} = \frac{\exp(1)\,B\ln(\frac{1}{\gamma})}{A} \qquad (6.2)$$

$$(pd)_{min} = \frac{\exp(1)\,\ln(\frac{1}{\gamma})}{A} \qquad (6.3)$$

In breakdown process, 3 parameters are involved and they are the electron-neutral collisional cross section σ_n, the ionization potential V_i and the secondary emission coefficient γ.
The first two are included in the gas constants A and B according to following equations:

$$A = \frac{\sigma_n}{kT_n}$$

$$B = AV_i$$

where T_n and k are respectively the neutral temperature and the Boltzmann constant.
All the previous coefficients depend on the filling gas, and γ slightly depends also on the material of the cathode and this theory so called (Townsend theory) can be applied up to 300 kPa·mm, for higher pd products streamer theory has to be considered. [2]

In NIO1 some complications with respect the simple model with 2 parallel plates at fixed pressure are present:

- three electrodes are present (PG,EG,PA)
- electrodes are not parallel plates [Figure 6.2]
- there is a plasma source at the cathode
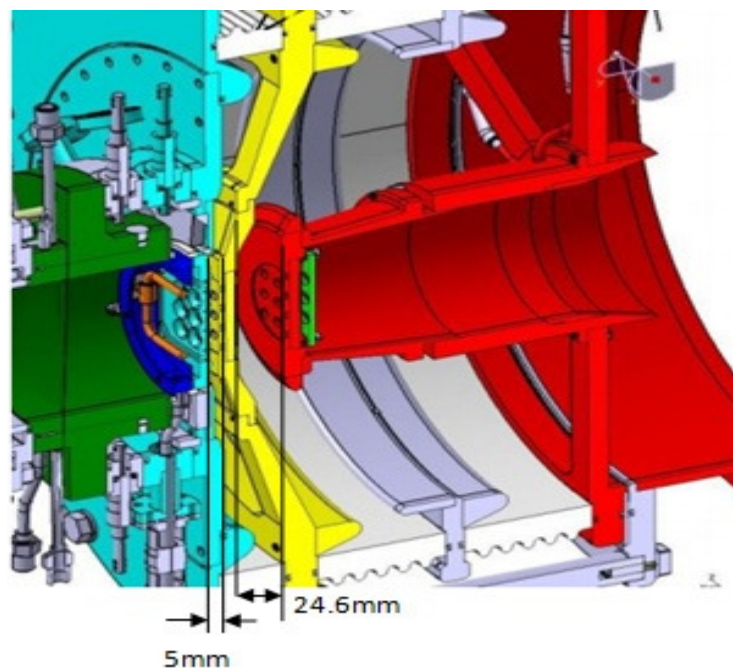- there is a pressure gradient between the grids

Figure 6.2 Cut section of NIO1 grids light blue (PG), yellow (EG), red (PA).

The experimental diagnostic consists in two oscilloscopes (Yokogawa 1646A) placed respectively on the HVD and outside of the NIO1 box.

The first one has the ground reference on the HVD and the four channels were connected as follows:

- CH1:current probe (current transformer with a sensitivity of 10A/V or 20A/V) placed around the positive cable of the EGPS
- CH2:voltage probe (transformer ratio 1000:1) connected between the HVD and Ground
- CH3:AGPS Rogowski coil
- CH4: EGPS Rogowski coil

A current clamp (Tektronik TCP303) is placed around the AGPS cable and its signal is amplified by an adjustable gain amplifier which for the experiment was set to 5A/V; then the signal is acquired from the external oscilloscope.

As regards the pressure measurement it would be desirable to know the pressure inside the acceleration column since the discharges are expected to be there. Unfortunately no pressure meters can be placed in that zone; however the pressure in the source can be computed from simulations Figure 6.3.
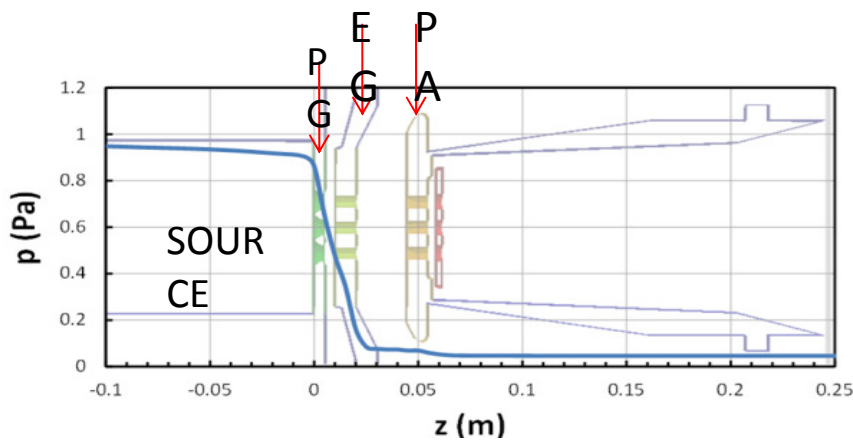

Figure 6.3 Simulation of pressure profile along the accelerator for air.

In our case the dual mode Pirani-Ionizing gauge, placed in the diagnostic chamber was used though a Pirani gauge was present in the source. This is due to the fact that during high voltage operations the source is biased and the gauge cannot be directly connected by an Ethernet cable to its acquisition system which is grounded at the electric grid potential.

Therefore in order to have the pressure value in the source a conversion of the vessel pressure has to be done depending on the gas type from calibration curves which links the vessel pressure with the source pressure and that are experimentally obtained.

It should be said that one of the upgrades of the NIO1 diagnostics has been the improvement of the pressure measurement system in the source since it has been connected to the DAQ

which is referred to the HVD potential like the source but this was performed towards the end of the breakdowns campaign.

Also it must to be pointed out that a lot of breakdown information was collected during normal extraction and acceleration operations, therefore a lot of points around some specific values of pressure corresponding the most suitable pressures for plasma generation were collected.

First operations with plasma started with hydrogen and since it was the first time that NIO1 restarted to operate in plasma after the vacuum leak, it was chosen to perform the conditioning of the extraction gap (space between PG and EG) in order to improve the voltage holding of the machine and to test the components without the further complication represented by the acceleration circuit.

 For this campaign the HVD was grounded and the AGPS disconnected like in the first set of measurement with the spark-gap [fig. 3.17]

With this configuration the Extraction Grid is biased both with respect to the Plasma Grid and the Post Acceleration grid which are at the ground potential; therefore the discharge can involve either the first or the second gap.

During these operations some breakdowns appeared and the results are shown in Figure 6.4 where the green markers are related to breakdowns with particle extraction, the x axis shows the vessel pressure and on the y axes the voltage applied from the EGPS when breakdown occurred is reported.

The pressure in the source for hydrogen is double with respect to the one in the vessel, and for the analysis the pressure between EG and PA has been assumed the same as the vessel pressure and that between PG-EG equal to the source pressure.
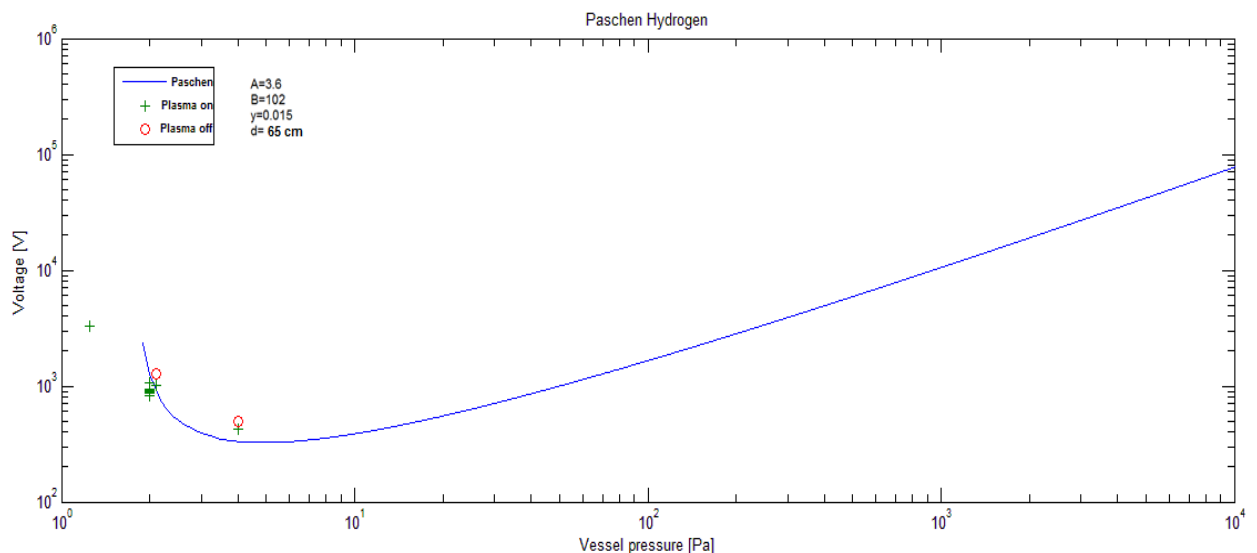

Figure 6.4 First breakdowns in hydrogen with and without plasma during extraction campaign.

First experimental result was that upon decreasing the pressure the voltage holding capability of the machine increases, therefore the experimental conditions are at the left of the minimum of the Paschen law.

Since the Paschen curves are obtained with no pre-existing charged particles in the electrode gap, in order to evaluate if the discharges during the extraction campaign were affected by charges some measurements were taken without plasma generation in the source (red points in Figure 6.4).

Experimental result was that the plasma generation only slightly decreases the voltage holding capability in the condition in which the maximum RF power was 250W; thus it can be assumed that Paschen law is still applicable.

Then the hydrogen Paschen curves was plotted (Figure 6.4) for various distances d in order to find the breakdown distance value most compatible with the experimental results and the most suitable curve obtained is shown in Figure 6.4.

It comes out that a distance of about 65cm between the electrodes is needed, thus since the distance between the grids is 5mm for PG-EG gap and 24.6mm for EG-PA gap [Figure 6.2] the discharge does not involve the minimum distance between the grids but rather other longer paths involving the metallic support of the grids itself for example.

Another consideration was that in the PG-EG gap, even with a big deflection of the generated electrons, a path of 65cm is not available; therefore a discharge between EG and PA is more likely.

Also the non ideality in the electrodes geometry is expected to reduce the real distance in the discharge, in fact in some points the electric field can be more intense than in planar geometry model and therefore a discharges may occur along shorter distances compared to the theoretically values.

Afterwards other data were collected also during the acceleration campaigns in which the circuit layout is that one in fig 3.21.

With this setup a good way to investigate the discharge evolution is theoretically simple since on both high voltage power supplies a current probe is placed; therefore if a breakdown occurs in the first gap, the EGPS current probe will show an over-current; the same applies to the other power supply.

Nevertheless during experimentation many spurious cases as regard the breakdown detection occurred:

- FPU detects an event and the oscilloscopes are not triggered; in this case it cannot be said if the event was a real arc or just a current spike or noise.
- FPU detects an event, only the oscilloscope on the HVD is triggered and no current is detected on the EGPS current probe; in this case if the voltage probe shows a fast voltage decrement it is assumed that a real arc is present between EG-PA [Figure 6.5]
- The internal over-current detector of the power supply detects an arc; in this case it is assumed that a real arc is present in the gap related to the power supply that detected the arc.
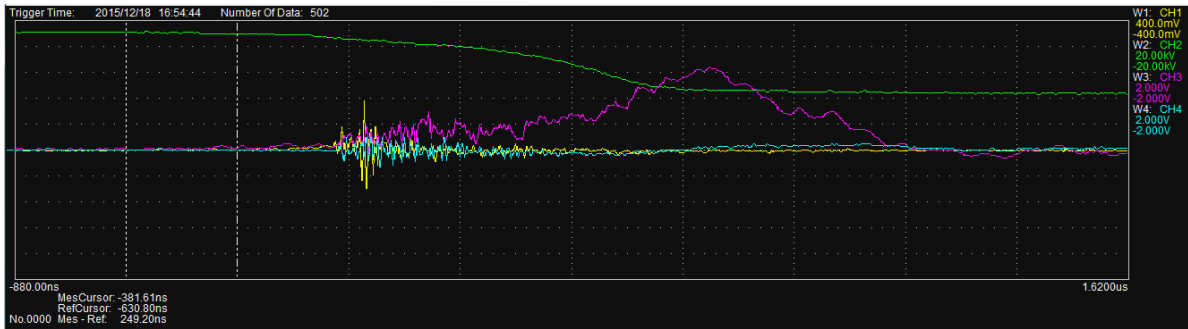
Figure 6.5 Typical waveform corresponding to an EG-PA arc sown by the HVD oscilloscope.

The graph in Figure 6.5 was collected by the HVD oscilloscope with a source pressure of 0.6Pa, AGPS at 18kV and EGPS at 5kV; the MOV effect on the green line (CH2) and the AGPS Rogowski voltage (CH3) can be clearly observed. Furthermore the oscillatory behavior of the current probe (CH1) probably is a disturbance since the EGPS typical discharge is different as seen in 3.3.

For hydrogen, unfortunately, just a few discharges was identified since the first spurious case was dominant, for this reason two charts, shown in Fig. 6.6 have been derived taking into account all the breakdowns detected with respect the PG-EG and the EG-PA gap voltages and the pressure in the source.
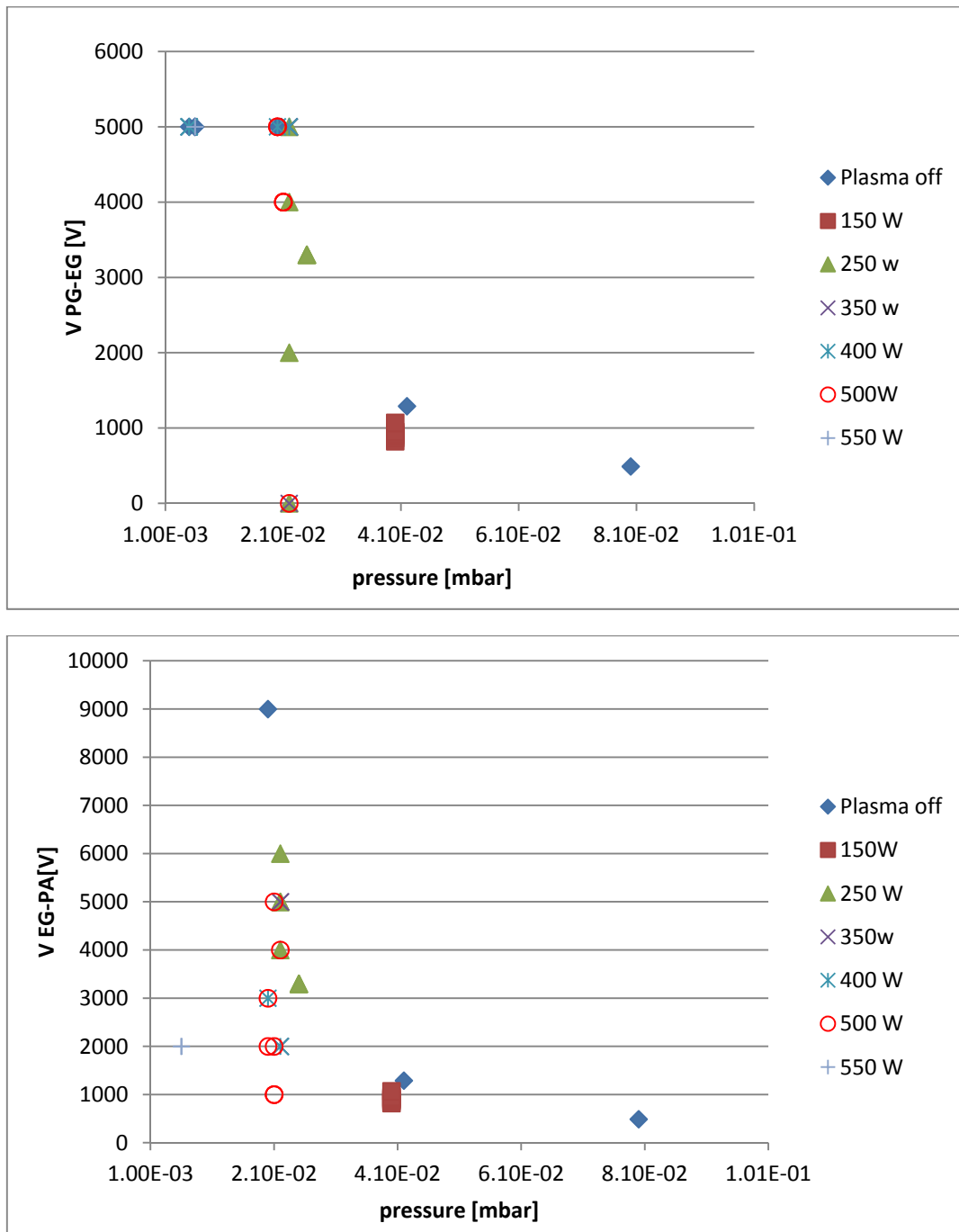
Figure 6.6 Breakdown voltages in the first gap (upper) and second gap (lower) collected in hydrogen with respect source pressure and radiofrequency power.

The charts in figure 6.7 show two important aspects related to the voltage holding of the accelerator. At first a general trend relating pressure and voltage holding on the gap is clear, in particular the gap maximum voltage holding increases by decreasing the operating pressure in the source. Furthermore operations without plasma exhibit higher withstanding voltage on the gaps in comparison with plasma operations.

Another interesting result discovered in hydrogen operations is a particular condition in which the discharge shows an evolutive behavior [Figure 6.7] in fact it has been seen that a breakdown can start from PG to EG and then generate another arc between EG and PA.

This behavior is explainable as follows: since electric arcs are sustained with very low voltage compared to that one between PG-EG before the discharge, the potential of the Extraction Grid becomes about that one on the Plasma Grid (AGPS voltage), therefore the voltage on the second gap increase from AGPS-EGPS voltages to about that one of AGPS, thus if this voltage is greater than the withstand voltage of the EG-PA gap another arc will start. Furthermore the first arc generates many free charges in the acceleration column, and some of them may be accelerated in the second gap further reducing the voltage holding by helping the trigger of the second arc.
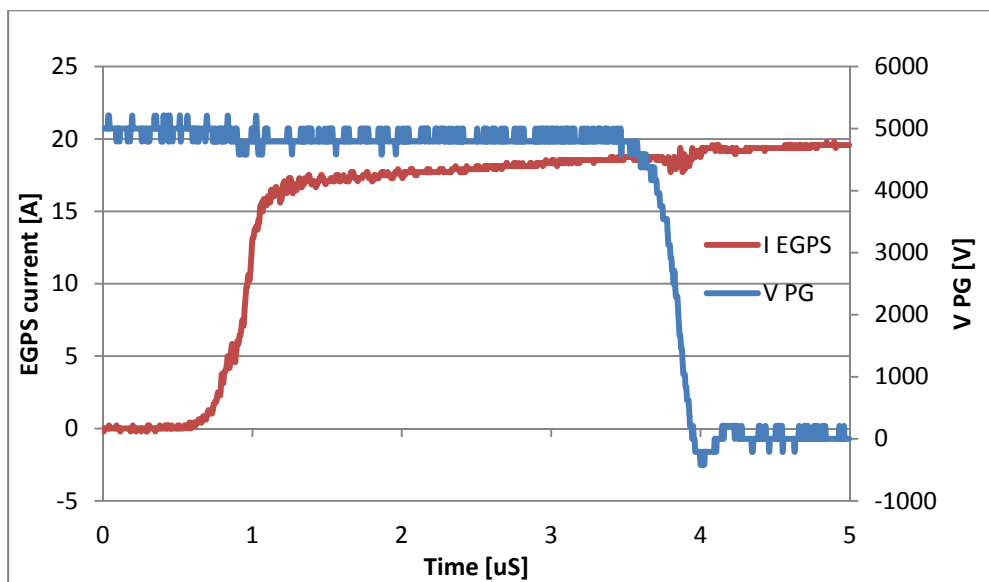

Figure 6.7 Typical behavior of an evolutive discharge from PG-EG to EG-PA.

In the previous graph (Figure 6.7) an evolutive arc is shown: the EGPS arc (red line) and the HVD potential with respect to ground (blue line) that initially remains unmodified for about 3 micro seconds from the beginning of the EGPS breakdown, then it collapses to zero in less than one microsecond because of the second arc (EG-PA) shown in Figure 6.8 upper; a zoom view of the fast phase of the AGPS current is shown in Figure 6.8 lower, where it can be observed that the arc evolves in the order of microseconds.
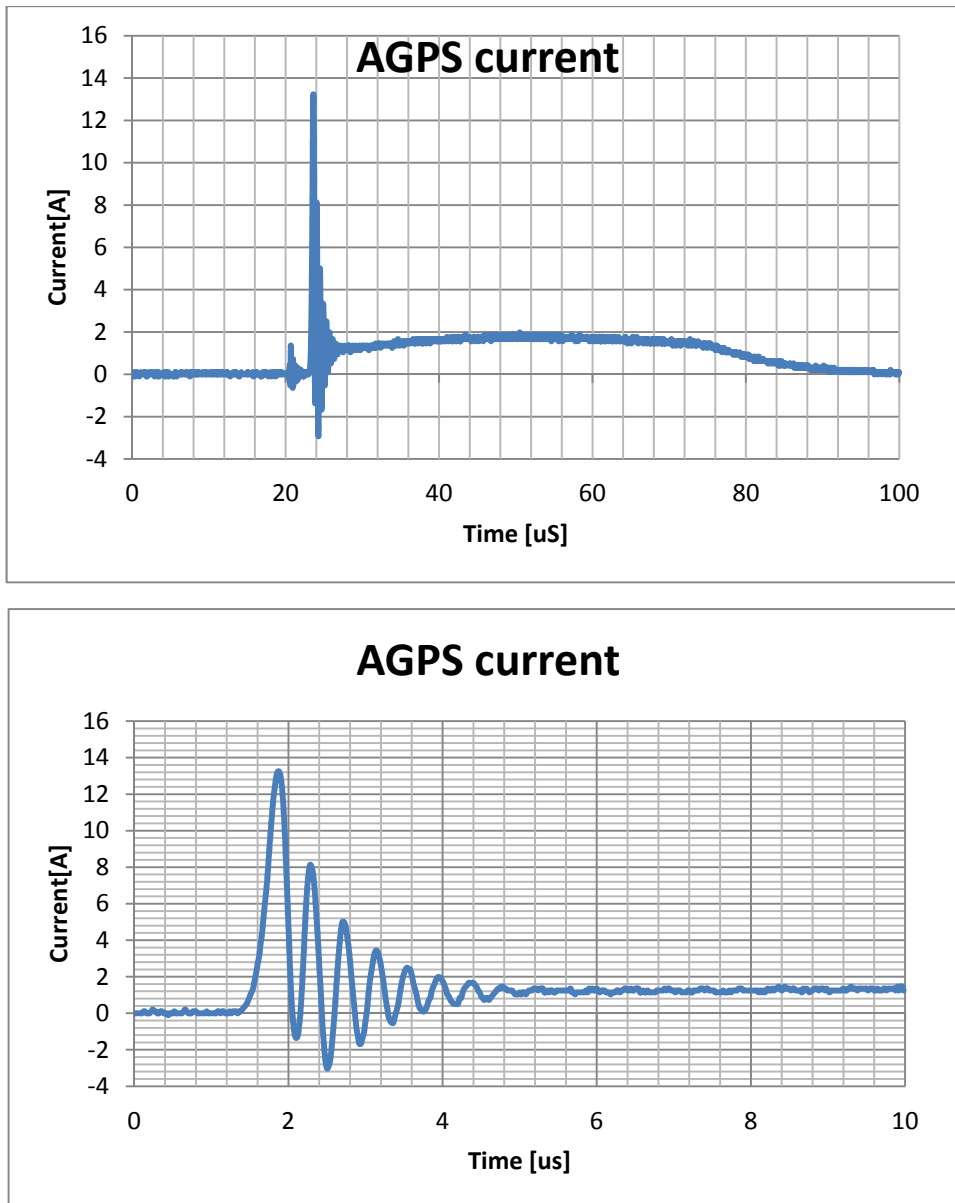
Figure 6.8 AGPS discharge due to the EGPS arc shown in Figure 6.7. The bottom plot is a time zoom of the highest peak in the upper one.

These graphs were collected from both the oscilloscopes in hydrogen with an RF power of 500W, 2.2mbar in the source, 5kV and 4kV respectively for AGPS and EGPS.

This fact drives an important consideration, if the FPU and the AGPS were fast enough to disable the output voltage once Rogowski on the EGPS cable trigger the first arc, the second arc could be avoided.

AIR

As regards the air campaign the behavior of the arc detection was different, in this case a lot of arcs were collected and identified unlike hydrogen campaign; in fact it was possible to

trigger many discharges from the HVD oscilloscope and for those ones not triggered the identification was performed by the internal detector of the power supplies.

In the air case the read pressure in the vessel had not to be corrected since the gauge is calibrated for air, furthermore the conductance for the air is lower than for hydrogen since the size of the particles (mainly N_2 and O_2) is greater; in this case the pressure in the source is about 20 times higher than that in the vessel.

In this case it was observed that mainly the discharges were between PG-EG, therefore data analysis was done in order to identify which parameters affect the breakdown voltage.

At first it was verified that the effect of the Bias Plate and the Plasma Grid Filter was negligible, since for fixed conditions (RF, EGPS, AGPS and pressure) the breakdown voltage was about the same.

For this reason the analysis was made in the first gap at different pressure with variable radiofrequency power as shown in Fig.6.9
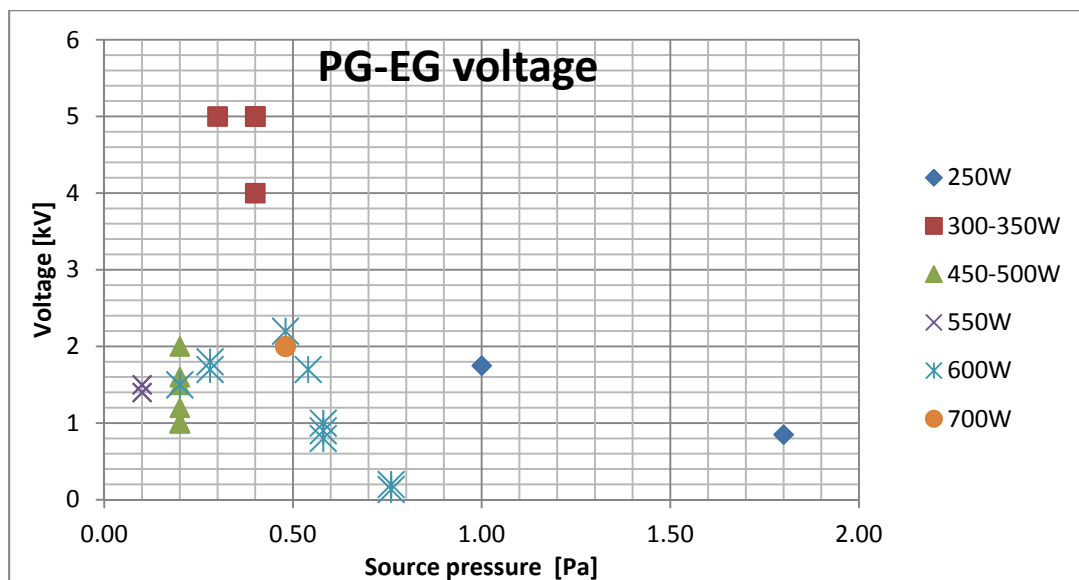

Figure 6.9 Voltage holding for AIR at different RF power.

The chart highlights a clear trend for RF powers up to 350W in the expected direction since the breakdown voltage increases as pressure decreases, the same behavior can be noted for 600W up to 0.5Pa and no points with RF over 350W can hold a voltage higher than points with lower powers for pressures below 1 Pa, therefore a clear effect of the radiofrequency power in the voltage capability was found.

An interesting result is represented by two singular cases:

- with no plasma the breakdown voltage fulfilled the full capability of NIO1 (5kV on the EGPS and 20kV on the AGPS) in the present reduced operative range with a pressure in the source of 0.2Pa.

- without plasma and for a pressure in the source of 0.47 Pa the discharge involved the second gap in contrast with all the cases collected until then since they were in the first one; furthermore the arc shows an evolutive behavior opposite with respect to that in hydrogen shown above (Figure 6.7).

As regards the first case above-cited, the influence of plasma on the breakdown voltage for the air case is clear since that the full voltage capability has never been obtained for these values of pressure.

Also the second case is very meaningful where the discharge behavior is reported in Figure 6.10 and it can be explained as follows: at first an arc involved the path between EG and PA that was detected from the current probe on AGPS (third panel), an alignment of this current triggered from the external oscilloscope with the waveforms triggered by the internal one was possible since this current clearly causes a first lowering in the HVD potential up to the varistor clamping voltage of about 9kV. Then after a time of about 9 microseconds another arc involved also the gap between EG and PA and the current value is shown in the second panel (the waveform assumes negative values since the probe was inserted reversed, hence the current is correctly delivered by the power supply); the first panel shows also that in this phase the HVD potential goes down to zero since the varistors are short-circuited by the arc.
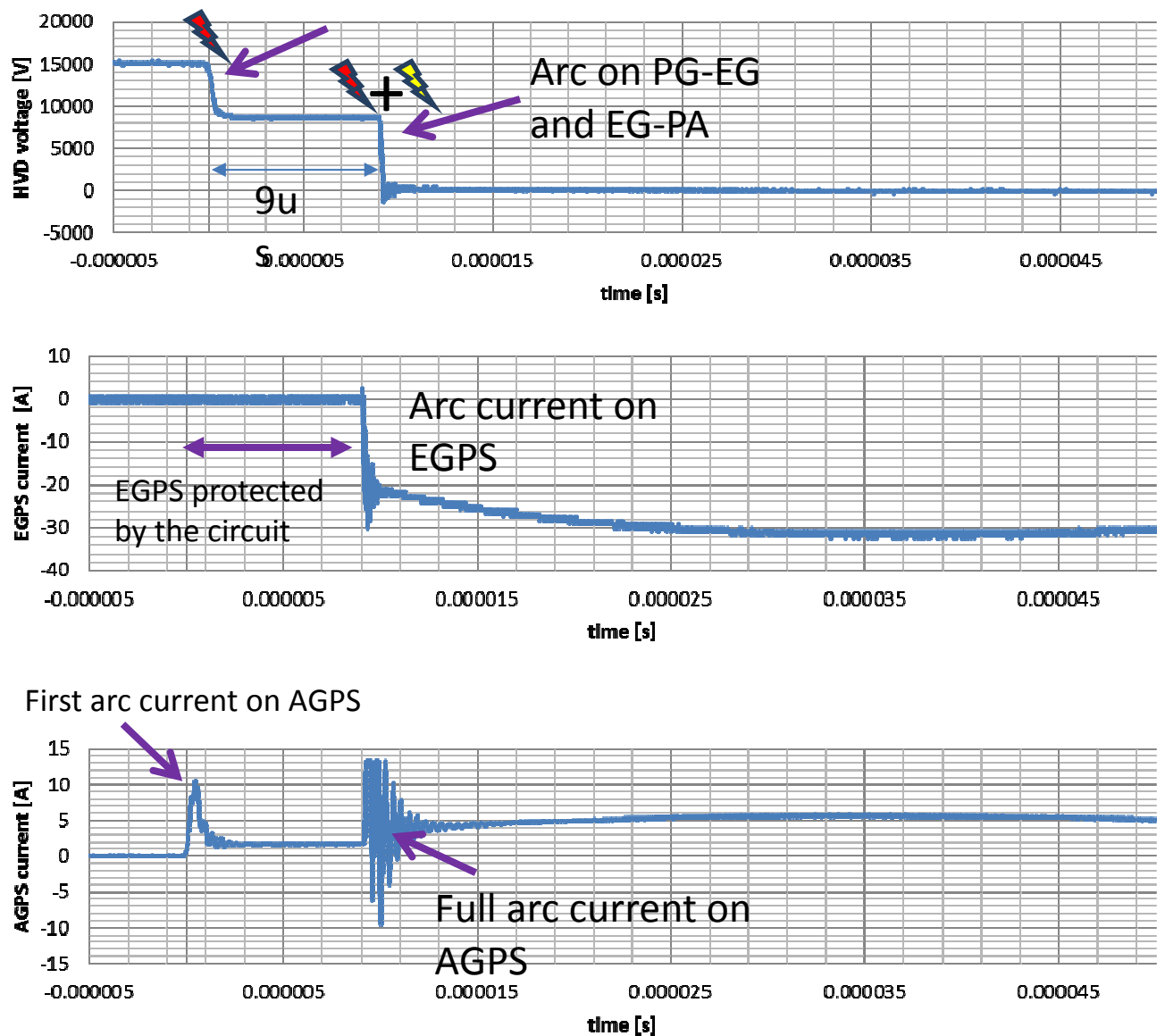
Figure 6.11 Evolutive arc started from EG-PA than evolved in to PG-EG-PA.

From this discharge it came out that the gap PG-EG is not able to sustain a voltage of 9kV (MOV clamping voltage) at this pressure, furthermore it can also be seen that EGPS is well protected by the varistors during the EG-PA arc since no current is forced to flow in the power supply.

Oxygen

In oxygen just a few breakdowns were collected during the thesis period, and all of them at the pressure of 1.6e-4mbar in the vessel (0.32Pa in the source) except one at the pressure of 2.4e-4mbar in the vessel.

For all cases the arc was detected in the EG-PA gap in contrast with air. A table with the voltage limits is shown in Tab.6.1 and the behavior is not clear at the moment because the limit is in the EGPS voltage at about 2kV, but the discharge is in the second gap, as derived by the absence of current measured by the EGPS current probe, where the voltage decreases along with the EGPS voltage increase.

RF power [W]	Vessel pressure[mbar]	VEGPS	VAGPS	Vgap2
600	1.60E-04	1	25	24
600	1.60E-04	2.3	23	20.7
600	2.40E-04	1.7	17	15.3
600	2.50E-04	2.1	21	18.9
600	1.60E-04	1.5	20	18.5
600	1.60E-04	1.6	20	18.4
600	1.60E-04	1.4	20	18.6
600	1.60E-04	1.2	20	18.8

Table 6.1 Breakdowns conditions in oxygen.

Another diagnostic was tested in this campaign: a differential voltage probe was inserted in the PG-EG gap in order to measure the voltage during the arc phase if an arc in the first gap was triggered. Fortunately, even if in oxygen this is fairly rare, at least an event occurred. Fig 6.12 shows the EGPS current (blue line) and the voltage of the first gap, the discharge was taken with a pressure in the vessel of 1.7e-3mbar and 1.5kV and 15kV for EGPS and AGPS respectively.
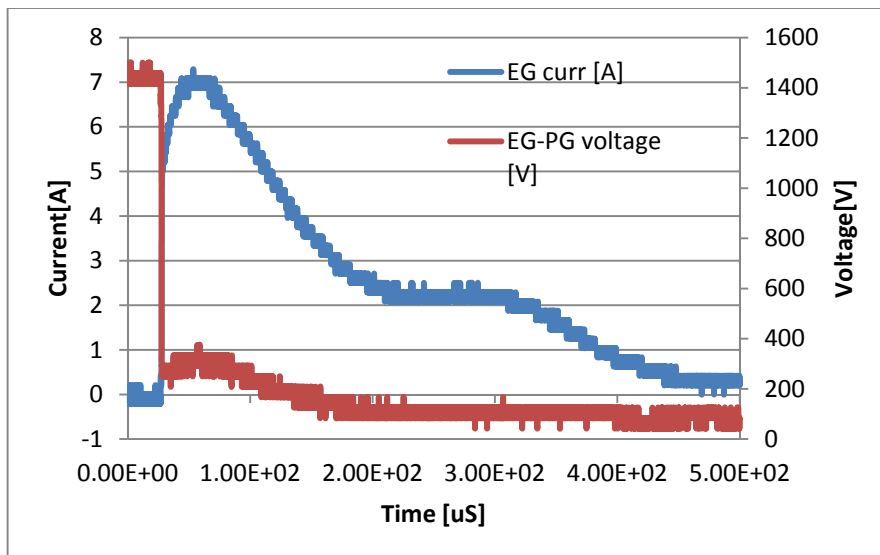

Figure 6.12 EG current (blue) and PG-EG voltage (red) during an arc at 1.7e-3mbar, VEGPS (1.5kV).

From the previous figure an important results can be obtained by multiplying voltage and current: the power of the arc which is deposited on the Extraction Grid as thermal power and therefore also the output power of the power supply. [Fig 6.13]
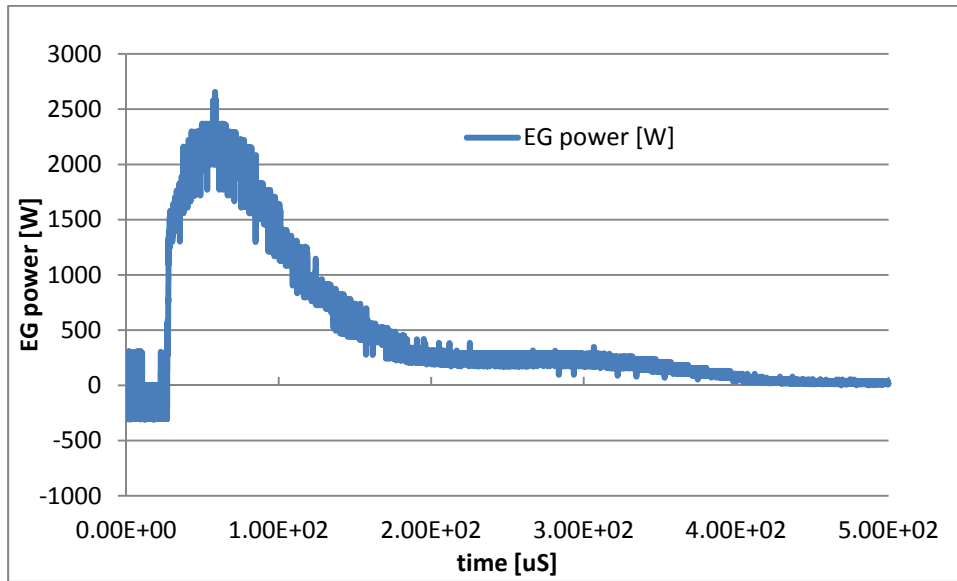
Figure 6.13 EGPS Arc power at 1.7e-3mbar, VEGPS (1.5kV).

In this case the maximum power is about 2500W, and surely the power on the Extraction Grid is less than the maximum expected during normal operations, since the EGPS can deliver a power up to 6kW (600mA at 10kV); nevertheless the area exposed to the arc is expected to be significantly smaller then the whole grid, therefore care has to be taken with respect to the surface damage due to arcs. Moreover the power waveform was integrated with the aim to obtain the total energy released by the arc, which was calculated as 240mJ; the arc resistance during the current peak results30Ω.

6.2 Extraction and acceleration

In this section some meaningful results for the NIO1 extraction and acceleration for different types of gases will be presented; it has to be recalled that during this thesis work acceleration was performed for the first time on NIO1 therefore the diagnostics described in the previous chapters have been designed, built and installed during this campaign.

Hydrogen

During this campaign, at first the conditioning of the extraction gap was made in order to increase the voltage holding of NIO1 as already reported above when describing also the use of the EGPS; then after some days the full setup with also acceleration was employed.

Gradually the RF power and thus the plasma intensity was increased in order to test the Pyrex and to verify the proper operation of the diagnostics installed, for example PMT, Luximeter, thermocouples, Mini-STRIKE, the protection systems installed and described in Chapter 3 and finally OES and BES.

At first, the source was been analyzed: the most suitable value for the RFPS frequency was found at 2022MHz where the reflected power is minimum; then with that frequency value many attempts were done in order to achieve measurable extracted currents by varying the pressure, the voltages on the HV powers supplies and the filters (magnetic filter and bias of the PG).

As shown in Chap5, it was impossible to discriminate a real beam current using the AGPS display, thus the PA shunt idea was conceived.

As the amount of collected data was rapidly increasing, also a better way to manage data was developed: this system consists in reading all the measured values and all the settings (e.g. from the power supplies, the vessel pressure, the diagnostics) when the operator pushes a specific button on the NIO1 console [Fig 6.14] and save these parameters in a CSV file; furthermore for the diagnostics not yet connected to the control interface, like the PA-shunt (which is read from a multi-meter) and luximeter, the readings can be manually added to the CSV file by writing the values in a specific text box. This is very useful to study the beam because only the most significant data at stable conditions can be saved, and then the file can be managed with Microsoft Excel in order to obtain all the graphs shown below.
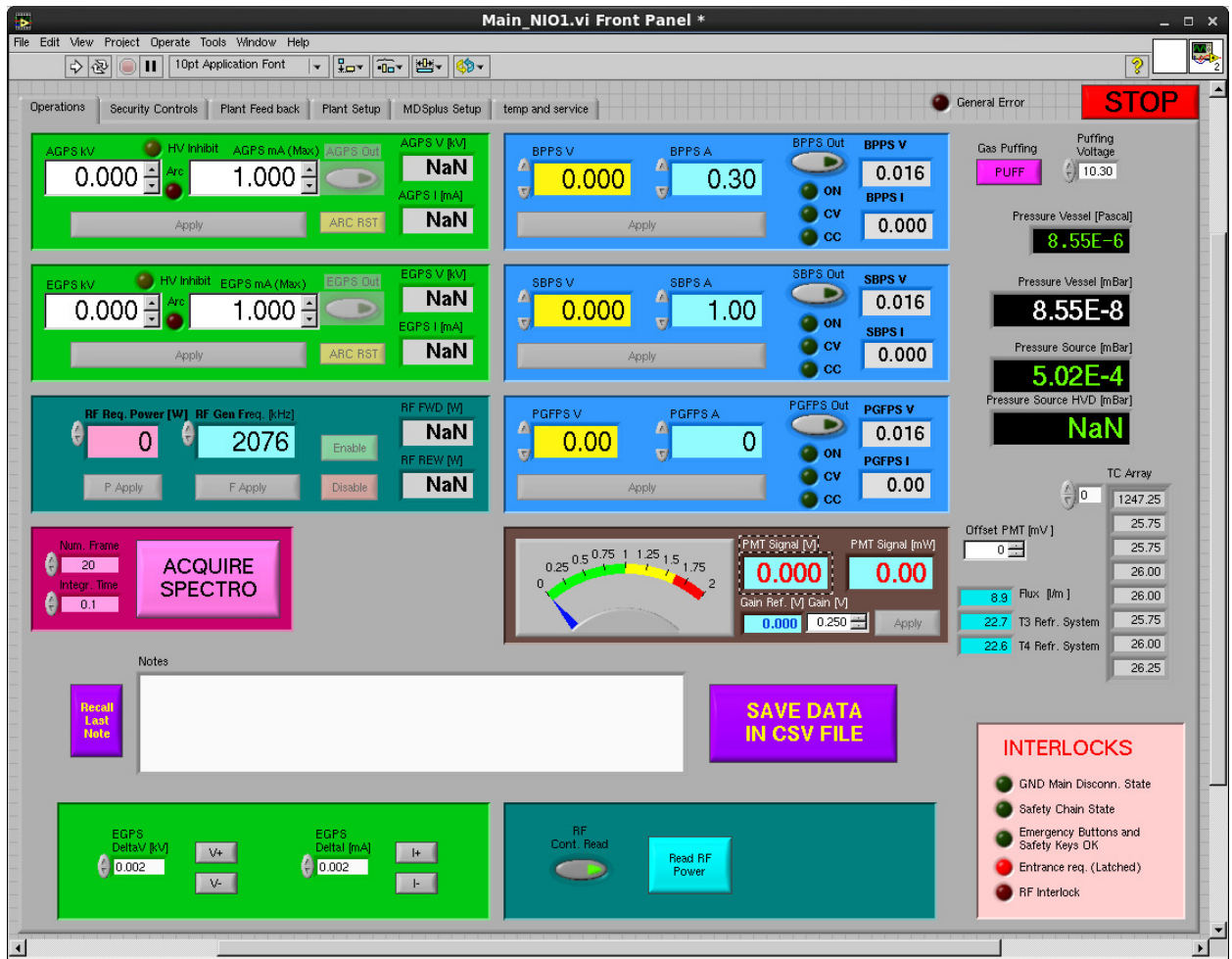
Figure 6.14 NIO1 control interface based on Labview.

With the aim to give the order of magnitude of currents in hydrogen, just some graphs will be presented here, in particular special focus will be placed on the extracted particles.

At first it can be observed that for the EGPS current [Fig 6.15], the display reading can be used in order to evaluate the extracted current: the leak current is 0.4mA per kV due to the EGPS leak resistance which was evaluated in about 2.5 MΩ.
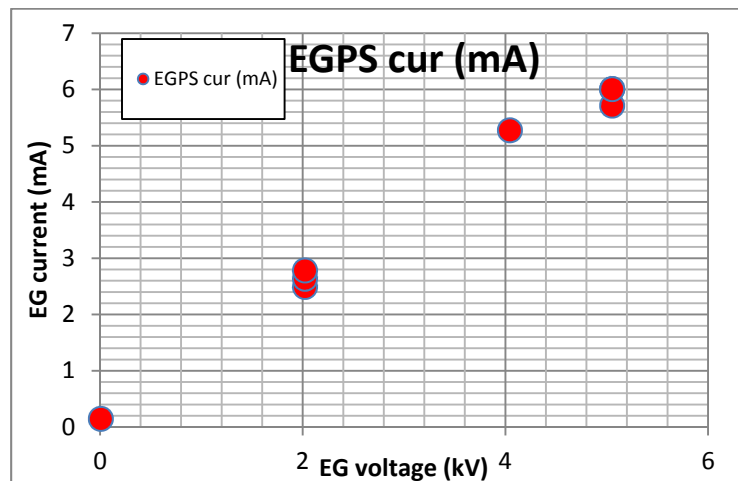

Figure 6.15 EGPS current at Press=5e-3, Power=500 W.

117

A first it can be observed that RF power, pressure and extraction voltage are the main parameters involved in the magnitude of the extracted current: for higher pressure, more current can be extracted even at lower RF power as shown in Fig. 6.16
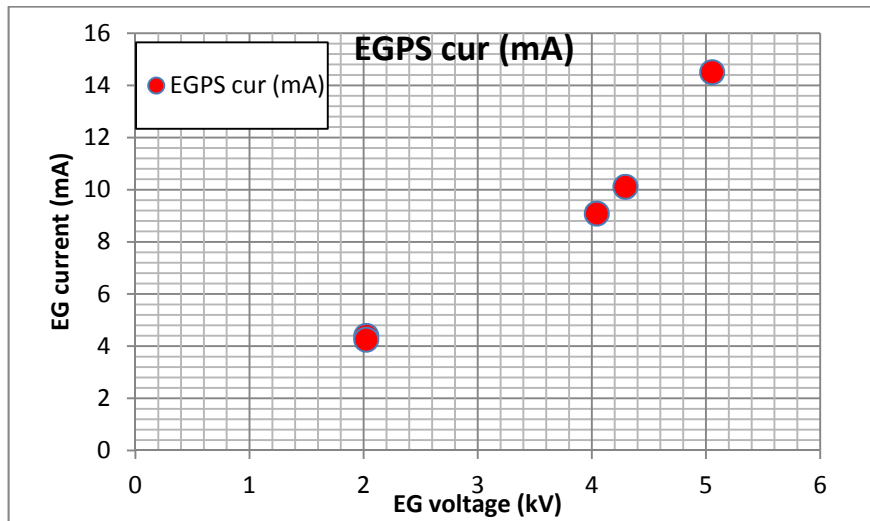

Figure 6.16 EGPS current at Press=2e-2, Power=350 W.

As regards the measurements performed by means of the PA shunt, consisting in particles that hit the PA grid, some voltage scans were made in order to evaluate the effect of extraction and acceleration voltages on the amount of particles impinging o the PA grid as shown in Fig. 6.17 where the maximum values in Hydrogen for the PA currents were achieved.
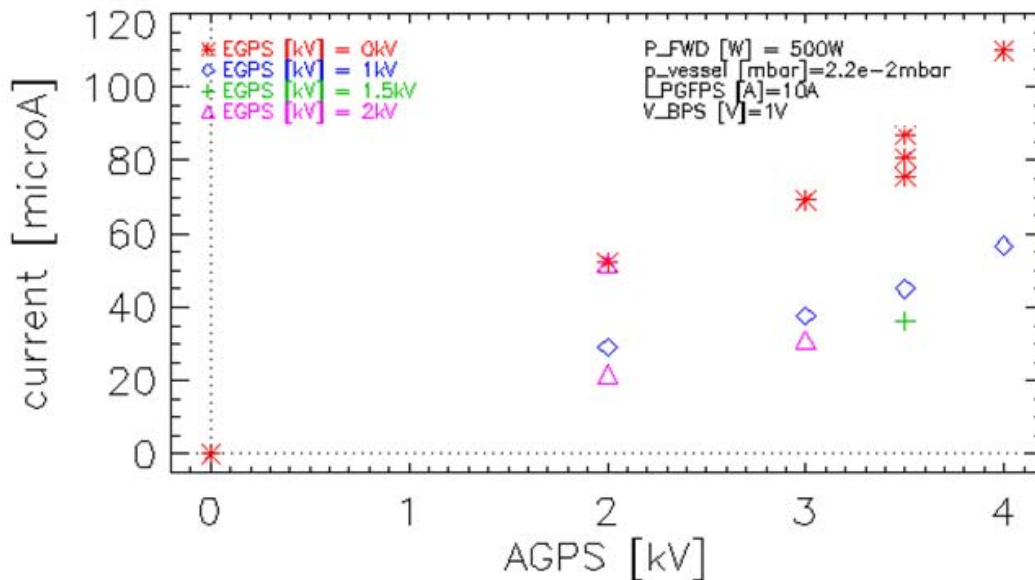

Figure 6.17 PA current at Press=2.2e-2 mbar, Power=350W.

Even with these current values, no heating on mini-STRIKE was detected; furthermore increasing the acceleration voltage at this pressure value in order to raise the beam particle energy, and thus the beam power, was not possible because of breakdowns problems.

In hydrogen currents probably were so weak for several reasons:

- No caesium has been injected in the source, since the oven is not yet installed, and hence negative ion production is performed by the volume channel only (low production rate) while surface production is expected to be negligible. It should be remembered that, as reported in Chapter one, surface production can enhance the H⁻ by a factor from 3 to 10, thus with no caesium the number of neative hydrogen ions is very small.

- Another reason is related to the limited radiofrequency power used (550W), since Pyrex had never been tested before: care was taken in RF power increasing and higher power will be used in the following campaign with Air and Oxygen.
  In order to understand the effect of the RF power on Hydrogen plasma generation a graph collected in the previous campaigns before the Alumina break is shown in Figure 6.20.
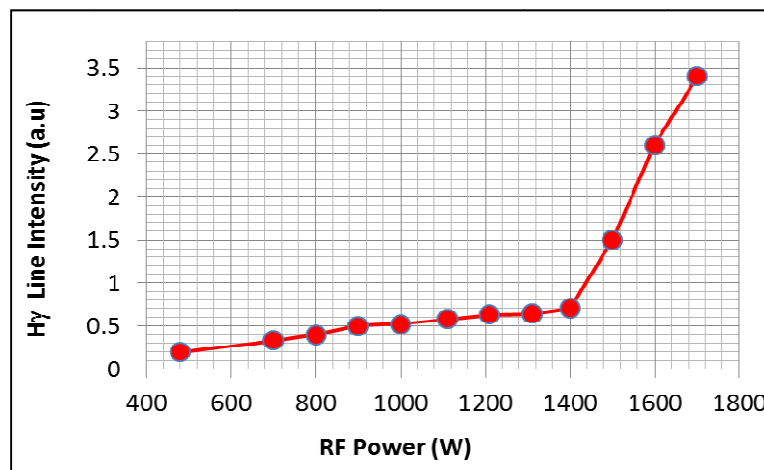

Figure 6.18 H$_\gamma$ intensity vs RF power.

The graph shows the amplitude of hydrogen H$_\gamma$ line with respect the RF forward power and collected by OES. It can be observed that the H$_\gamma$ amplitude strongly increases around 1400 W, where plasma coupling changes from capacitive (E-mode) to inductive (H-mode); in correspondence to this transition the production of negative ions is expected to be enhanced.

- Third cause is due to the deflection magnets located inside the Extraction Grid, which are slightly oversized as shown from accurate simulations made "*a posteriori*"; the field in the Extraction gap is shown in Fig. 6.19 where the y component of the field **B$_y$** (horizontal direction perpendicular to the beam direction Z) is shown and Z=0 is the Plasma Grid knife, therefore charges are deflected in the x direction by the Lorentz force with a circular trajectory characterized by the Larmor Radius **R$_L$** as shown Figure (right) where the proper operation is shown.

In this case also negative ions can be deflected by the magnets since hydrogen ions have smaller mass (1amu) than O⁻ (16amu) for example, as shown by the following formula which represents the Larmor radius[3]

$$R_L = \frac{mv}{qB}$$

where **m** is the ion mass, **v** is the perpendicular velocity with respect the magnetic field line **B** and **q** the elementary charge.
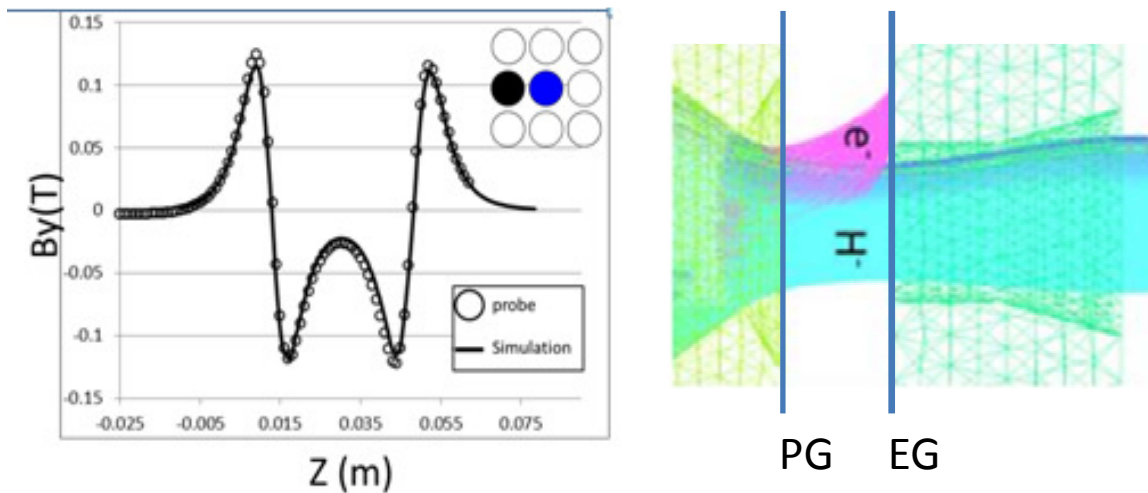

Figure 6.19 By field in the extraction region (left), effect of the magnets on the charge particles in proper operation (right) [4].

This means that the Larmor radius is too small also for hydrogen ions with respect to the distance between PG and EG, in this case also ions might be deflected against the side of the grid, where no holes are present, or towards the cylindrical part of the apertures in the EG, where they are lost from the beam.

In order to increase the Larmor radius it would be possible increase the extraction energy **E** that is proportional to the EG voltage **V**, in fact in this way since:

$$qV = E = \frac{1}{2}mv^2$$

the ion velocity along Z increases, nevertheless up to 5kV no substantial improvement in the extraction current have been observed.

AIR and OXYGEN

In order to achieve the H-mode with increased plasma density in the source and reduced ion deflection it was been chosen to change the filling gas as the simplest and fastest solution.

Even if SPIDER and MITICA will be based on hydrogen/deuterium, air and oxygen were chosen in order to improve the diagnosability of the beam and the knowledge in negative ion accelerators and to facilitate the data analysis techniques.

At first air was chosen with the aim to produce an inductively coupled plasma at lower RF power than hydrogen since in previous experimentations involving just the source characterization the transition was reported around 700W as shown in Fig. 6.20.

In an air plasma negative ions are mainly represented by O^- that are 16 times heavier than those of hydrogen, thus extracted ions can go through the Extraction Grid holes; furthermore as Oxygen has higher electron affinity than hydrogen (1.461eV vs 0.754eV [5]), free electrons are more easily collected by neutral Oxygen; therefore the ratio between O^- and electrons is expected to be higher and the absolute amount of negative ions is greater.
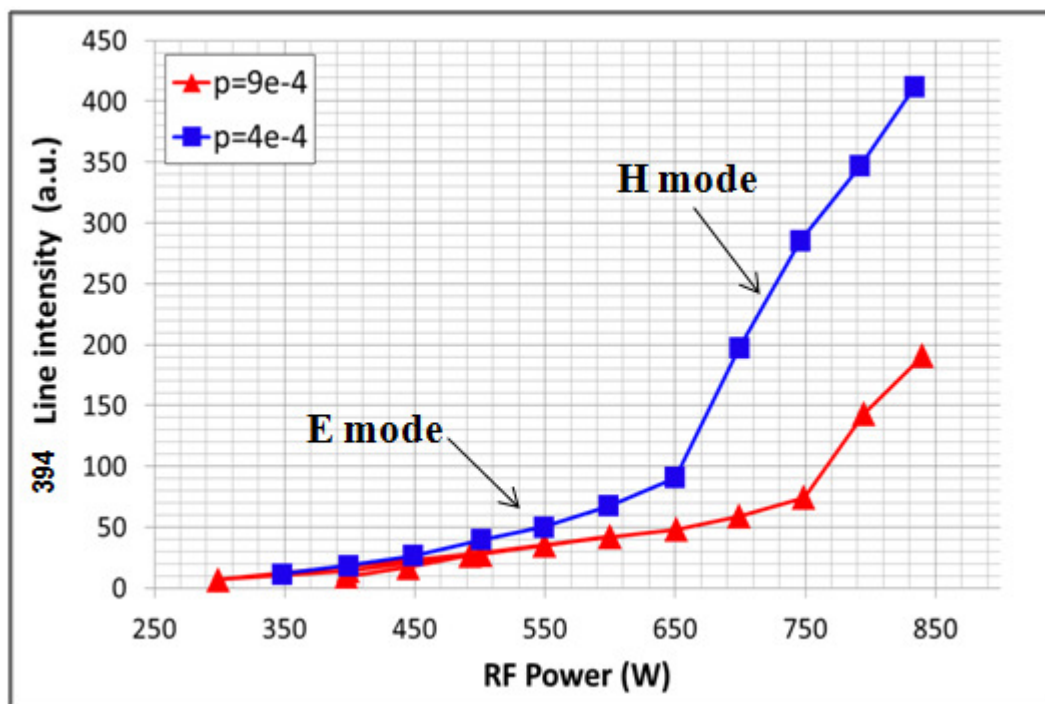

Figure 6.20 H-transition for Air for two different pressures.

During air operations for the first time increases in the temperature of the CFC tile have been observed; moreover the measurement system for the current collected on the tile entered operation and the PGF improvement was performed in the latter operation of the air campaign.

All these improvements have proven to be very useful to study the beam as reported here below.

In order to read correctly the graphs some indications are given:

- Current read from EGPS is assumed as an electron current; it represent all negative particles extracted from the source that hit the grid, and magnets deflect mainly

electrons; furthermore negative ions extracted are lower by orders of magnitude with respect to electrons therefore the amount of ions that hit the grid is negligible.

- Sum of currents collected on the PA grid and on Mini STRIKE is assumed to be the negative ion beam current since no electron leak is ensured by EG and PA magnets.

At the beginning some tests about the beam optics were performed just with the PA shunt since the current measurement system on the CFC tile was not already installed (and the tile was simply grounded); the current collected on the PA grid is expected to be proportional to the beam angle at the grid surface (divergence), hence for fixed values of EG voltage, a scan of the acceleration voltage was made; furthermore the ratio between electrons (EGPS current) and the portion of the beam accelerated and collected on the PA surface was evaluated Fig. 6.21 where the ratio has to be divided by 1000 since it has been calculated as a ratio of µA/mA.
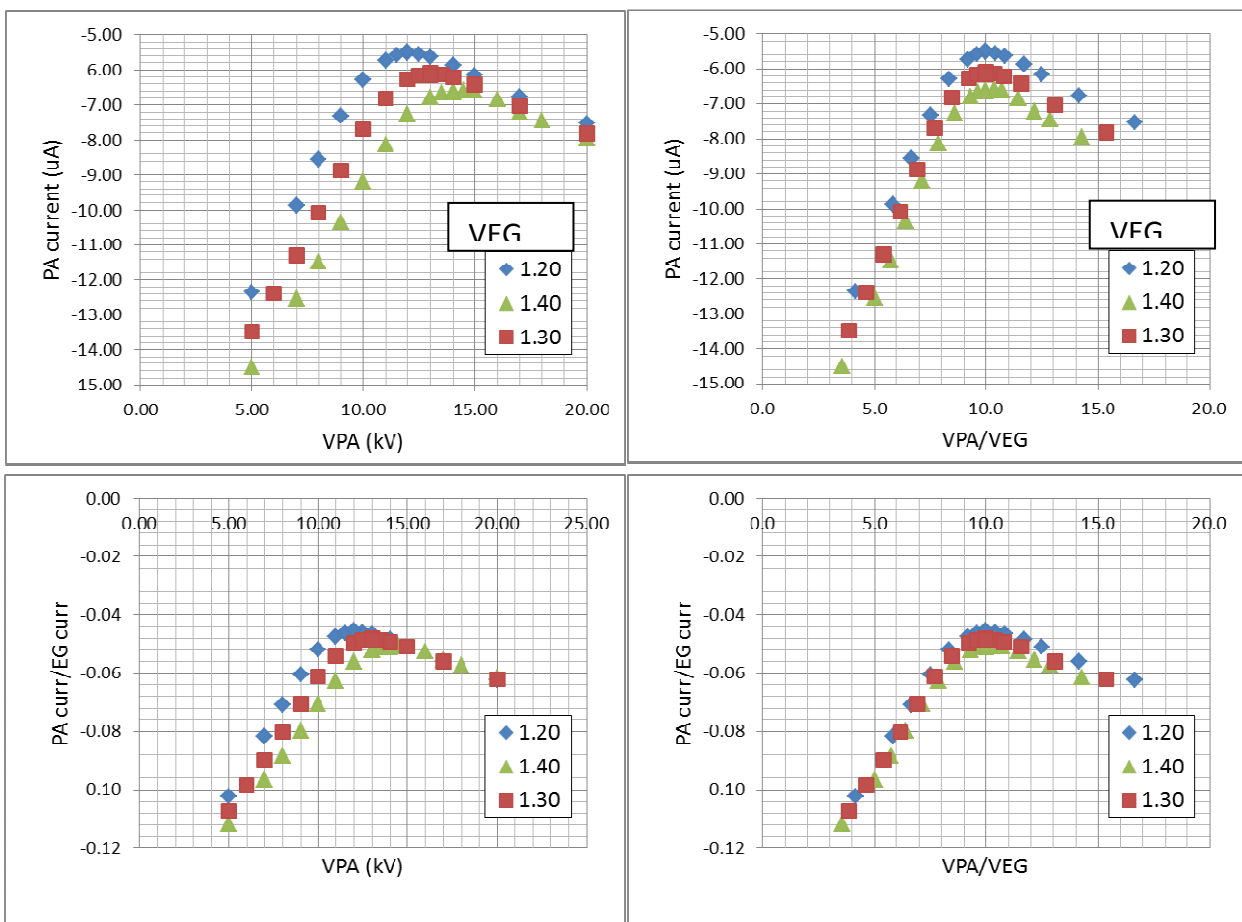

Figure 6.21 Variation of I_PA and I_EG as a function of VEGPS, VAGPS at RF power of 550W and 0.1Pa in the source for Air.

In this case a minimum was found for all cases (NB: PA current is negative because it is carried by negative charges) around a constant ratio of 10 between Acceleration Voltage and Extraction Voltage.

This behavior is probably due to the optimum for the beam optic since it is expected that at the minimum a higher amount of accelerated particles crosses the PA grid holes and thus is

122

not detected by the shunt; moreover an overall increase in the beam current can be observed with the extraction voltage.

In this case extracted current is very low also for the relatively low extraction voltage which was set juts up to 1.4kV in order to make it possible to evaluate the right branch of the curves since the acceleration voltage can be increased just up to 20kV in the present reduced operative conditions.

Another characterization of the beam intensity was obtained by keeping the ratio between the voltages constant at the optimum value referred to above (10) by a power scan at two different extraction voltages Figure 6.22. At first it can be observed that almost no ion current is extracted at 350W where, at this source pressure of 0.19Pa, plasma luminosity became very weak; then the beam intensity rises together with the light emission and thus with the radiofrequency power; also in this chart the effect of the extraction voltage on the beam intensity is shown, and by comparing the magnitude of the PA current in Figure 6.21 (at the minimum) with this values at the same power an increase due to the higher pressure in the source can be observed even for a lower extraction voltage (1kV).
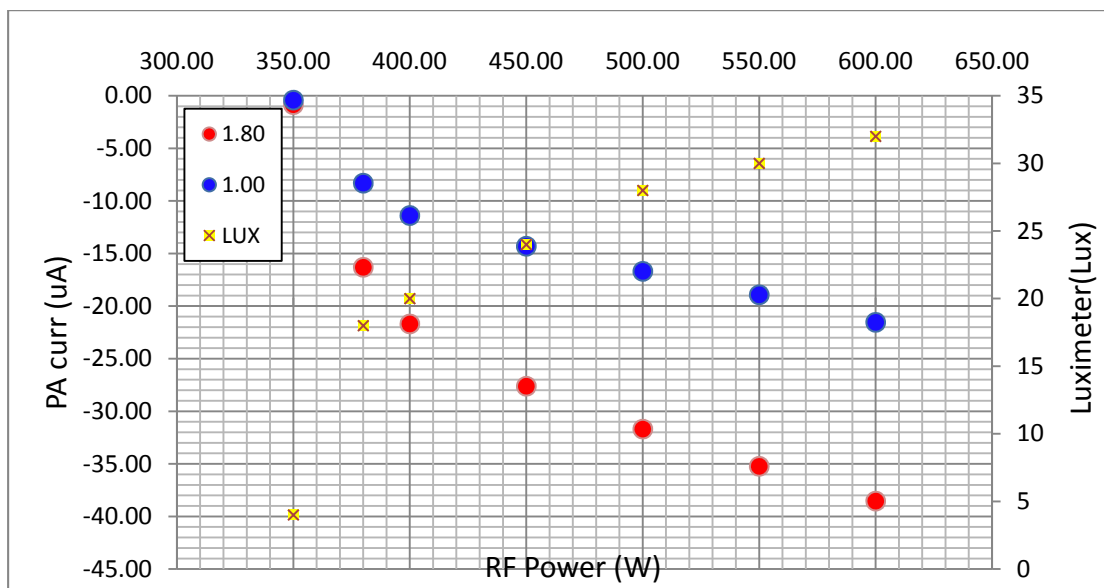

Figure 6.22 Power scan at 0.19Pa at different extraction voltages keeping constant the ratio VPA/VEG at 10 with VEG = 1kV and VEG = 1.8kV.

For all previous measures it would be appropriate to know also the current carried by the particles crossing the PA holes in order to measure the total beam current and to study roughly the optics since mini-STRIKE (MS) did not show any pattern of the beamlets profile but rather an overall increase of the tile temperature in the central zone [Figure 6.23], therefore just an integral measurement can be made.

Calorimetric estimation needs a heating/cooling transient long enough to fit the curve with precision by a thermal non linear equation:

- **Cooling phase**: In order to evaluate the current of the impinging beam from thermal equation, thermal conductance of the tile support R_{cond} and environment temperature T_{env} are needed, this is the temperature that would be reached at infinite time during the cooling phase since the temperature decay phase can be approximated as an exponential behavior with an asymptote corresponding at the environment temperature. In this case it was been assumed that the cooling phase occurs just by heat conduction through the tile support.

$$T(t) = T_{env} - (T_{env} - T_{ini2})e^{-\left(\frac{R_{cond}}{\rho V C_s}t\right)} = T_{env} + (T_{ini2} - T_{env})e^{-\frac{t}{A}}$$

where ρ = 1960kg/m^3 is the CFC density, V = 0.12×0.09×0.012m^3 is the tile volume, C_s=700J/(kg K) is the specific heat of the tile, and T_{ini2} is the temperature due to beam heating at the beginning of the cooling phase.
Then a non linear fit of the tile average temperature with the previous equation is made in order to get R_{cond} and T_{env}.

- **Heating phase:** for the heating phase, in the general case with no temperature saturation, both conduction through the tile support and thermal flux supplied by the beam q_{beam} have to be taken into account by the complete thermal equation:

$$T(t) = \left(\frac{q_{beam}S_{tile}}{R_{cond}} + T_{env}\right) - \left(\frac{q_{beam}S_{tile}}{R_{cond}} + T_{env} - T_{ini1}\right)e^{-\left(\frac{R_{cond}}{\rho V C_s}t\right)}$$

where S_{tile}= 0.12×0.09=0.0108 is the tile surface and T_{ini1} is the initial tile temperature (t=0) taken into account for the fit.
The first term on the righ-hand side represents the maximum temperature reached at stationary conditions (t=∞) so called T_{max} and it is evaluated from the fit.

- **Current evaluation:** from the power balance in stationary conditions

$$q_{beam}S_{tile} = V_{beam}I_{beam} = R_{cond}(T_{max} - T_{env}) \Rightarrow \boldsymbol{I_{beam} = \frac{R_{cond}(T_{max} - T_{env})}{V_{beam}}}$$

where V_{beam} is the acceleration voltage.

It's clear that this system is more precise for long acquisition times with respect to the thermal time constant A since the fit will be more accurate, furthermore material parameters have been assumed constants therefore for large temperature increases the error rises; an example of a typical thermal transients is shown in Figure 6.23 where the red line represents the fit curve on the thermal camera data used to obtain the current.

124

For this reason a fastest system to measure the total current impinging on the tile was installed, the Mini-STRIKE-shunt described in chapter 5m, by which the following charts have been made.

Then some measures performed by this system were compared with the calorimetric estimation in order to verify the accordance between the two systems.

It can be observed that the calorimetric estimation is quite in agreement with the electric one, since the two systems perform results with a maximum difference of a 30%, furthermore the thermal measurement is always greater, but it is based on the higher temperature on the tile, while the current is an average over the tile surface.
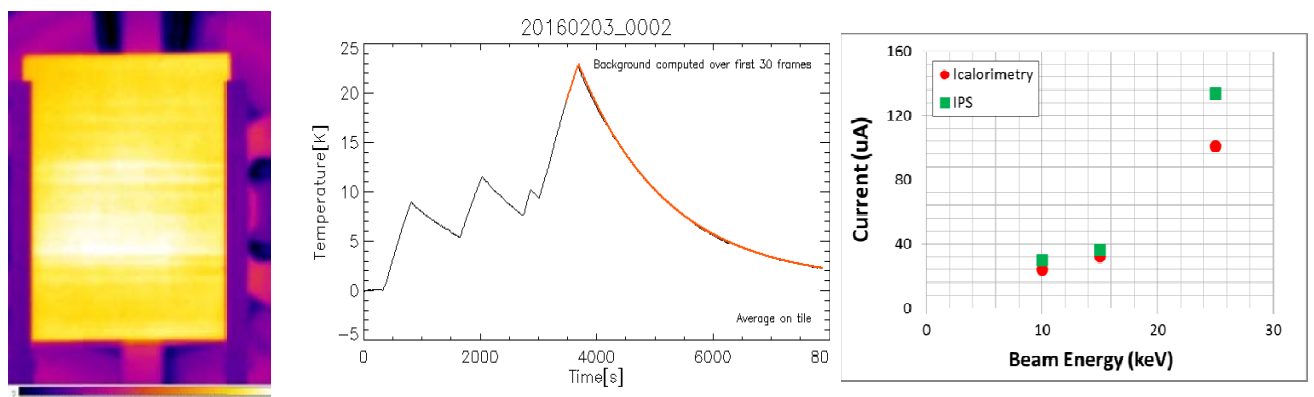

Figure 6.2311 Mini Strike (left), exponential fit of average tile temperature (center), comparison between thermal and electrical measurement (right).

Next charts (Figure 6.24) depict the current collected by the PA grid and also the fraction of the beam that is collected on mini-STRIKE by varying the Extraction Voltage with Acceleration voltage kept at 10kV; values have been normalized with respect to the electrons extracted from the source: in this way the optics can be better analyzed. For reduced values of extraction voltages a reduced amount of particles both on PA and MS is detected due to an overall reduction of the amount of extracted ions probably due to the fact that extraction voltage is not enough to extract ions from the plasma meniscus; then around the optimum (VEG=1kV) the best condition are found since the ratio of particles collected on the beam dump to those impinging on PA grid is maximum and at the same time the magnitude of the beam on the tile is maximum since the extracted current increases with the extraction voltage as shown in Figure 6.24 (lower). For EG voltages above 1kV a lot of ions hit the PA grid probably because focus point is too close to the plasma grid. Also the filters effect has been evaluated, and it results that by biasing the source (SB) at 10 volt with respect the Plasma Grid and increasing the filer current (PGF) from 10 up to 200A fewer electrons (filtered) and more ions were extracted from the source (less O$^-$ destruction due to high energy electrons in the extraction region) since there have been following improvements, calculated at the optimum point:

- EG current decrease by 9%
- PA current increase by 18%
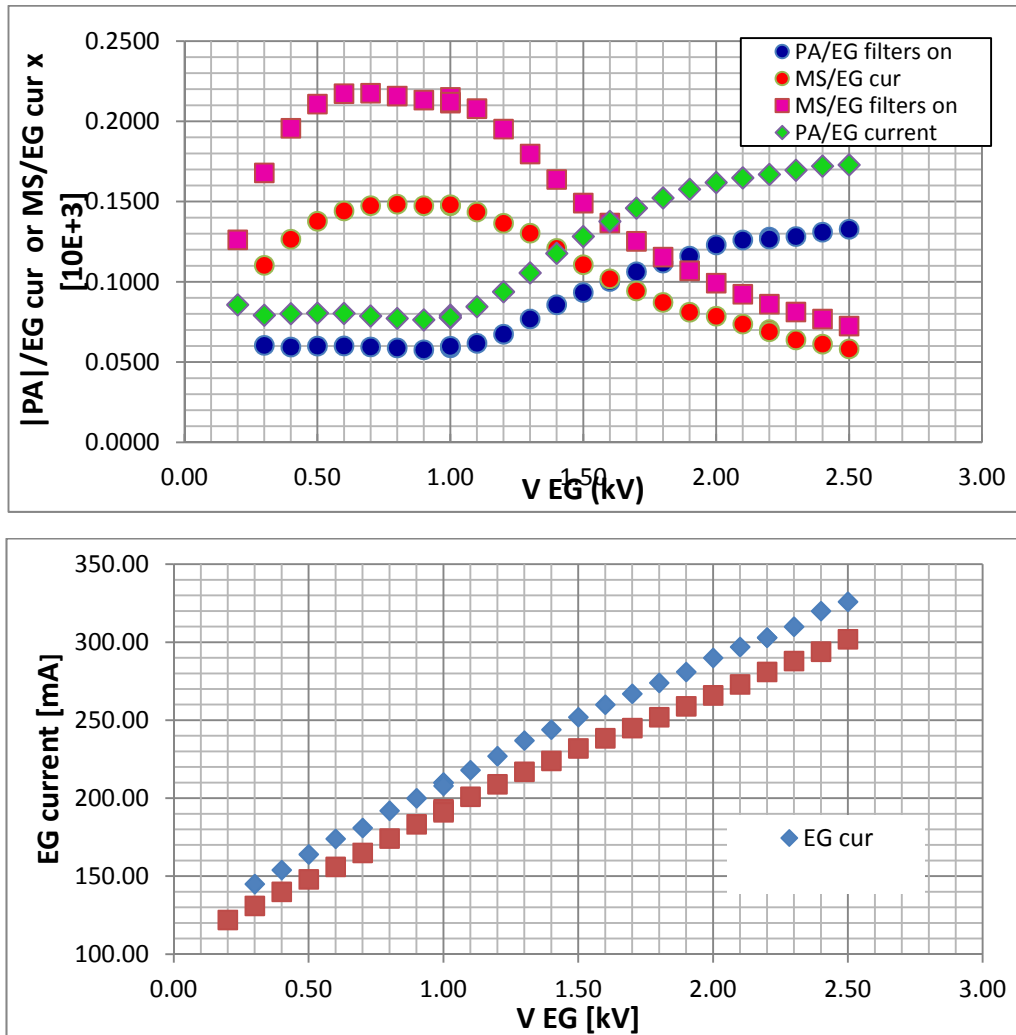- MS current increase by 32%

Figure 6.24 Beam currents on MS and PA normalized with respect to the Extraction Current for 0.17Pa at 600W (upper) with and without filters (PGF=200A and SB=10V) and with VAGPS=10kV; EG current vs VEG in the same conditions (lower).

As regards the influence of the pressure on the beam current, a scan was made and the total beam current was evaluated from the sum of both shunt currents; figure 16 was obtained at fixed ratio between voltages at the optimum point for 0.8kV of EG voltage and 600W RF power. Graph shows a strong dependence of the extracted beam on the pressure; nevertheless for pressure in the source higher than 0.6Pa breakdowns may arise as reported in the previous section; therefore at the moment this is a strong limitation with respect to the beam current improvement.

The scan in pressure shows also a strong dependence of the light emitted from the plasma in the source that increases with the pressure, and a reduction in the extracted electrons with the pressure increase; in Figure 6.25 the dependence of these parameters on the pressure is shown.
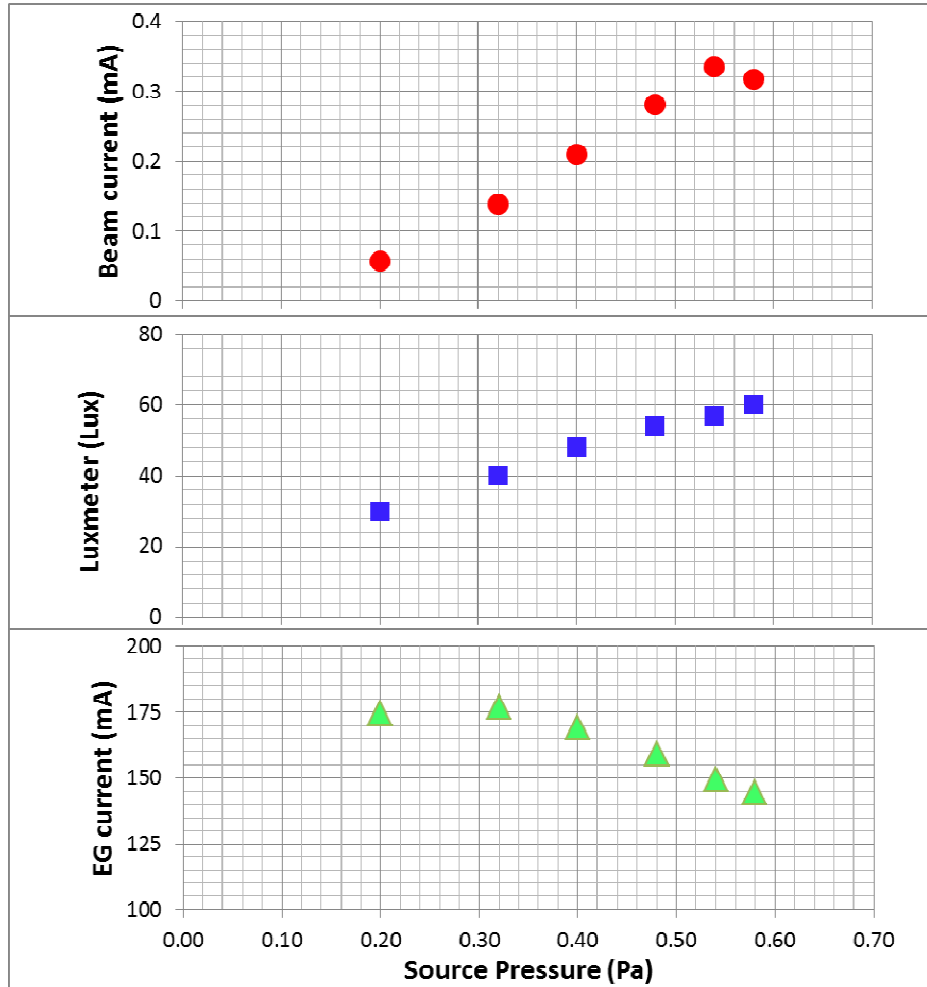

Figure 6.25 Pressure scan at 600W, VEG=0.8kV and VAG=8kV.

For previous reasons, with the purpose to further increase the beam current, since the benefits have been proved as shown in Figure 6.24, the Plasma Grid Filter was improved (Chapter.3) and the maximum value for the beam current of 0.6mA in air was achieved.
In Figure 6.26 the effect of the Plasma Grid filter is shown, at the extraction voltage of 1.2kV the improvement up to 400A has lead to an increase of a 20% for the whole beam compared to the case with 200A (old maximum PGF current); in Figure 6.26 also the RF power effect is shown for several extraction voltages by keeping constant the ratio VAG/VEG at 10.
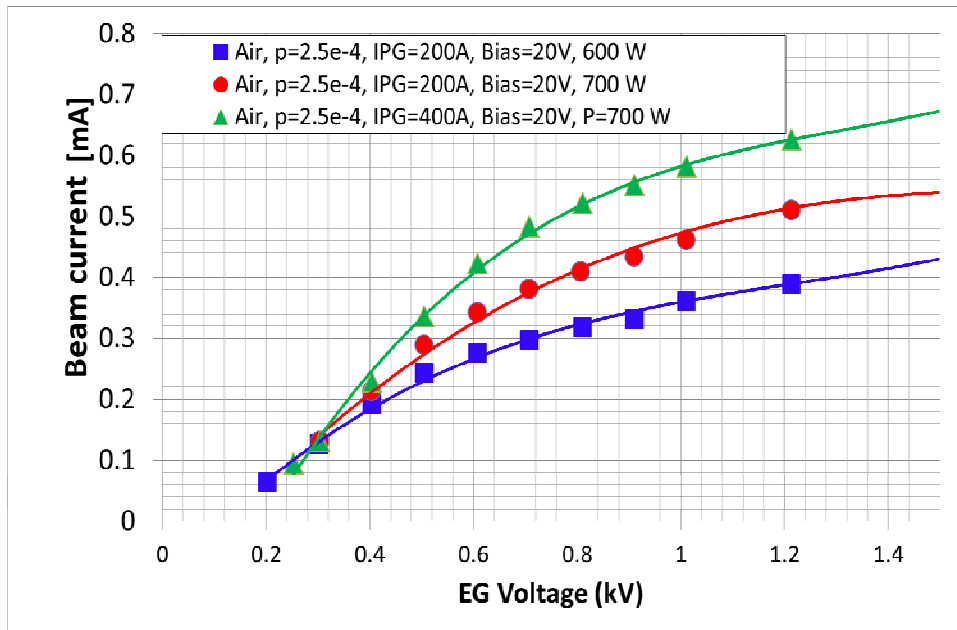
Figure 6.26 Voltage scan at the ratio VAG/VEG =10 for two RF powers and PGF at 0.51Pa in the source.

For the previous scan also the ratio between the current carried by the particles impinging on mini STRIKE and those on the PA grid was evaluated; Figure 6.27 shows that the best optics indeed does not depend just on the voltage ratio but also on the absolute value of the voltages at the optimum ratio; moreover the best condition depends also on the beam current since for higher values the minimum moves to higher values of voltages and this is probably due to the space charge effect that might be effective also in the second gap; this fact is positive because the target for future operations is a large increase both of voltages and currents, improving the optics.
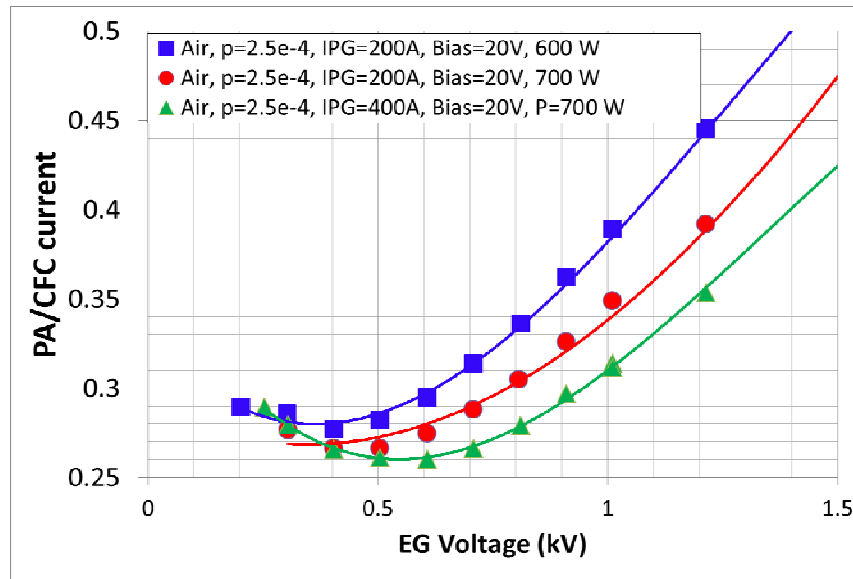
Figure 6.27 PA/MS current for different voltages at the ratio of 10 with 0.51Pa in the source for different values of RF and PGF.

With the aim to further increase the beam current it was chosen to operate with oxygen instead air since in air negative ions are made mainly by O^- and in pure oxygen the particle amount is 5 times greater at the same pressure, moreover the density of negative oxygen ions should further increase as long as the nitrogen density decreases; therefore an oxygen bottle was connected to the gas pipe.

From first operations it is come out a strong increase both in the CFC current and PA current with respect the air in same conditions, the ratio between maximum current for oxygen and air was 3 despite the concentration was 5 times higher.
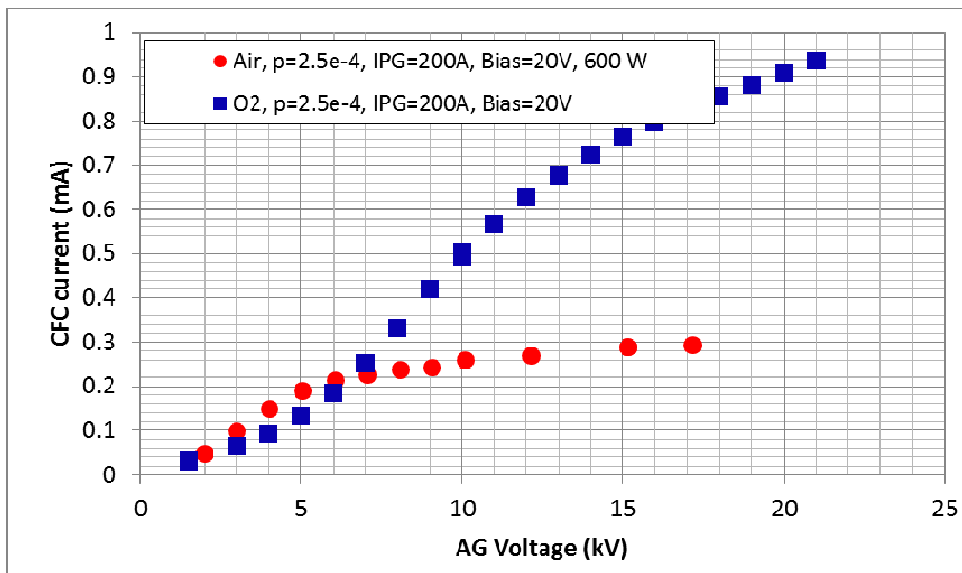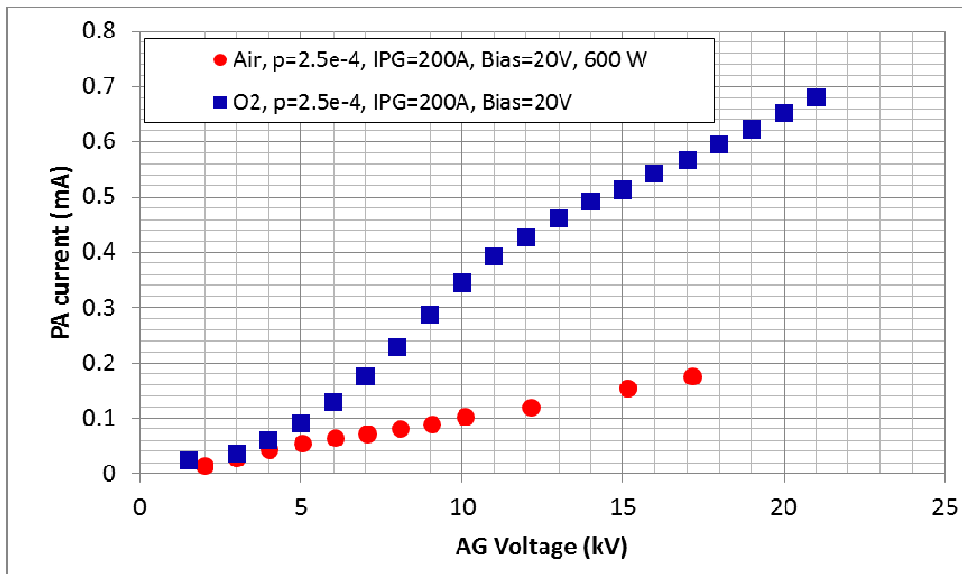
Figure 6.2812 Air vs Oxygen at 0.51 Pa in the source and constant ratio VAG/VEG of 10.

Also for oxygen the filter effect of the PGF has been analyzed as shown in Figure 6.29 and the following results have been achieved for 700W, 0.33Pa, 15kV and 1.8 kV respectively for VAG and VEG (maximum current collected on CFC):

- CFC current +22% (+15% from 200A to 400A)
- EG current -6% (-4% from 200A to 400A)
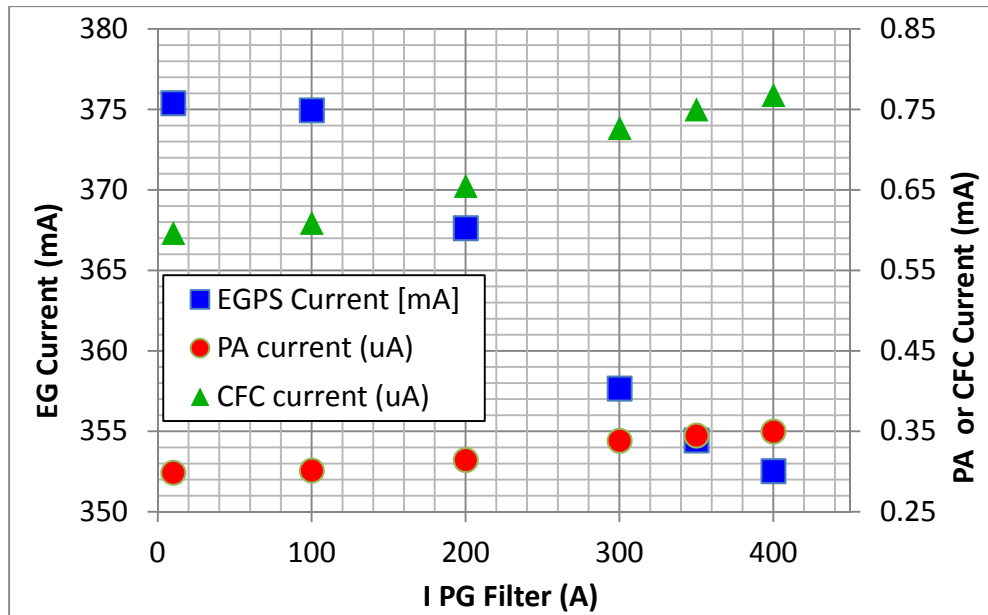- PA current +17% (+10% from 200A to 400A)

Figure 6.29 Plasma Grid Filter effect at 700W, 0.33Pa (source), VAG=15kV and VEG=1.8kV.

Previous results have confirmed the magnetic filter usefulness, especially the effect from 200A to the new limit of 400A; therefore a modification of the magnetic circuit is under development in order to increase the transversal magnetic field Bx in the source as shown in Figure 6.30.

Prototype will be made by an external coil (blue coil in figure21) which will be arranged outside of the source, the filter will be able to work with different layouts: red curve in Figure 6.30 shows the field along the transversal direction with 100A injected in the plasma grid and returning from the external coil (half for each conductor to preserve symmetry); in this way the integral of the field increases enhancing the confinement of high energy electrons without affecting excessively the driver region. Second layout (blue curve) would increase also the magnitude of the maximum field since current flows in PG(red arrow) then crosses a half of the external coil (blue arrow) and returns through the Bias Plate (green arrow), then flows again in the other half of the external coil and finally returns to the power supply (PGFPS); in this way the closed path integral involves a double current value increasing the B field; the effect is stronger also in the driver region and the consequences have to be verified.
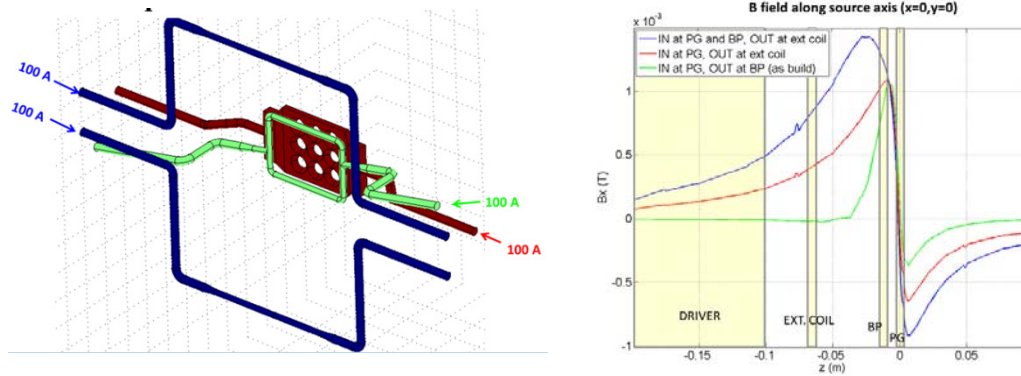
Figure 6.30 New magnetic filter prototype to reduce high energy electrons near the extraction region in the source.

Summarizing, during this first experimental operations with the beam acceleration, the extracted current was gradually increased, and the beam behavior was analyzed by new diagnostics installed and tested for the first time; moreover the electron/ions ratio is decreasing due to optics and filter improvement. The radiofrequency power is being increased and the Pyrex cylinder is under test; also sputtering inside the source was evaluated and until now the Molybdenum coverage seems to be effective since no metal particles were found in the source.

During these campaigns many data were collected and herein just the more meaningful in the context of the new diagnostics and improvement have been shown.

Currently caesium injection system is developed and a new Extraction Grid with weaker magnets is under test and soon it will be ready to be installed on NIO1; therefore air and oxygen campaigns are useful to prepare the experiment for instance diagnostics, data storage and analysis techniques as well as validation of numerical codes.

7 Conclusions

In the framework of nuclear fusion for energy production, Neutral Beam Injectors (NBI) represent a key component in the plasma heating as additional heating system in order to achieve the proper temperature for fusion reactions. In this project, Padova will play a major role in the design, research, development and construction of the NBI prototype for ITER. With the aim to gain experience in neutral beam injectors, also a smaller experiment, called NIO1, has been installed at Consorzio RFX as a project developed by the host and INFN-LNL (Laboratori Nazionali di Legnaro) on which my thesis work has been developed and the following results have been achieved. This thesis work has allowed to test the passive protections circuit previously designed and developed at Consorzio RFX: the system was found to work properly and it is satisfactory for power supply protection with the present reduced operating range; in particular the real need to protect the Extraction Grid Power Supply during EG-PA breakdowns was proved during normal operations with beam extraction. A lot of arcs with different behavior were collected and analyzed and the effect of the pressure and the radiofrequency power involved in plasma generation was found clearly linked to the breakdown voltage capability of the machine; therefore a simple model based on Paschen theory is not adequate but further numerical analysis taking into account charge generation and probabilistic particle paths during breakdowns are needed in order to understand how to reduce the probability of electrical discharges. Another new assembly tested is the Fast Protection Unit (FPU) that coordinates the switch-off of the high voltage (HV) power supplies; two current sensors, the Rogowski coils, were built characterized, tuned and installed on NIO1, and then tested both during dedicated campaigns and normal operations. In many cases Rogowski coils are capable of sensing the over-currents by detecting the arcs and therefore FPU works by switching off the HV power supplies, nevertheless the measurement of the Rogowski coils output during breakdowns is not yet satisfactory since a lot of noise is present due to the fact that the oscilloscope reference is the HVD potential. On the other hand, sometimes the FPU issued a signal with no real arcs measured by current probes; sometimes arcs were not detected, especially in the air campaign where EGPS arcs occurred; therefore a more accurate tuning has to be done both on the comparator threshold and on the Rogowski load for example by increasing the sensitivity of the EGPS Rogowski coil; moreover a differential probe might be used to acquire the Rogowski signals. As regards the mechanical improvements, the new Pyrex cylinder seems to work properly even if up now the RF power has been limited up to 900W; from preliminary inspections it seems that the molybdenum covers installed in the source have been effective to reduce the sputtering effect. Also a thermocouple board for acquisition and conditioning of the signals was developed and the most suitable components were chosen after dedicated tests; then a prototype with a reduced number of channels was realized and tested directly on NIO1. The board can work with grounded-junction thermocouples, by avoiding ground loops, and it is an important achievement since for SPIDER grounded-junction thermocouples have been chosen. The experimentation on NIO1 has been very useful since the environment

is characterized by a strong RF noise, and it was evident that the signal is affected by this noise; in particular an offset in the measurement appears when the plasma is inductively coupled and it was proved that this is due to the environmental field picked-up by thermocouples wires. More investigations both on thermocouples shielding and the board bandwidth have to be done in order to reduce and filter the noise. Also a preliminary design of an insulation module for the thermocouples board has been made for SPIDER Grounded Grid application where the overvoltage constraints are very strict: a preliminary design of a small insulating transformer has been made and main problems due to working in vacuum have been highlighted, more work has to be done to define all the characteristics by numerical simulations. During this thesis an important milestone was achieved: for the first time a beam of particles was extracted from NIO1 and it was also confirmed by independent measurement techniques based on electrical currents and temperature increases. Two new measurement systems have been developed, installed and tested in order to evaluate the beam current and to study the beam optics for the first time; these systems proved to be very useful especially for small currents. Also the effect of the plasma grid filter, which was improved by allowing to double the filter current, and of the plasma grid bias were investigated thanks to these measurement systems. Furthermore Mini-STRIKE was used for the first time on NIO1 and thermal measurement proved in great accordance with the electrical system. Also a lot of work was done in order to improve the control interface and in particular the data storage in order to provide a smart system for data analysis; also the new current sensors have been integrated in the control interface by a Raspberry which communicates with the main PC. During the thesis period NIO1 experiment capability grew a lot: the beam current increased from a few micro amps to over 1mA; currently the filling gas is Oxygen, but for the future many improvement are expected in order to increase the current also in Hydrogen: there is a lot of room for improvements since caesium will be injected in the source, a new EG will be installed, the RF power gradually will be increased, and a new passive protection system is under development to fulfill the requirements of NIO1 in terms of extraction and acceleration voltages; for this a better understanding of the breakdown phenomena, including the data collected during the present thesis, will be necessary.

Bibliography

Chapter 1

[1] Mitsuru Kikuchi, Karl Lackner, Minh Quang Tran**, *" Fusion Physics"*, International Atomic Energy Agency,2012

[2] https://en.wikipedia.org/wiki/Helium

[3] http://iec.neep.wisc.edu/operation.php

[4] http://www.iter.org/

[5] M. A. Lieberman and A. J. Lichtenberg*: "Principles of Plasma Discharges and Materials Processing"*. New York: John Wiley & Sons, 1994: p. 137.

[6]R.S. Hemsworth and Takashi Inoue. *"Positive and negative ion sources for magnetic fusion"*, *IEEE Transactions on Plasma Science* 33 (2005),pp. 1799–1813.

[7] https://www.iter.org/mach/heating

[8] https://www.iter.org/newsline/21/952

[9] G. Brown (Ed.): *"The Physics and Technology of Ion Sources"*. Weinheim: Wiley VCH Verlag GmbH & Co. KGaA, 2004: pp. 159‑187.

[10] https://en.wikipedia.org/wiki/Work_function

[11] P. Franzen *et al.*, *"Progress of the development of the IPP RF negative ion source forthe ITER neutral beam system"*, Nucl. Fusion **47**, 264 (2007)

[12] V. Toigo et al. "*Progress in the realization of the PRIMA neutral beam test facility*", *Nuclear Fusion* **55** (2015) 083025.

Chapter 2

[1] R. S. Delogu , C. Poggi, A. Pimazzoni, G. Rossi and G. Serianni, "*Analysis of diagnostic calorimeter data by the transfer function technique*", Rev. Sci. Instrum. **87**, 02B932 (2016)[2] Andrea Rizzolo, Mauro Dalla Palma, Michela De Muri, , Gianluigi Serianni," *Design and analyses of a one-dimensional CFC calorimeter for SPIDER beam characterisation*", Fusion Engineering and Design, 2010,pp 2268-2273

[3] M. Cavenago, G. Serianni, et al., Rev. Sci. Instrum. 85, 02A704 (2014).

[4] M. Cavenago,"*INFN for NBI: RFX and NIO1*", Legnaro, 17 Feb 2015

[5] B. Zaniol, M. Barbisan, M. Cavenago, M. De Muri, A. Mimo, R. Pasqualotto, and G. Serianni, "*NIO1 diagnostics*", AIP Conference Proceedings 1655, 060010 (2015)

[6] Cavenago, Serianni et al.,"*First Experiments with the Negative Ion Source NIO1*" Rev. Sci. Instrum. **87** (2016) 02B320

[7] M. Barbisan, B. Zaniol, M. Cavenago, and R. Pasqualotto, "*Modeling and design of a beam emission spectroscopy diagnostic for the negative ion source NIO1*", Review of Scientific Instruments 85, 02A708 (2014)

Chapter 3

[1] Peter C Stangeby, The Plasma Boundary of Magnetic Fusion Devices, IOP Publishing Ltd, London, 2000

[2] M. Barbisan C. Baltador, B. Zaniol, M. Cavenago, U. Fantz, R. Pasqualotto, G. Serianni, L.Vialetto and D. Wünderlich, "*First hydrogen operation of NIO1: characterization of the source plasma by means of an optical emission spectroscopy diagnostic*", Rev. Sci. Instrum. **87** (2016) 02B319.

 [3] M. Pavei, S. D. Bello ; H. Groeneveld ; D. Marcuzzi ; A. Rizzolo, " *Molybdenum armour layer on copper plates: Manufacturing technologies and tests of prototypes*", Fusion Engineering (SOFE), IEEE 25th Symposium on *(2013)*

[4] http://electrons.wikidot.com/semiconducting-ceramics:varistor-applications

[5] M. Recchia, B.Laterza, T.Patton, *" NIO1 HV protection system*", Technical note RFX_NIO_TN_019, 2016

[6] Peter Tant, Student Member, Bruno Bolsens, Tom Sels, Daniel Van Dommelen, Johan Driesen, and Ronnie Belmans, Fellow, "*Design and Application of a Field Mill as a High-Voltage DC Meter*", IEEE TRANSACTIONS ON INSTRUMENTATION AND MEASUREMENT, VOL. 56, NO. 4, AUGUST 2007

[7] C. Bonacina, A. Cavallini, L. Mattarolo. Trasmissione del Calore. Ed. CLEUP, Padova, 1992

[8] http://www.engineeringtoolbox.com/thermal-conductivity-d_429.html

[9] http://www.vidrasa.com/eng/products/duran/duran_pf.html

Chapter 4

[1] http://www.ing.unitn.it/~colombo/Termocoppie/3)Funzionamento.htm

[2] M. Brombin, R. Ghiraldelli, F. Molon, G. Serianni, R. Pasqualotto *"Design and test of readout electronics for thermocouples on ion beam sources*"

[3] https://www.adafruit.com/datasheets/MAX31855.pdf

[4] http://www.ti.com/lit/ml/slup124/slup124.pdf

[5] D. Ilic, D. Mosti , E. Dolicanin, K. Stankovi c, P. Osmokrovic *" Mechanisms of Electrical Berakdown in Low Vacuums"* scientific publications of the state university of novi pazar ser. a: appl. math. inform. and mech. vol. 3, 2 (2011), 85-99.

[6] http://it.omega.com/temperature/Z/pdf/z041-044.pdf

[7] http://www.omemspa.com/download/comparazioni.pdf

[8] http://www.lpiemme.it/Filismaltati.htm

Chapter 5

[1] G. Serianni E. Sartori P. Agostinetti M. Brombin P. Veltri, "*Notes on the joint test campaign at NIFS June-July 2015*" Technical note: RFX-SPIDER-TN-385, 2015

Chapter 6

[1] L.F.Berzak, S.E Dorfman, and S.P Smith,"*Paschen Law in Air and Noble Gases*", April 25, 2006

[2] http://www.elettrotecnica.unina.it/files/lupo/upload/Mazzanti%20Cap1-1.pdf

[3]https://it.wikipedia.org/wiki/Plasma_(fisica)

[4] P. Veltri1, M. Cavenago2, G. Serianni1 et al., "*Design, modelling and operation of the NIO1 negative ion source*", AIV Conference, Genova, 20-23 May 2015

[5] https://en.wikipedia.org/wiki/Electron_affinity_(data_page)